# Experimental Investigation of Time-Reversal Techniques using Electromagnetic Waves

A dissertation in partial fulfillment of the requirements for the degree of

Doctor of Philosophy in Electrical and Computer Engineering


Submitted by

Ahmet Gurkan Cepni


To the Faculty of the Department of Electrical and Computer Engineering

in the Carnegie Institute of Technology


Carnegie Mellon University

Pittsburgh, Pennsylvania


December 2005

# Abstract

Time-reversal is a novel method to utilize the multipath components in a cluttered environment for super-resolution focusing. The conventional thought about the adverse effects of multipaths on communication systems has been changing based on recent findings showing how to use multipath components to create independent paths between transmitter and receiver. Time-reversal schemes are one of these recent techniques which can convert the traditionally hostile multipaths into performance-boosting elements in a two-way communication system as well as target detection, and localization systems in a cluttered channel. Time-reversal techniques utilize the scattering of waves in the medium to improve the resolution of focusing in multipath rich channels. The successful demonstrations of time-reversal experiments using low frequency waveforms in acoustics and ultrasonics have generated interest in time-reversal methods using radio-frequency electromagnetic waves. The wide-range of possible applications have ignited extensive research on this area. The work studied in this thesis is based on experimental investigation of time-reversal methods using electromagnetic waves. The ultimate aim is to demonstrate by experiments the gains achieved by electromagnetic time-reversal techniques over conventional radar methods to focus radar beams, to null the clutter environment and finally to detect targets in highly scattering environments. To that end, the main principles of time-reversal systems have been studied and the clutter channel has been analyzed to assess the feasibility of time-reversal methods in a laboratory environment. We have demonstrated physical time-reversal focusing in the frequency domain as well as in the time-domain. Frequency domain instruments allowed us to do wideband (>1 GHz) time-reversal experiments while in the time-domain the available bandwidth was limited to 40 MHz. In the frequency domain, with the help of wideband phase shifters and network analyzer,

**Abstract**

physical time-reversal focusing and nulling experiments have been done in a laboratory environment. The time-domain experiments have been conducted at 2.45 GHz in a cylindrical cavity environment. The degree of focusing and nulling depends on the multipath components in the channel as well as the bandwidth of the signal. The cavity provides a multipath-rich environment where we can show focusing and nulling by using a relatively small bandwidth compared to free space. By using 36 MHz of bandwidth, we have demonstrated single antenna time-reversal focusing and nulling. The wireless channel is reciprocal. This allows us to also do back-propagation using a computer instead of physically re-emitting the waves from the antennas. In a complex lab environment, we have demonstrated computational time-reversal focusing and nulling using 6 antennas and a two dimensional grid that has 100 points on it. The results have shown that the time-reversal system performance depends on three parameters. These are bandwidth, multipath components in the medium, and the number of antennas on the time-reversal array. We have characterized a scattering environment where we have dielectric rods and copper pipes as scattering objects. The experiments have been conducted starting with a simple scenario (e.g. one single rod in the range of the antenna array) and extended to increasingly complex propagation environments, with a progressively larger number of scatterers placed in the channel. The important parameters have been extracted and using simulations we have extended the results to larger scattering environments than permitted in the laboratory. We have worked on the detection performance of a time-reversal system and compared it with conventional detection methods. The matched filter deteriorates as we increase the complexity of the medium. On the contrary, time-reversal has better performance as the scattering environment gets more complicated. We have described experimental results using a multiple antenna detection scheme that is based on clutter nulling. By using time-reversal, the response from the cluttered medium is first nulled. When the target enters into the medium, the electromagnetic energy focuses around the target so that a stronger echo is obtained. The experimental results show that using time-reversal techniques, we can improve the signal-to-noise ratio of the return-echo due to the target compared to conventional change-detection radar.

# Acknowledgements

Firstly, I would like to thank my advisor, Professor Daniel D. Stancil for his guidance over the last five years. I feel myself fortunate to have very stimulating talks with him that resulted in inspirations and new ideas. His human behavior will always be an example for me.

I owe a tremendous debt of gratitude to the time-reversal research group members. I learned a lot from our faculty advisors Professor Jose M.F. Moura, and Professor Jimmy Zhu. I will never forget the highly exciting research discussions during our group meetings. I also want to thank my fellow colleagues in the time-reversal research group Ben Henty, Dr. Yuanwei Jin, Yi Jiang, Lin Cheng. I had very nice collaborations with them.

I also want to thank my PhD committee member Dr. Nitesh Shah, from Raytheon Company in Tuscon, Arizona. I had very valuable feedback from him and advice on the project. I greatly appreciate his comments on this thesis.

This work is partially funded by DARPA through the Mathematical Time-Reversal program. I would like to thank our program manager Dr. Carey Schwartz. His fruitful discussions and comments on the time-reversal project have always given us new horizons.

I have also had the pleasure of interacting with very respectful colleagues including but not limited to J.P. Van't Hoff, Jessica Hess, Kevin Borries, Jake Meyers, Ariton Xhafa, Pavel Nikitin, and Ratish Punnoose.

Finally, I would like to thank my parents, without whom none of this would be possible. They always have been an inspiration source for me.

# Table of Contents

# List of Figures

# List of Tables

# Chapter 1

# Introduction

## 1.1 Background and motivation

Inhomogeneity is a characteristic property of every real medium. These inhomogeneities may be regular and/or random. While wave propagation in a duct or waveguide is an example of a regular inhomogeneity, random inhomogeneities may include scattering of waves. The scattered waves are superimposed on the incident wave and can lead to amplitude and phase fluctuations in the received field. This effect can be observed in the fluctuations of intensity of sound waves in the atmosphere and fading effects of radio signals in a wireless channel.

In the case of the wireless channel, the principles of electromagnetic wave propagation through the medium can be described with three mechanisms: these are reflection, diffraction and scattering. Electromagnetic waves arriving from a certain direction at a surface with large dimensions compared to the wavelength are (partially) reflected by this surface. The intensity of the reflected wave depends on the radio wave frequency, the type of material, the polarization of the wave and the angle of incidence. Diffraction can be explained as an apparent bending of radio waves around obstacles. Scattering is the dispersion of radio waves due to contact with objects with irregular structures or surfaces [1].

Because of all these effects, the electromagnetic wave that reaches the receiver may look

very distorted. Multiple paths can be observed in the received signal. In the case of digital communication, these multipath effects can cause intersymbol interference and may result in errors while making decisions as to whether the signal is a zero or one. Traditionally multipath was thought to degrade the performance of a communication system, but recent results using multiple input and multiple output (MIMO) antenna systems have shown that multipath provides an extra degree of freedom which can be utilized to improve the capacity of a two-way communication system [2], [3], [4], [5], [6], [7], [96]. In a rich-multipath environment, the receiver can separate the multiple propagating paths. In other words, the channel can be decomposed into a set of subchannels that relay independent information from transmitter to receiver.

The performance of a radar system also suffers from a multipath environment. As the medium becomes more cluttered, the detection performance of conventional radar systems seriously degrades. The angular resolution of a conventional radar antenna is limited by the antenna mainlobe beamwidth. To reduce the antenna mainlobe beamwidth by conventional approaches requires either using a larger antenna or operating at a higher frequency [8]. Both approaches may be undesirable for radar systems. Alternatively, we can use space-time processing to enhance the angular resolution of the antenna and achieve better imaging.

A novel method to utilize the multipath components for super-resolution focusing is the time-reversal technique. Time-reversal focusing can be used to improve the detection performance of a radar system in a highly cluttered environment as well as to enhance the signal-to-noise ratio of a two way communication scheme. As the name suggests, the basic idea of the time-reversal method is like playing a movie backwards.

In the time-reversal process, the channel is first illuminated with a uniform pulse. The returned echo is recorded by an array of probes, time-reversed and then re-transmitted into the medium [9]. Time-reversed signals propagate backwards through the time-independent medium and go through similar multiple scattering, reflections and refraction that they underwent in the forward direction, resulting in energy being focused around the initial

source.

In this thesis, we experimentally investigate time-reversal techniques using electromagnetic waves. The main purpose of this thesis is to demonstrate the gains achieved by electromagnetic time-reversal techniques over conventional radar methods to focus radar beams, and detect the targets in highly cluttered environments. The first step to a time-reversal based detection scheme is to characterize the clutter channel. We examine the time-reversal focusing and nulling performance, the spot size, the effect of bandwidth, number of antennas, antenna array size, and the degree of scattering needed in the field. The experiments have been conducted in a controlled scattering medium, in a complex laboratory environment, and in a multipath rich cavity channel. Physical and computational time-reversal systems have been implemented to assess the feasibility of time-reversal methods in different channels and to evaluate the trade-offs involved. Time-reversal systems have been demonstrated in the frequency domain and time-domain. The experimental considerations are described. We compare the conventional matched filter approach to the time-reversal approach. Based on the analytical framework and simulation results, we have built experimental systems in the lab to carry out experiments using conventional radar techniques (using the matched filter and change detection schemes) and the time-reversal approach. We started with a simple case using a single rod and gradually increased the complexity of the scattering environment. In the case of a single target in the field, conventional radars using a matched filter work very well. As the number of scatterers increases, the performance of matched filter detection deteriorates. There are other methods to improve the detection probability when there are many scattering objects in the medium. One of those techniques is known as matched field processing. The matched field processing requires knowledge of the channel Green's function $G(t)$ for every target position in the field. These data should be provided either by simulation or experiments in the field. Due to the complexity involved in the process, this is not workable in most practical applications. In time-reversal, we can detect the target without the need of the exact channel response. By time-reversal, the radar filter is automatically matched to

the channel and the scatterers inside the channel. With appropriate algorithms, the RF energy can be focused around the target object in a highly scattered channel thus improving the target detection performance.

## 1.2 An overview of time-reversal techniques studied in the literature

In a homogenous medium, the focusing resolution is diffraction limited (Rayleigh resolution) because of the finite aperture length of the antenna array ([10]). In randomly heterogeneous media, the focusing resolution is much tighter, since the presence of scattering centers in the medium improves the effective aperture of the antenna array ([9], [11], [12]).

By using time-reversal techniques in a rich multipath environment, we can achieve a resolution which is better than the Rayleigh resolution. Anything better than the Rayleigh resolution is called super-resolution. Super-resolution in the time-reversal process is achieved by doing inverse-scattering. The back-propagation of the signal through the inhomogeneous medium increases the effective aperture of the antenna array and results in sharp focusing around the source. Wave propagation in a random medium has been studied extensively in physics [13], [14], especially in optics. These studies have included wave diffusion and optical localization in random composites. In the frequency domain, time-reversal is equivalent to phase conjugation which has been studied extensively in optics since 1970's. The phase-conjugation applies to monochromatic waves and this technique is used to cancel the distortions of the medium [15]. Later, Fink and co-workers designed a successful time-domain experiment in which they showed time-reversal focusing using a relatively broadband (1 and 3 MHz) ultrasonic signal. They also showed that if there are several reflectors in the medium, the time-reversal technique can be iterated so that the back-propagation signal focuses on the most reflective one [16]. Physical time reversal has been explored by using ultrasonic waves ([17], [18], [19], [20], [21], [22]), and acoustics ([23], [24], [25], [26], [27], [28], [29], [30]). The underlying principles of time-reversal have

been researched through numerical simulations ([31], [32], [33], [34], [35]) and theoretical analysis ([36], [37], [38], [39]). Time-reversal has many applications in various fields like medicine (e.g. in the destruction of kidney stones, ultrasonic focusing in human tissues), geophysics (e.g. finding the center of an earthquake), non-destructive testing, underwater acoustics, wireless communications, radar systems (like retrodirective antenna arrays). It is also possible to image the medium through computational time-reversal ([35], [40], [41], [42], [43], [44], [45], [46]). Time-reversal methods have been used to perform selective focusing on passive targets. The system relies on decomposition of the time-reversal operator and is called DORT (The Time-Reversal Operator Decomposition) method ([53], [54], [55], [56],[48], [49], [50], [51], [52]). The locations of targets can be identified from the time-reversal method through the singular vectors associated with non-zero singular values using the background Green's function. The target scattering strengths can be determined by the set of singular values using the DORT method. The DORT method requires that the number of targets should be less than or equal to the number of antenna elements in a time-reversal array and the targets should be well resolved. Another method that is used to image a medium to locate targets is called time-reversal MUSIC (MUltiple SIgnal Classification) and developed by Devaney ([57], [58], [59]). Time-reversal MUSIC does not require that the targets should be well-resolved, but similar to DORT it requires that the number of transceiver antennas (N) should be greater than the number of targets (M) in the field to be scanned ($M < N$). Devaney has shown that the time-reversal multiple signal classification algorithm obtained using the background Green's function gives accurate estimates of the positions of the targets even in the presence of multiple scattering between the scattering objects and the target in the medium. The target scattering strengths are also computed using a non-linear iterative algorithm [60]. The DORT algorithm utilizes the non-zero singular vectors and values of the multistatic matrix, while MUSIC makes use of the zero-singular vectors and values [58].

Currently, there is a growing research effort to apply time-reversal techniques using electromagnetic waves. As the RF instruments become more available, the time-reversal

methods find applications in two way communication systems, as well as radar detection and imaging applications. As one of the earliest implementations of time-reversal methods at RF frequencies, in [61], [62], Henty and Stancil showed time-reversal focusing using the phase-conjugation technique in the frequency domain. Their experiments have shown that by using a single-frequency phase-conjugation approach, energy could be focused around two targets which were separated by one-half wavelength. In [63], Fink and his research team presented a time-reversal focusing experiment at microwave frequencies. They showed experimentally that by using electromagnetic waves, they can focus a 1 MHz wide pulse in a cavity environment.

A time-reversal based target detection scheme has been proposed by Zhu and Jiang using electromagnetic waves [65]. The 2-D FDTD-based simulation results have shown that the clutter channel can be cancelled first through time-reversal nulling methods using multiple antennas. When the target enters into the medium, the time-reversal energy focuses around the target resulting in higher power return from the target [65]. The method is called time-reversal adaptive interference cancellation (TRAIC) and is studied through analysis [66], [67] and experimentation [68]. Time-reversal schemes have been implemented and compared with change detection schemes. Using single antenna time-reversal methods, in [69] Moura and Jin have presented various detection algorithms. In [71], Gingras and his collaborators have provided a theoretical analysis of time-reversal techniques using electromagnetic waves. Using 2-D FDTD simulations, Yavuz and Teixeira showed electromagnetic time-reversal focusing in random media, and also looked into the impact of polarization on time-reversal focusing [72]. In [73], the background Green's function has been estimated and the imaging of an experimental medium has been obtained using electromagnetic time-reversal techniques. In [74], by using simulations, Sarabandi, et. al. showed time-reversal focusing in a forest environment.

Time-reversal methods can also be used in two-way communications systems (e.g. cellular or wireless LAN systems). The idea is to use a time-reversal filter for each user and convolve the incoming data streams with the appropriate filter so that the signals focus

around the user's physical location. By using time-reversal filter during the data transmission from the base station, the channel dispersion can be removed and an ISI-free communication link can be obtained which can potentially enhance the capacity of the channel. It can also be used in space division multiple access algorithms to spatially differentiate the users [62], [75], [76], [77].

## 1.3 Outline of thesis

In this thesis, we explore the time-reversal methods using electromagnetic waves. The main emphasis is on target detection in highly cluttered media. Firstly, the cluttered channel is analyzed, the main parameters are extracted, and the feasibility of time-reversal methods and possible advantages are discussed. In Chapter 2, the clutter channel is examined through theory, simulations and experiments. We have performed physical time-reversal experiments in time-domain as well as in the frequency domain. In the time-domain the bandwidth of the pulse is limited to 40 MHz due to equipment limitations. In the frequency domain, we have used stepped frequency measurements using a vector network analyzed and wide-band I-Q modulators. The details of the frequency domain experiments are discussed in Chapter 3. Additionally, multiple antenna time-reversal experiments in a laboratory environment are described and the results discussed. In Chapter 4, time-domain experiments are described. Single antenna time-reversal focusing and nulling experiments have been conducted in a multipath rich cavity environment. In Chapter 5, we describe time-reversal based detection schemes and compare them with conventional change detection and matched filter schemes. Single antenna as well as multiple antenna detection systems are explained. Chapter 6 concludes the thesis along with a contribution summary and suggestions for future work.

# Chapter 2

# Channel Characterization of Clutter

## 2.1 Introduction

Time-reversal methods have been proposed for many different applications ranging from ultrasonic focusing on human tissues to detection and localization of targets in highly cluttered mediums using electromagnetic waves. The use of time-reversal methods for enhancing the detection performance of a radar system has spurred significant interest in space-time-frequency processing. A key consideration in time-reversal based detector design is modelling the complex propagation environment. The radar operating channel can be modelled by using various techniques like ray tracing [78] and direct solution of Maxwell's equations for the electromagnetic field in the given region [79]. Another approach is to statistically analyze the propagation environment. Statistical ensembles of field strengths can be calculated for different regions and we can estimate the parameters of the statistical distributions [80]. The main objective of this chapter is to understand the propagation medium and analyze the main parameters that can affect the time-reversal performance. The time-reversal system is analyzed through theory, simulations and experiments. The channel characteristics should be studied so that the system designer knows the trade-offs before implementing a time-reversal system. The density of scattering objects in the field has a big impact on time-reversal performance. That should be

analyzed and the main parameters should be investigated. The bandwidth and operating frequency of the waveform directly affect the time-reversal performance as well as the radio design. The time-reversal performance improves with many antennas on the array. The number of antennas that should be used and, the antenna spacing on a given array length are important questions that should be understood. In this chapter, we will address some of the important questions regarding the channel propagation characteristics before starting to design time-reversal based systems. We will start with a brief overview of the time-reversal method. Then the simulations will be explained and the results will be analyzed. After that, experiments will be described and the discussions will be presented. In a time-reversal process, the channel is first illuminated with a uniform pulse (Fig. 2.1a), the returned echo is recorded by an array of probes (Fig. 2.1b), time-reversed and then re-transmitted into the medium (Fig. 2.1c). Time-reversed signals propagate backwards through the time-independent medium and go through similar multiple scattering, reflections and refraction that they underwent in the forward direction, resulting in energy being focused around the initial source (Fig. 2.1d). The focusing happens both in space and in time. We can regard the time-reversal process as a space and time correlator. The more multipath components the channel provides, the more constructive interference happens at the original source position and one can get better space and time resolution. If a source located at $r_0$ emits a pulse $s(t)$, the $i^{th}$ antenna on the time-reversal array will record $s(t) * h_{r_0 r_i}(t)$, where $h_{r_0 r_i}(t)$ is the impulse response between antennas at $r_0$ and $r_i$. Due to reciprocity, the reverse channel response is identical ($h_{r_0 r_i}(t) = h_{r_i r_0}(t)$). The time-reversed signal at the initial source point $r_0$ is

$$z(t) = k \cdot s(T - t) * h_{r_0 r_i}(T - t) * h_{r_i r_0}(t), \tag{2.1}$$

where k is a constant to normalize the transmit power, and T is a time-delay to make the system causal. The last two terms represent a correlation filter. The correlation function has a maximum at $t = T$. This maximum value is $\int (h_{r_0 r_i}(t))^2 dt$ that corresponds to the

energy of $h_{r_0 r_i}(t)$. The time-reversal system performance improves when used with multiple antennas. The time-reversal waveforms return to the source at the same time, meaning they will have constructive interference and improve the time-reversal peak signal. With N antennas, time-reversal waveform becomes

$$z(r_0, t) = \sum_{i=1}^{N} k_i s(T - t) * h_{r_0 r_i}(T - t) * h_{r_i r_0}(t) \tag{2.2}$$

Time-reversal is a space-correlator as well as a time correlator. In the above analysis, the time-reversal waveform is matched exactly at the original source point $r_0$. If the probe antenna moves away from the source, then the inverse impulse response will change.

$$z(r, t) = \sum_{i=1}^{N} k_i s(T - t) * h_{r_0 r_i}(T - t) * h_{r_i r}(t) \tag{2.3}$$

Similar to time-correlation analysis, as the probe antenna moves away from $r_0$, the uncorrelated terms tend to cancel each other. If the channel is rich in multipath components, the correlation peak will be sharper and we could obtain a sharp focusing spot both in time and in space. In time reversal, due to the time-reversibility of the E& M wave equations, the back-propagated field focuses near the active targets. The antenna array acts as a mirror that refocuses the time-reversed signals back onto the source. The time-reversal method is not limited to focusing on an active source. The back-propagated waves also focus around the passive scattering objects in the complex media. By using an iterative time-reversal method, it is even possible to focus the RF energy on the most reflective object in the medium [16]. In a homogenous medium (see Fig 2.2), the focusing resolution is diffraction limited because of the finite aperture $a$ of the antenna array. The cross-range resolution is given by $\lambda L/a$ [10]. The resolution in the perpendicular direction, the range resolution, is $\lambda(L/a)^2$ [10]. In randomly inhomogeneous media (see Fig 2.3), the focusing resolution is much tighter [9]. This phenomenon is called super-resolution, and is the result of scattering by the random inhomogeneities. In effect, the array behaves as if it has

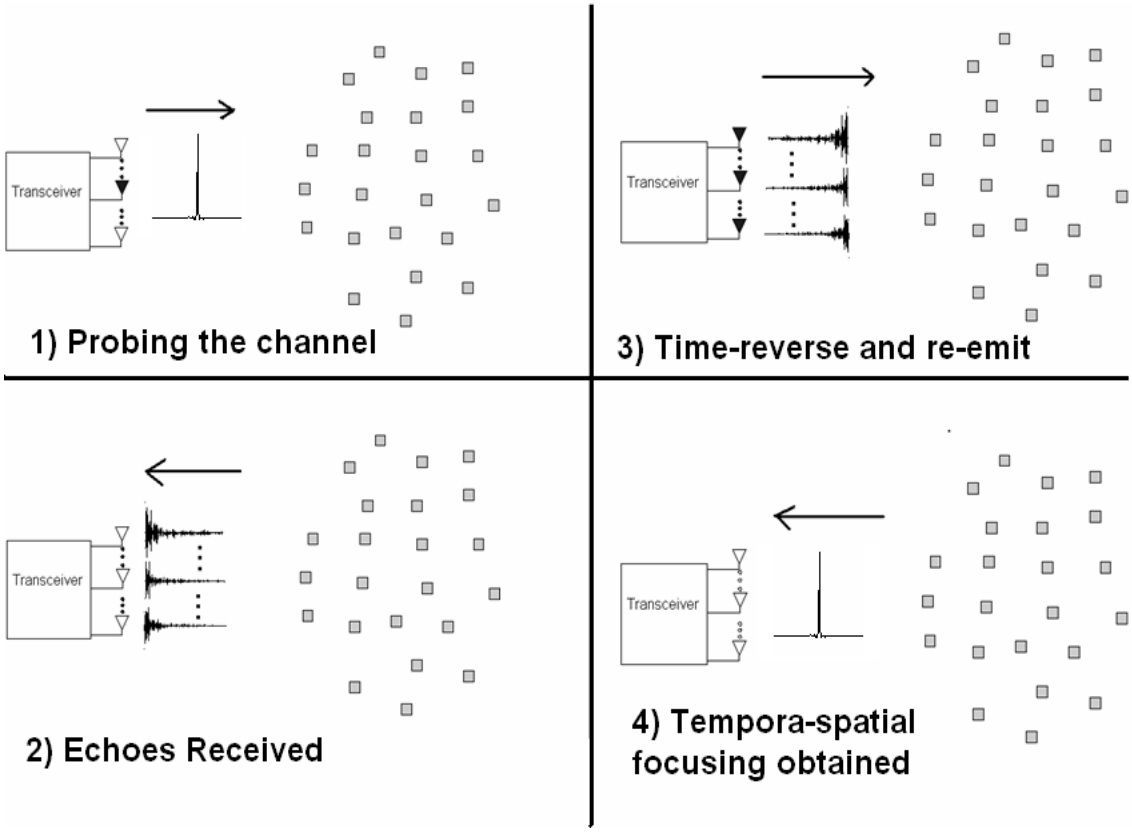


Figure 2.1: The steps involved in a time-reversal process: 1) A uniform pulse is transmitted from a source 2) The signal propagates through the channel and echoes are recorded by each one of the antennas 3) The recorded signals are time-reversed and transmitted back into the medium 4) The probing pulse is restored at the source antenna.

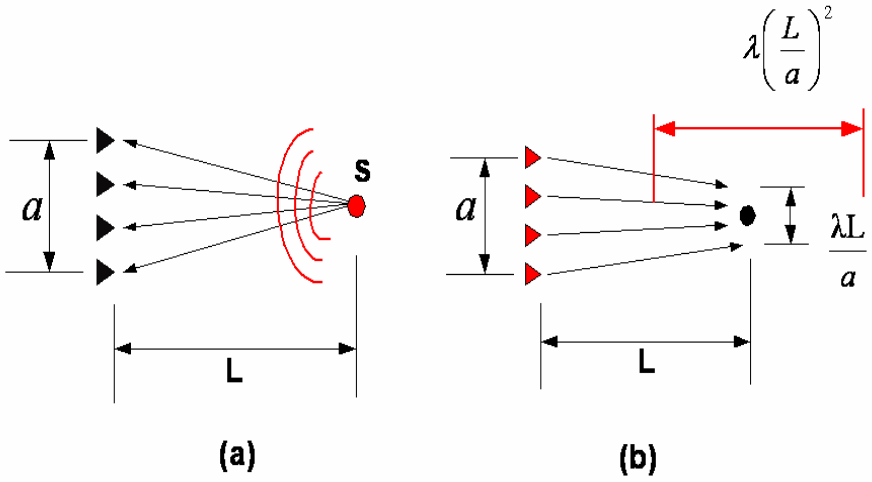


Figure 2.2: Time-reversal in a homogenous environment. (a) A point source at s emits a signal that propagates through a distance of L and received by an array with an aperture size of a. (b) The time-reversed signal is sent back from each one of the sensors in the array. The waves propagate back through the same medium. The spatial focusing is diffraction-limited both in range and cross-range.

an effective aperture larger than its physical size.

## 2.2 Electromagnetic wave propagation simulations in a medium with clutter

By using a simple electromagnetic channel simulator, we will analyze important time-reversal system parameters and in the following sections we will provide experimental demonstrations. The simulations that we have done are based on the Green's function method. We assume that we have point targets. The scalar Green's function between two points is given by

$$g(r,f) = \frac{e^{-j2\pi fr/c}}{4\pi r} \tag{2.4}$$

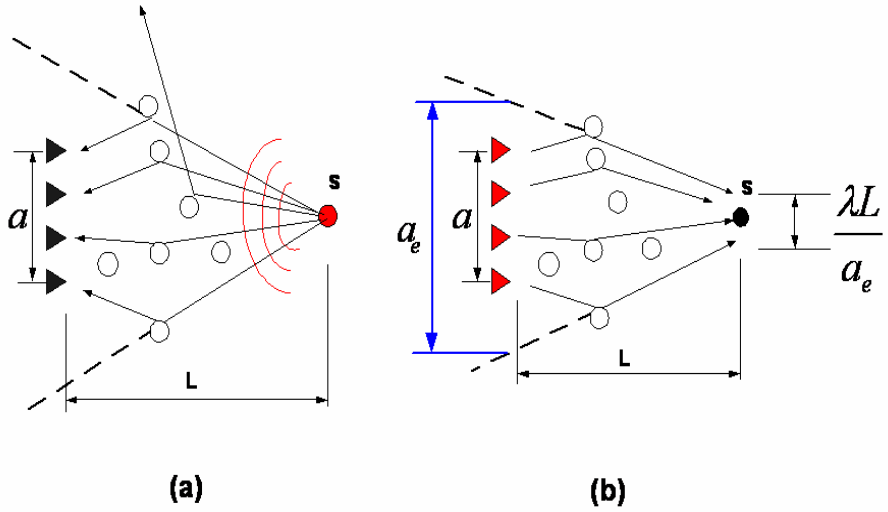


Figure 2.3: Time reversal in a random medium with significant multipath. The array appears to have an effective aperture $a_e > a$ and the focusing of the back-propagated field is tighter.

where f is the frequency of operation and r is the distance between two points. Fig 2.4 shows the simulation setup, where there are $N_A$ transmit antennas, $N_B$ receive antennas, and M scatterers. In the simulation, we take into account first and secondary reflections. Higher order reflections are neglected. The transfer function between $ith$ element of antenna array A and $jth$ element of antenna array B is given as

$$H_{ij} = \sum_{l=1}^{M}(-\frac{\sigma^{1/2}e^{-j\beta(r_{li}+r_{jl})}}{r_{li}\cdot r_{jl}} + \sum_{s=1,s\neq l}^{M}\frac{\sigma e^{-j\beta(r_{li}+r_{sl}+r_{js})}}{r_{li}\cdot r_{sl}\cdot r_{js}}) \tag{2.5}$$

where $\sigma$ is the radar cross-section of the objects, and $\beta = 2\pi/\lambda$ is the wave-number. The advantage of this 3-D simulation method is that the simulation time is independent of the area of the scattering environment. It only depends on the number of scattering objects in the channel. This makes it fast compared to other 2-D or 3-D simulation tools. As previously mentioned, the resolution of a time-reversal system in a homogeneous medium is limited by the Rayleigh resolution. The antenna aperture defines the resolution. Fig 2.5 shows the performance of the time-reversal method in a homogeneous medium using 4 antennas and 8 antennas. The simulations are done using the above model. The value of

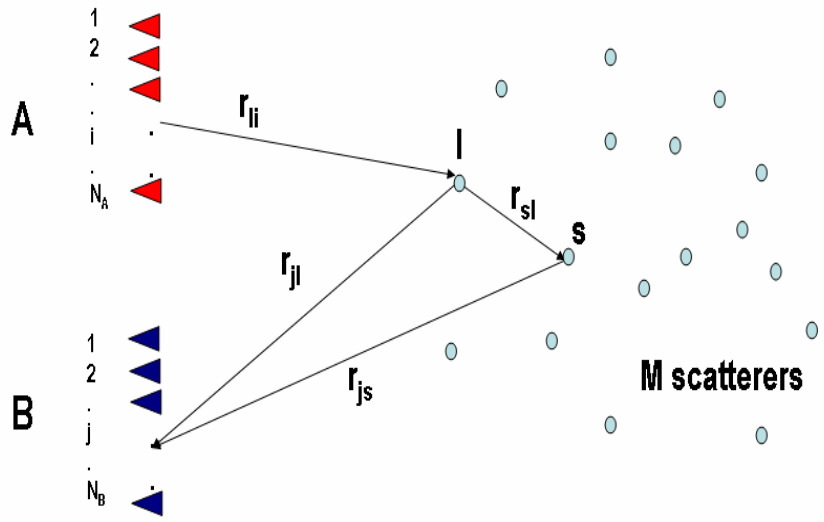


Figure 2.4: The simulation setup.

radar cross section $\sigma$ is chosen to be 0.1. The bandwidth of the probing pulse is 2 GHz between 4 GHz and 6 GHz. The antenna separation is $4\lambda = 24cm$ in both cases. The distance between the antenna array and source is 10 m. The cross-range resolution is 60 cm using 4 antennas and 26 cm using 8 antennas. Grating lobes exist around the central lobe. The separation between the grating lobes and the central lobe is related to the antenna separation in the array. Since we have the same antenna separation in both cases ($\delta x = 24cm$), the first grating lobe is at $\lambda L/\delta x = 2.5m$ from the main beam.

The time-reversal system performance in an inhomogeneous medium results in super-resolution. The scattering objects in the medium increase the effective aperture of the antenna array resulting in a tight range and cross-range resolution. Fig 2.6 shows the time-reversal focusing in the presence of 20 scattering objects. The range resolution is 15 cm and the cross-range resolution is just 4 cm. That shows an improvement of cross-range focusing compared to the homogeneous medium by a factor of 15. Fig 2.7 shows the time-reversal waveform and forward-channel waveform in a homogeneous and inhomogeneous medium that are described in Fig 2.5a and Fig 2.6a. In the homogeneous channel

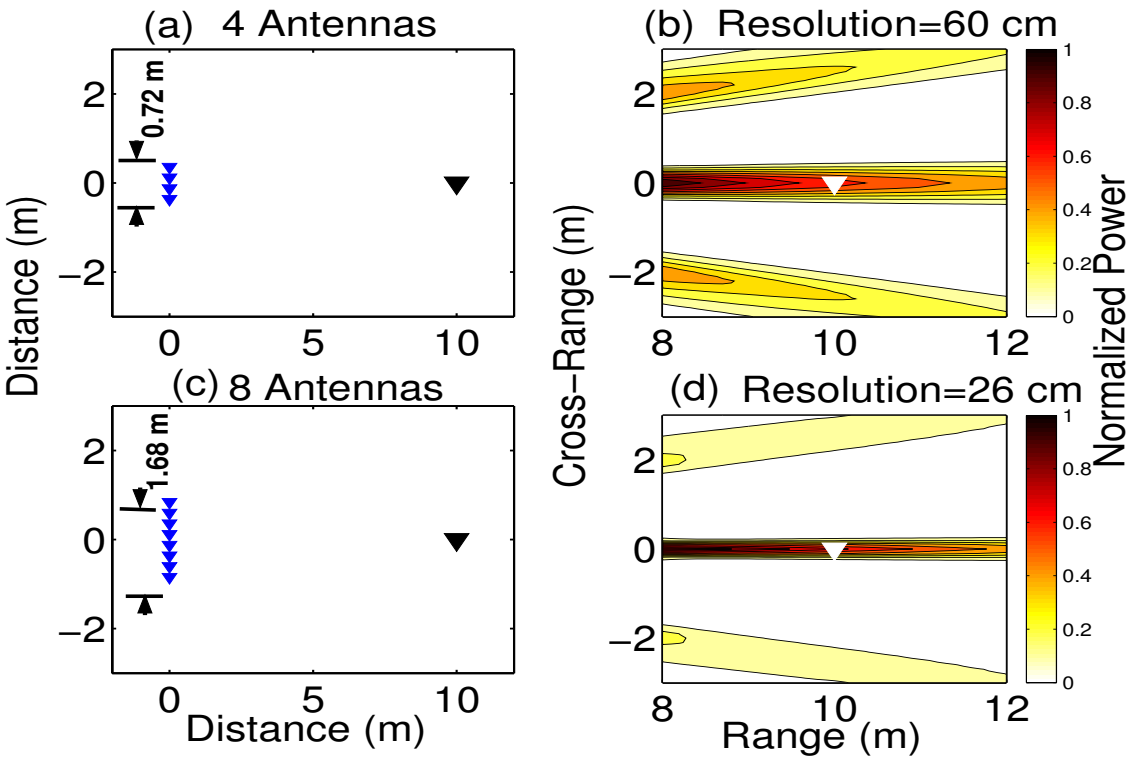


Figure 2.5: The performance of time-reversal method in a homogeneous medium using a)-b) 4 antennas and c)-d) 8 antennas. Antenna separation is 24 cm in both cases.

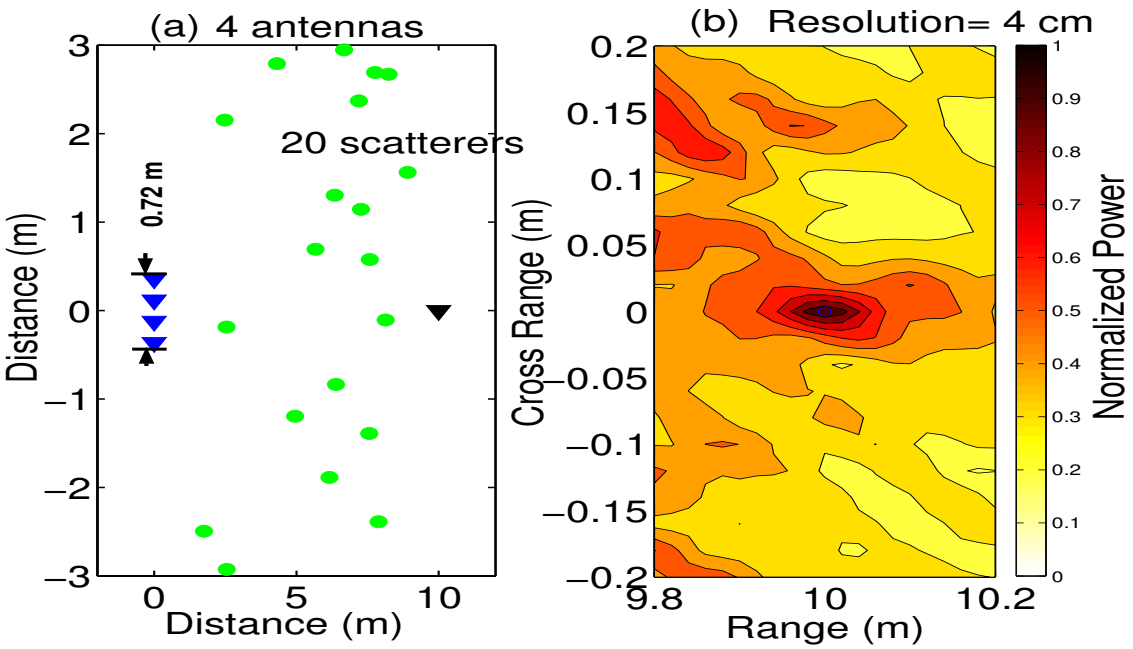


Figure 2.6: The performance of time-reversal method in an inhomogeneous medium using 4 antennas with an antenna separation of 24 cm. a) The simulated geometry b) The focusing around the source antenna

(Fig 2.5a), the forward-channel waveform is obtained by transmitting co-phased signals from each one of the antennas on the array simultaneously and recording the signal received by the target antenna on the right ($\sum_{i=1}^{4} h_i(t)$). The resulting waveform is shown in Fig 2.7a. The time-reversal signal, which is obtained by sending time-reversed waveforms from each element of the antenna array and recording the signal at the target antenna location, looks like the forward waveform since the transmitting antennas are the only source of signal that reaches to the receiver. In the inhomogeneous medium (Fig 2.6a), the scattering objects in the medium make the forward channel waveform dispersive (Fig 2.7b). The time-reversal waveform causes compression of the impulse response and produces a peak signal at time $t = T$. Thus time-reversal caused focusing both in time (Fig 2.7b) and space (Fig 2.6b) in an inhomogeneous medium. As for the homogeneous medium, there is no advantage of a time-reversal based system over conventional beam steering.

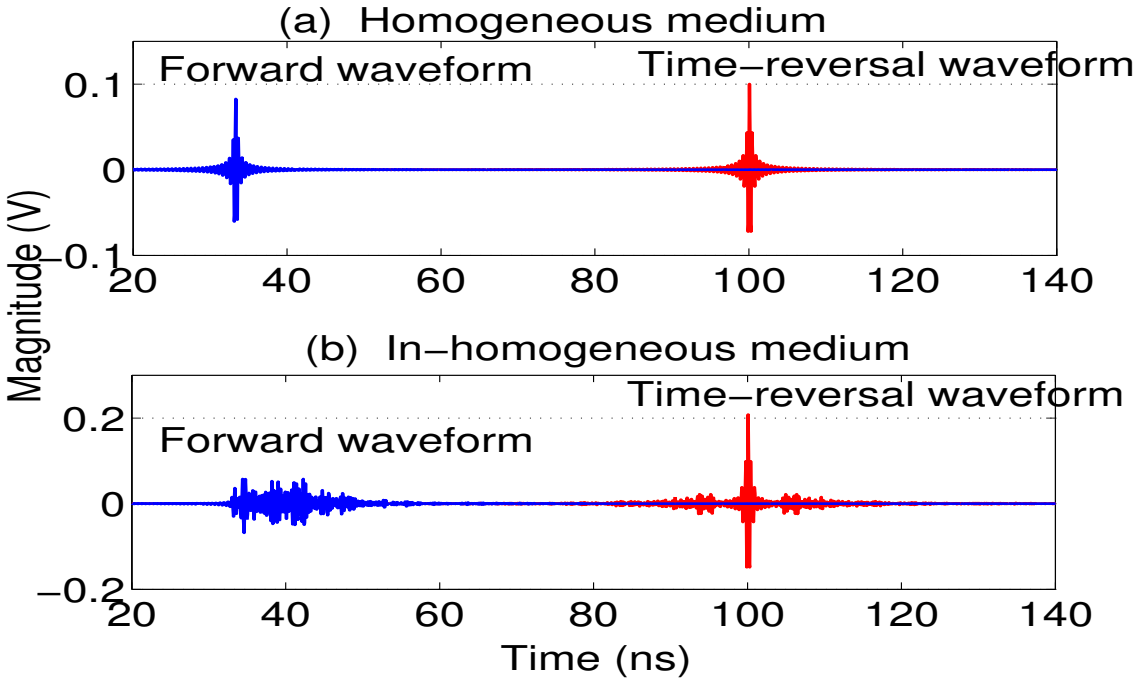


Figure 2.7: Time-reversal waveform and forward-channel waveform in a) homogeneous medium and b) inhomogeneous medium

### 2.2.1 RMS delay spread

The scattering objects in the medium result in multiple signal paths between two antennas in a wireless system. Based on the antenna locations, there can be a direct path as well. Multipath channels are well-known in wireless communications and are typically characterized by the root mean squared (RMS) delay spread $\tau_{RMS}$ and Mean Excess Delay $\tau$, defined as follows [81]

$$\bar{\tau} = \frac{\int_{-\infty}^{+\infty}(t-t_0)P(t)dt}{\int_{-\infty}^{+\infty}P(t)dt} \tag{2.6}$$

$$\tau_{RMS} = \sqrt{\frac{\int_{-\infty}^{+\infty}(t-t_0)^2P(t)dt}{\int_{-\infty}^{+\infty}P(t)dt} - (\frac{\int_{-\infty}^{+\infty}(t-t_0)P(t)dt}{\int_{-\infty}^{+\infty}P(t)dt})^2} \tag{2.7}$$

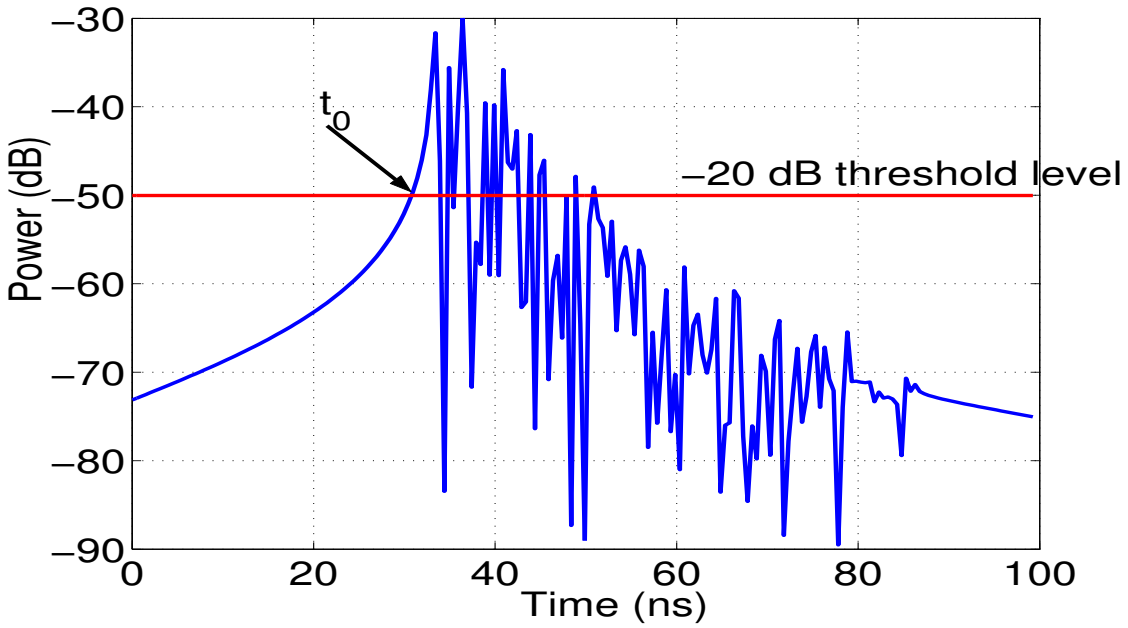


Figure 2.8: Power Delay Profile of the channel between the first element in the time-reversal array and the source antenna in Fig 2.6a.

where P(t) is the power delay profile, and and $t_0$ is the first arrival time above a certain threshold. The power delay profile is a plot of relative received power as a function of time delay. In our analysis, the power delay profile is defined as the square of the impulse response $|h(t)|^2$ between transmitter and receiver. The mean excess delay and RMS delay spread are the first and second central moments of the power delay profile. RMS delay spread is a good measure of the length of the echoes in the channel. To calculate the RMS delay spread and mean excess delay, power threshold levels are defined and the points above the threshold are used to calculate these parameters. In our simulations, the threshold level is set to -20 dB. The power delay profile of the channel between the first antenna on the 4-element array and the source antenna in the inhomogeneous medium of Fig 2.6a is shown in Fig 2.8 along with the -20 dB threshold level. The RMS delay spread is calculated to be 3.2 ns.

### 2.2.2 Coherence Bandwidth

Dispersion in the time domain is equivalent to frequency selective behavior in the frequency domain. The more the time-domain signal has echoes, the more nulls and peaks we observe in the frequency spectrum. The frequency selectivity is measured by a parameter called coherence (correlation) bandwidth. The correlation bandwidth is the statistical average bandwidth over which signal propagation characteristics are significantly correlated. The correlation bandwidth can be obtained by calculating the normalized auto-correlation $R(f)$ of the measured complex frequency function $H(f)$. The correlation bandwidth is defined as [81]

$$R(f) = \frac{\int_{-\infty}^{\infty} H(f+f')H^*(f')df'}{\int_{-\infty}^{\infty} |H(f')|^2 df'} \tag{2.8}$$

where $H(f)$ is the complex transfer function of the channel. $R(f)$ is a measure of the range of frequencies over which the amplitudes in the channel response are correlated. There is a relationship between the coherence bandwidth and RMS delay spread. If the coherence bandwidth is defined as the range of frequencies over which the normalized correlation function $R(f)$ is above 0.5, then the relation between the coherence bandwidth (CB) and RMS delay spread for a Rayleigh fading channel is as follows [81]

$$CB_{0.5} = \frac{1}{5\tau_{RMS}} \tag{2.9}$$

The frequency response and the corresponding correlation function of the channel between the first element of the antenna array and the source antenna in the inhomogeneous medium of Fig 2.6a is shown in Fig 2.9. The 0.5 coherence bandwidth of the channel is approximately 69.6 MHz. Using Equation 2.9, the estimated RMS delay spread is 2.87 ns. As a comparison, the RMS delay spread that we calculated through the power delay profile was 3.2 ns. The simulation results are compared with experimental results for correlation bandwidth calculations in Section 2.3 (Fig. 2.29). The close match between experimental

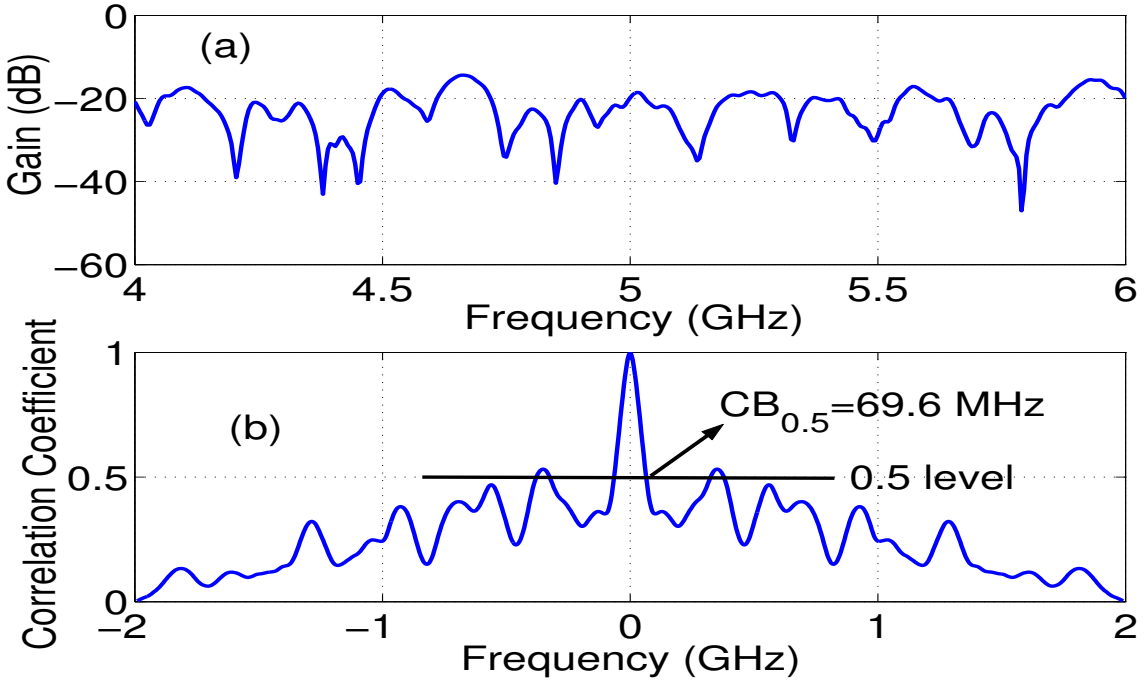


Figure 2.9: a) The channel frequency response b) Autocorrelation response of the channel between the first element in the time-reversal array and the source antenna in Fig 2.6a.

results and simulations show that the simple 2-reflections based simulator can be used to estimate the channel parameters with reasonable accuracy. The correlation bandwidth should be analyzed in environments with various densities of scatterers. For that purpose, Fig 2.10 has been prepared using the simulation tool. In each set-up, a 10 element transmit array and 10 element receive array are used to probe channels with different numbers and densities of scattering objects. The separation between the antennas is 12 cm. The channel response is simulated between each pair of elements in the transmit and receive arrays with different numbers of scattering objects in the medium. The frequency band simulated is 4-6 GHz using 401 points. We start with one single scattering object and increase the number up to 60. The scattering objects are uniformly distributed over four areas and the simulations are repeated for each one of the cases as described in Fig 2.10a-d. The scattering objects are distributed over an area of 0.24 m x 0.24 m, 0.48 m x 0.48 m, 1.2 x 1.2 m and 12 m x 12 m. In a 10 x 10 antenna array, there are 100 possible paths between the elements of the arrays. Each path is taken as a separate channel and the correlation

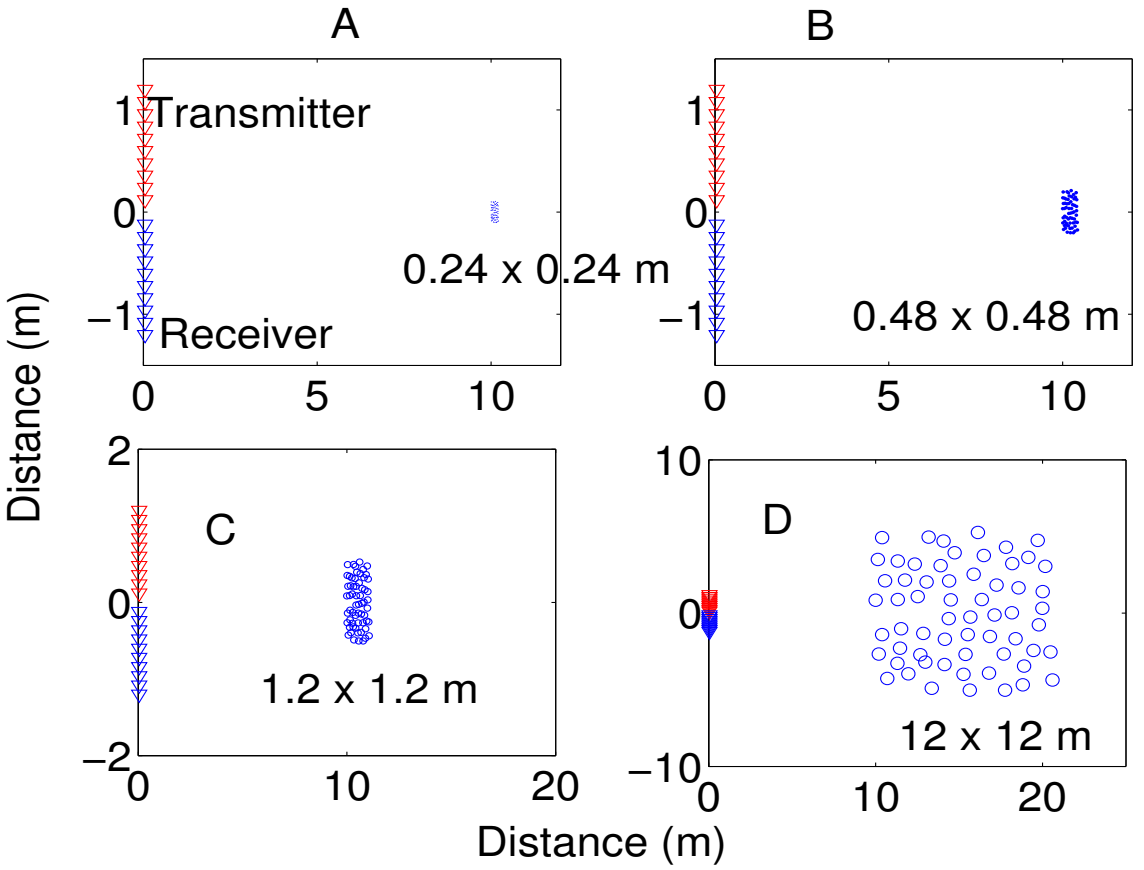


Figure 2.10: Simulation set-ups. 60 scattering objects are used and distributed uniformly across areas of A) 0.24 x 0.24 m B) 0.48 x 0.48 m C) 1.2 x 1.2 m D) 12 x 12 m

bandwidth is calculated for each channel and then averaged.

Fig 2.11 shows the correlation bandwidth for all four cases with different numbers of scattering objects in the medium. The results show that the area covered by the scattering objects is important. Based on the area of the scattering objects, the correlation bandwidth saturates at a certain value. In the case of single object in the medium, the correlation bandwidth is close to 1 GHz and with increasing number of objects the correlation bandwidth becomes smaller. If the area is small (0.24 m x 0.24 m), the correlation bandwidth fluctuates around 500 MHz. If the area is increased by four times, the correlation bandwidth is about 300 MHz, and it is fairly constant even though the number of scattering objects is increased. The correlation bandwidth becomes 100 MHz with an area of 1.2 x 1.2

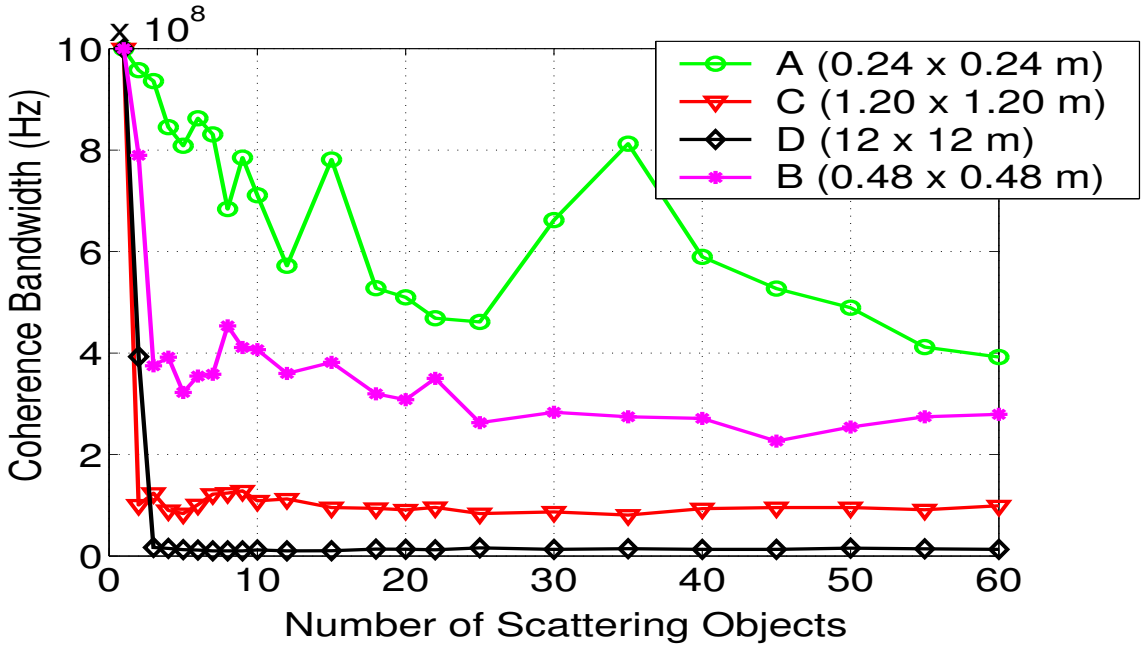


Figure 2.11: Coherence bandwidths as a function of number of scattering objects.

m, and if the area is 12 x 12 m, the correlation bandwidth saturates around 12 MHz. In the simulations, we have used a 2 GHz wide spectrum that has a time-resolution of 0.5 ns corresponding to a spatial resolution of $3{\cdot}10^{8}{*}0.5{\cdot}10^{-9} = 15cm$. That shows that the antennas can not resolve any two objects which are closer than 15 cm. In the case of the smallest area 0.24 m x 0.24 m, even though we packed up the region with 60 scattering objects, their return waveforms all overlap with each other and do not produce any more dispersion in time. That is why the correlation bandwidth is quite high compared to other cases. As the area gets bigger, the separation between the scattering objects becomes larger and each one of the objects in the channel produces unique signature in the time-domain pulse and the aggregate time dispersion increases. That results in lower correlation bandwidth.

### 2.2.3 Singular values

Singular value decomposition is a very powerful technique to investigate the properties of any matrix. In a scattering environment, the channel is probed with multiple antennas. The singular values of the channel matrix can reveal important information such as the

number of objects in the medium as well as the reflection coefficient of each scattering object. The complex channel matrix, K, is formed from the channel responses between N transmit antennas and N receive antennas at a certain frequency. The singular value decomposition of K can be written as

$$K = U \sum V^{\dagger} \tag{2.10}$$

where U and V are unitary matrices and $\sum$ is a diagonal matrix of the singular values of K sorted in descending order, and $V^{\dagger}$ is the transpose conjugate of $V$ [82]. By doing SVD analysis, the channel matrix K is decomposed into a set of independent orthogonal modes of transmission, which are referred to as singular vectors, and each one of the singular vectors has weight defined by the singular values. Fig 2.12 shows the singular values of the simulation setup described in Fig 2.10d. K is a 10 x 10 matrix, and the frequency of operation is at 5 GHz. The number of scattering objects is increased in the medium from 1 to 10 and we plot the significant singular values. As the plot shows, the number of significant singular values is exactly the same as the number of scattering objects in the medium. This shows that the singular values can be used to recognize the number of scattering objects in the medium [48]. The drawback of this method is that the rank of the channel matrix should be greater than the number of scattering objects in the medium to identify each one of the scattering objects. The singular vectors can also be used to do back propagation into the medium for imaging applications [83] as well as selective focusing on the scattering objects in the medium [21].

### 2.2.4 The effect of bandwidth and number of antennas on Time-Reversal focusing

The peak to side-lobe ratio (PSR) of the time-reversal focusing signal depends on the amount of clutter in the channel, the bandwidth of the waveform and the number of antennas in the array. PSR is the ratio of maximum focusing signal to the maximum side-

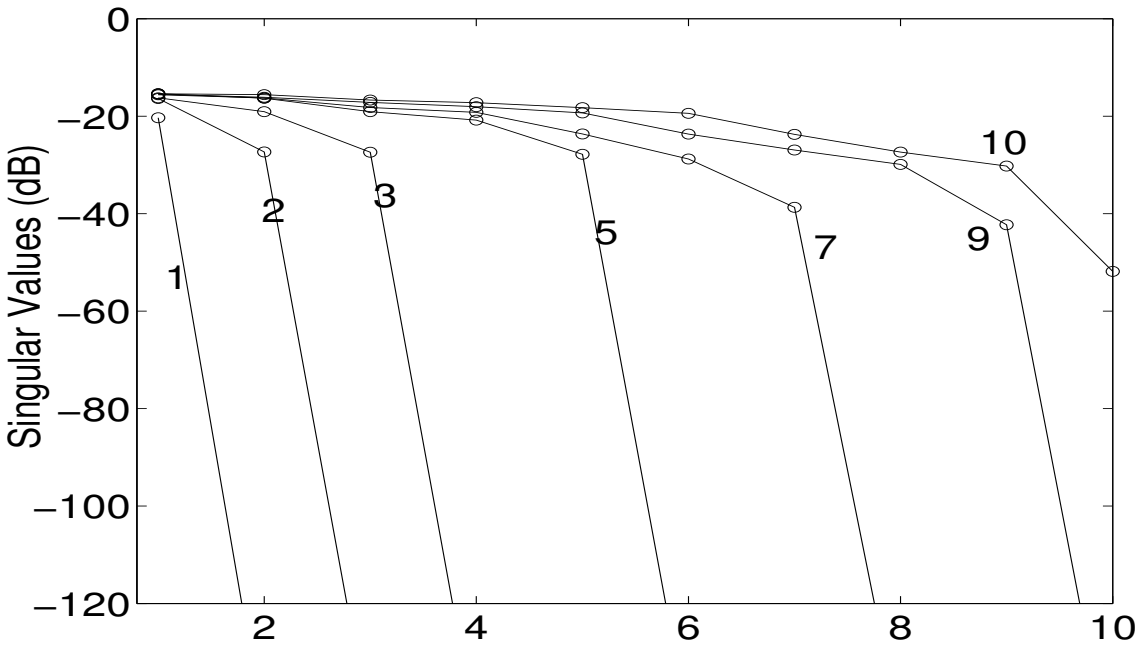


Figure 2.12: The singular values of 10 x 10 antenna array simulation using the setup of Fig 2.10d with increasing numbers of scattering objects in the medium.

lobe level in the time-domain. The PSR improves proportional to $\sqrt{N * \frac{\Delta B}{\delta B}}$ where N is the number of antennas, $\Delta B$ is the bandwidth of the waveform, and $\delta B$ is the coherence bandwidth of the medium [84]. For the analysis of the time-reversal focusing effect in a multipath channel, we assumed a random Rayleigh channel model for which the normalized frequency domain channel response H is given by

$$H = \frac{X + jY}{\sqrt{2 \cdot N \cdot D}} \tag{2.11}$$

where X and Y are normally distributed random variables with zero mean and unity variance, and D is the ratio of total bandwidth to the coherence bandwidth. The channel response is normalized with respect to the number of antennas and the bandwidth. In the case of a single antenna and single frequency point, the power of the complex channel response is 1. Fig. 2.13 shows the time-domain focusing signal through the time-reversal process with different bandwidths and numbers of antennas. As we increase either the

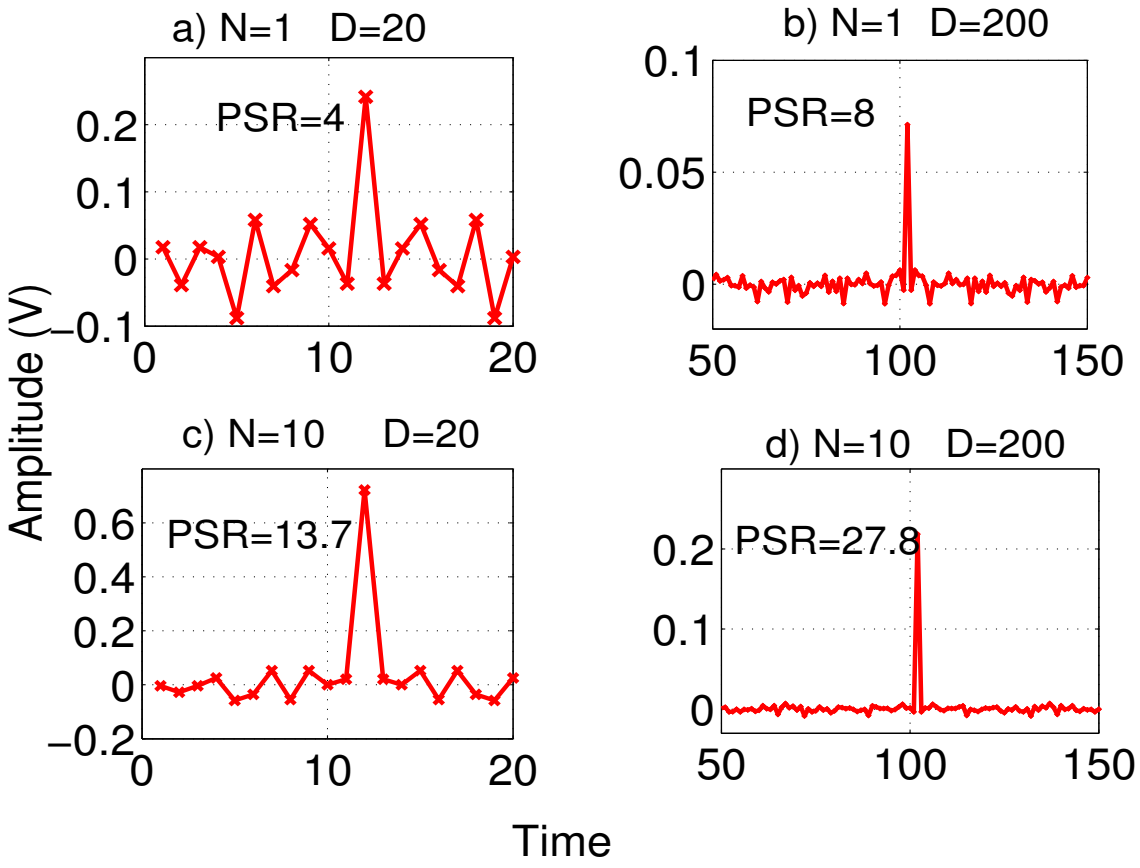


Figure 2.13: The focusing waveform obtained after time-reversal process using a) 1 antenna and 20 frequency points b) 1 antenna and 200 frequency points c) 10 antennas and 20 frequency points d) 10 antennas and 200 frequency points.

bandwidth or the number of antennas, the focusing signal becomes sharper and the PSR improves. Fig. 2.14 shows the PSR gain of the time-reversal focusing signal as a function of the number of antennas and the bandwidth as multiples of coherence bandwidth. From the plot, it is clear that if we have 100 antennas and 1000 independent frequency points, the PSR approaches 180 (=45 dB).

### 2.2.5 Time-Reversal focusing in the presence of noise

Noise affects time-reversal focusing quality. As we increase the noise level, the focusing signal gets smaller compared to side-lobes. The time-reversal process involves a back-propagation part. Due to small scale variations, the channel in the forward ($h_{r_0 r_i}$) and

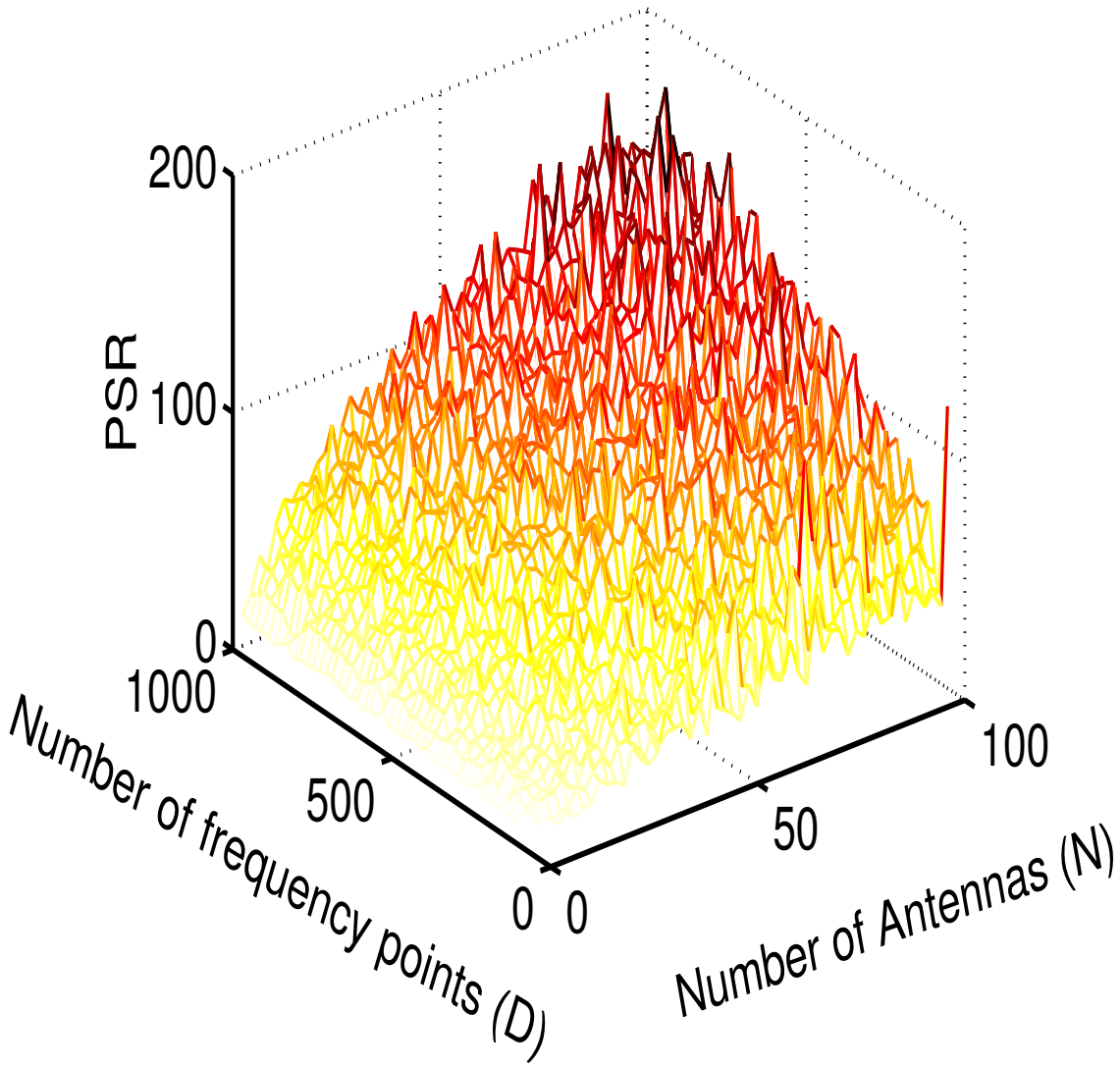


Figure 2.14: The PSR gain of the time-reversal waveform as a function of the number of antennas and number of frequency points.

backward direction ($h_{r_i r_{0'}}$) may not be identical. Below we will analyze the performance of a time-reversal focusing system in a noisy environment. In the simulations, we again used a Rayleigh channel model as described in the previous section. As we increase either the channel variation or the additive noise due to receive circuitry, we observe that the peak-to-sidelobe ratio diminishes. Fig. 2.15 shows the signal flow graph in a time-reversal system assuming channel variation and additive receive circuitry noise. In the forward direction, the time-reversal signal due to an input signal s(t) and channel impulse response h(t) with a variation of $\delta h_1(t)$ is given as

$$y_1(t) = s(t) * (h(t) + \delta h_1(t)) + n_1(t) \tag{2.12}$$

Here we assume that the channel impulse response contains both a stationary component $h(t)$, and a time-varying component $\delta h(t)$. So in the forward direction, the channel variation is characterized as $\delta h_1$, while in the reverse direction, the channel variation is $\delta h_2$. The statistics of $\delta h_1$ and $\delta h_2$ are assumed to be Rayleigh distributed. The additive receiver noise terms are $n_1$ in the forward direction and $n_2$ in the reverse direction. Fig. 2.15 shows the inverse propagation with the time-reversed signal obtained from the previous part. The re-transmitted signal is

$$x(t) = k \cdot [s(T-t) * (h(T-t) + \delta h_1(T-t)) + n_1(T-t)] \tag{2.13}$$

where k is a constant for normalization of re-transmit power. The received signal at the original source point now is

$$y_2(t) = k \cdot [s(T-t) * (h(T-t) + \delta h_1(T-t)) + n_1(T-t)] * (h(t) + \delta h_2(t)) + n_2(t) \tag{2.14}$$

which can also be re-written as

$$
\begin{aligned}
y_2(t) &= [k \cdot s(T-t) * h(T-t) * h(t)] && (2.15)\\
&\quad +[k \cdot s(T-t) * h(T-t) * \delta h_2(t) + k \cdot s(T-t) * \delta h_1(T-t) * h(t) && (2.16)\\
&\quad +k \cdot s(T-t) * \delta h_1(T-t) * \delta h_2(t) + k \cdot n_1(T-t) * h(t) && (2.17)\\
&\quad +k \cdot n_1(T-t) * \delta h_2(t) + n_2(t)] && (2.18)
\end{aligned}
$$

The first term in the square brackets we call the *signal* term (the coherent focusing with no noise or channel variation) and the rest of the terms in the other square brackets we call the *interference* terms (this is the part of $y_2(t)$ that results from noise and channel variations). The $signal-to-interference\ (SIR)$ ratio is defined simply as

$$SIR = \frac{SignalPower}{InterferencePower} \tag{2.19}$$

The time-reversal waveform causes the dispersive components of the forward wave to focus at the same time-instant. So depending on the channel, the time-reversal peak is either equal to or greater than the peak of the forward signal $\{max(y_2(t)) \geq max(y_1(t))\}$. We define the ratio of time-reversal peak to the forward signal peak as the peaks-ratio (PR)

$$PR = \frac{y_2(T)}{max(y_1(t))} \tag{2.20}$$

Here we assume that the time-reversal signal has a peak value at time $t = T$. Similarly another metric to compare the time-reversal focusing to forward signal is through energy calculation across the entire frequency band. In both time-reversal and forward propagation, the same amount of power is being initially transmitted. This is done through introducing $k$ before retransmission of the time-reversal signal. The time-reversal signal changes the waveform such that the maximum energy focuses around the original source. We define the energy ratio (ER) as the power in the received time-reversal waveform to the

Table 2.1: The performance of time-reversal focusing in various noisy environments. The focusing waveforms are shown in Fig. 2.16.

| Cases | a | b | c | d | e | f |
|---|---|---|---|---|---|---|
| $\overline{\lvert h\rvert^2}$ | 1 | 1 | 1 | 1 | 1 | 1 |
| $\overline{\lvert n_1\rvert^2} = \overline{\lvert n_2\rvert^2}$ | 0 | 0 | 0.25 | 0.25 | 1 | 4 |
| $\overline{\lvert \delta h_1\rvert^2} = \overline{\lvert \delta h_2\rvert^2}$ | 0 | 0.01 | 0.25 | 1 | 1 | 1 |
| SIR | - | 18 dB | 1.7 dB | -2.7 dB | -6.3 dB | -13 dB |
| PSR | 10.7 | 9 | 4.6 | 4.5 | 2.1 | 0.5 |
| PR | 7.4 | 6 | 5 | 3.7 | 1.9 | 1.1 |
| ER | 1.9 | 1.8 | 1.7 | 1.1 | 0.9 | 0.98 |

power in the received forward propagation waveform.

$$ER = \frac{\int |y_2(t)|^2 dt}{\int |y_1(t)|^2 dt} \tag{2.21}$$

Fig. 2.16 shows the time-domain time-reversal focusing signal in various levels of noise conditions starting with no noise and incrementally increasing both receiver noise ($n_1$, $n_2$) and noise due to channel variation ($\delta h_1$, $\delta h_2$). Complex Gaussian noise is assumed. In the simulations, we have used a single antenna and 200 independent frequency points. The mean power in the noise sources is shown in Table. 2.1. The SIR values are calculated using Equation 2.18 and 2.19. Fig. 2.16 shows that as the noise is increased, the PSR decreases, and the time-reversal and forward propagation signals start having similar energy levels and peak values. When the SIR becomes -13 dB as shown in Fig. 2.16f, the time-reversal focusing signal is almost buried into noise. The results are summarized in Table. 2.1.

## 2.3 Experimental Characterization of Clutter

### 2.3.1 Data Processing Steps

The experiments were performed using the setup as shown in Fig. 2.17 and 2.18. We have used two horn antennas on both the transmit and receive sides. Each antenna was mounted on a motorized rotary and linear stage controlled via a computer. An Agilent

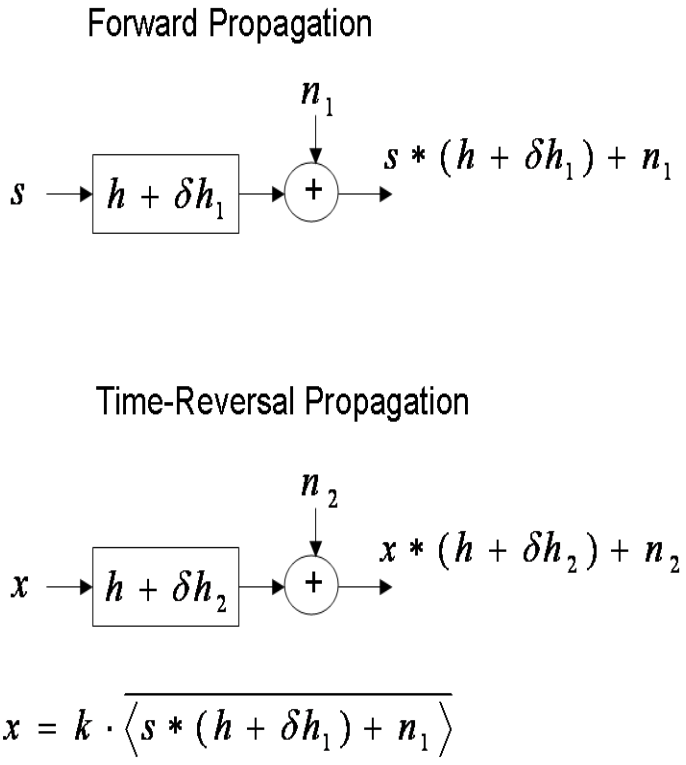


Figure 2.15: The signal flow graph in a noisy time-reversal system. There are two kinds of noise sources. The first one is due to channel variation in forward and reverse directions, and the second one is due to receiver circuitry, additive complex Gaussian noise.

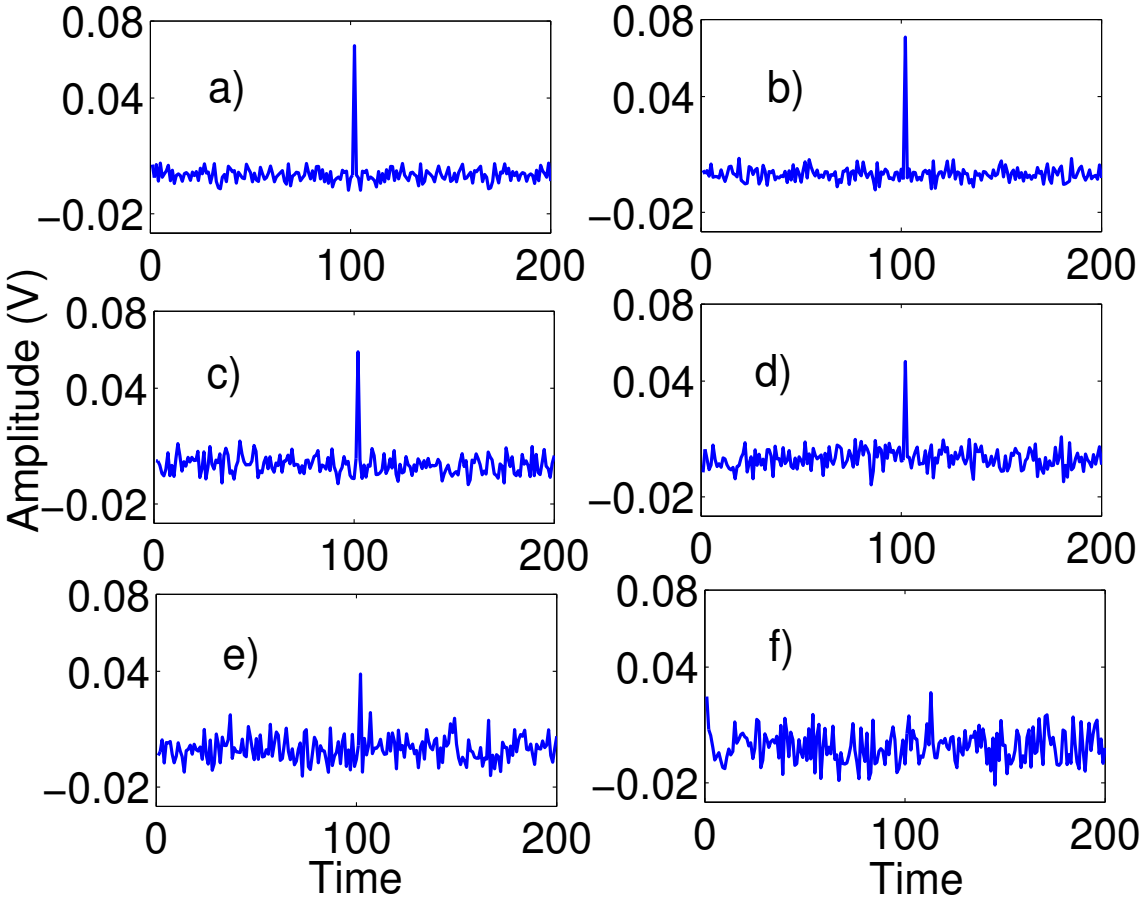


Figure 2.16: The time-domain time-reversal focusing in a noisy environment using single antenna and 200 independent frequency points a) No noise b) SIR=18 dB c) SIR=1.7 dB d) SIR=-2.7 dB e) SIR=-6.3 dB f) SIR=-13 dB

E8358A Vector Network Analyzer (VNA) was used for channel measurements. The frequency of measurement was from 4 GHz to 6 GHz with a resolution of 10 MHz. The antennas were moved in 10.16 cm steps on both rails. 10 points have been used both on the transmit antenna rail and the receive antenna rail. Each data set therefore can be thought of as having been obtained using a virtual array between transmit and receive arrays of 10 elements. We assume that the channel is stationary over the measuring time. (A detailed description of the experimental setup is explained in Appendix A.) We prepared a wood platform (1.22 m by 1.22 m) with holes in it to hold the scatterers. The minimum distance between antenna rail and the wood platform was 2.2 meters, well above the cross-over distance between near and far fields of the horn antennas that is

$$R = \frac{2D^2}{\lambda} \tag{2.22}$$

where $\lambda$ is the wavelength and D is the largest dimension of the transmit antenna. With $D = 13.5$ cm and $\lambda = 6cm$, the far-field cross-over distance for the horn antennas used in the experiment is 0.6 m.

### 2.3.2 Radar Cross Section and Radar Return Power

The power received, $P_r$ in a radar system is affected by many parameters like transmitting power, antenna gain, propagating medium, target cross-section, and receiving system as well as the polarization conditions of transmit and receive antennas. The received power is given as [87].

$$P_r = \frac{P_t G_t}{L_t} \frac{1}{4\pi R^2 L_{mt}} \sigma \frac{1}{4\pi R^2 L_{mr}} \frac{A_r}{L_r} \frac{1}{L_p} \tag{2.23}$$

where $P_r$ is the received power, $P_t$ is the transmitter power, $G_t$ is the gain of the transmit antenna, $L_t$ is the transmitter system loss, R is the distance between transmitter and the object, $L_{mt}$ and $L_{mr}$ are the additional medium losses, $A_r$ is the effective area of the receiver antenna, $L_r$ is the receiver loss, and $L_p$ is the polarization mismatch loss. In our analysis in

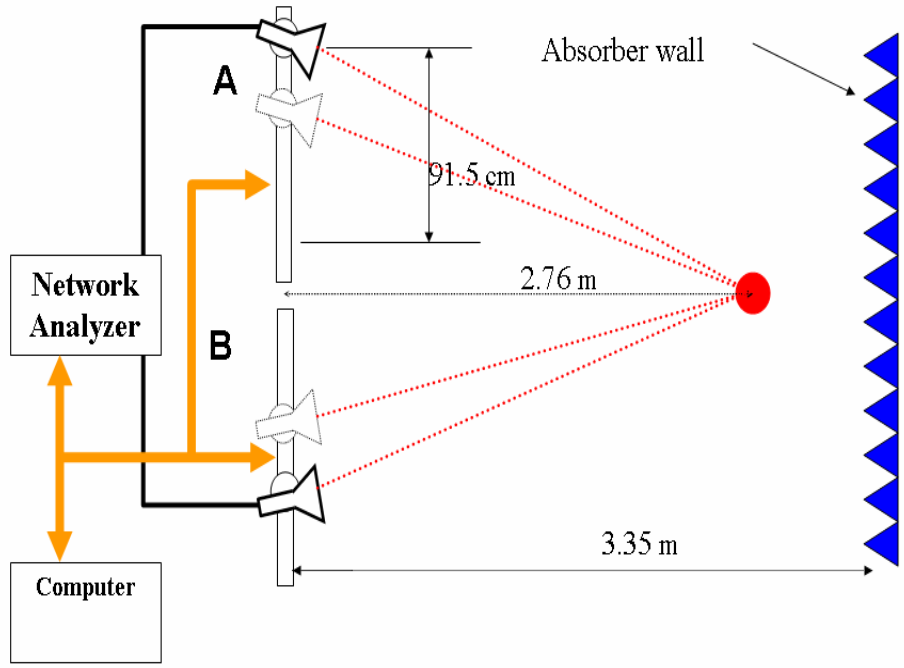


Figure 2.17: The schematics of multistatic radar experimental setup.

Figure 2.18: The photos of multistatic radar experimental setup.

this chapter, we ignore the system losses ($L_t = L_{mt} = L_{mr} = L_r = L_p = 1$). (See Appendix A).

The gain of the antennas could be easily calculated by a simple measurement, where we point two antennas towards each other, and measure carefully the distance between the phase centers of transmit and receive antennas. By using Equation 2.23, we can experimentally determine the gain of the antennas. The effective area of the receive antenna $A_r$ can be written in terms of antenna gain and wavelength as [81]

$$A_r = \frac{\lambda^2 G_r}{4\pi} \tag{2.24}$$

We have used the same antennas for transmitter and receiver, so $G_r = G_t = G$. By inserting Equation 2.24 into Equation 2.23, the gain of the antennas can be calculated as follows

$$G = \sqrt{\frac{(4\pi R)^2 P_r}{P_t \lambda^2}} \tag{2.25}$$

The ratio of $P_r/P_t$ is the channel magnitude response measured by the network analyzer. The gain of the antennas across the 4-6 GHz frequency band is shown in Fig. 2.19a. The gain is about 14 dB at 4 GHz and it increases to 17.5 dB at 6 GHz. Fig. 2.19b shows the measured radiation pattern of the horn antennas at 5 GHz. The 3-dB beam-width of the antenna is 30 degrees. Based on the manufacturing specs on the horn antenna, the usable frequency band is 3.95-5.85 GHz, the gain is 15 dB and 3-dB beamwidth is 33.8 degrees [85]. That means that the horn antennas illuminate a region with 1 m cross section at a distance of 2.2 m. In the case of no scatterers in the medium, minimal echo returns due to the RF absorbing materials on the wall. The scattering objects are 3.2 cm diameter solid dielectric rods and 1.27 cm diameter copper pipes. The dielectric constant of the rods is 3.7. We have also used aluminum plates of different cross-section as extended objects. Fig. 2.20 shows some of the scattering objects that we have used in our experiments. Before going into the details of the complex propagation environment, we first analyze the radar cross-section of scattering objects that are used in the experiments. The radar cross section (RCS)

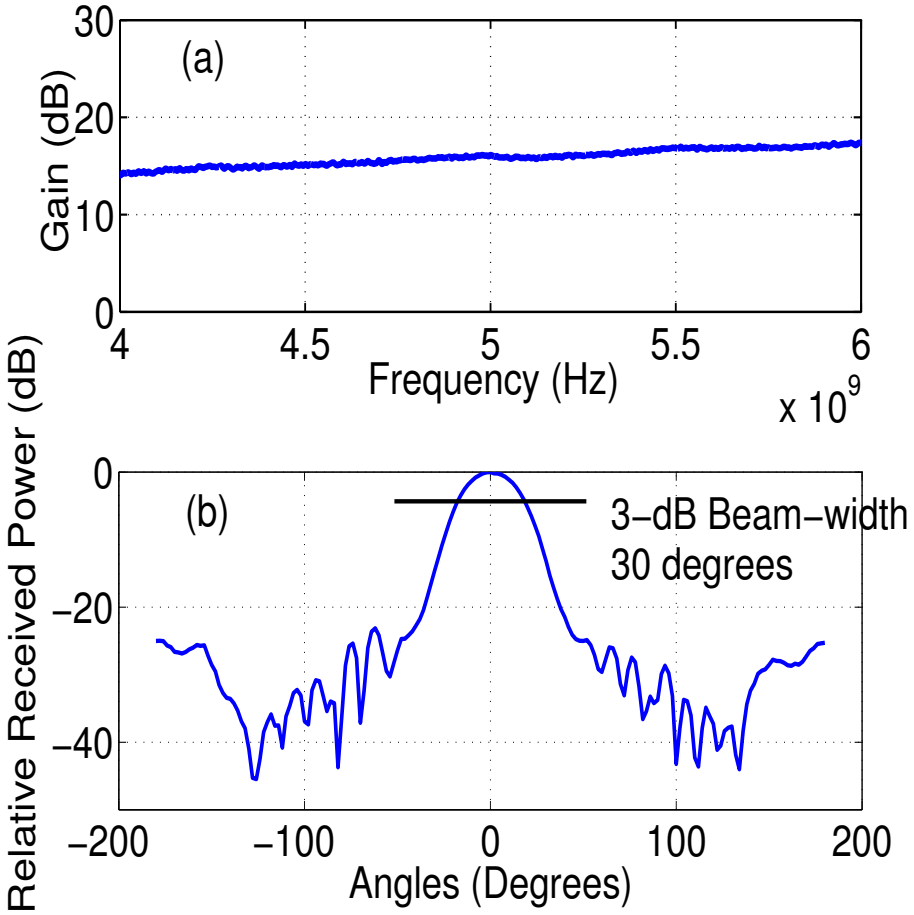


Figure 2.19: (a) The measured gain of the horn antenna across 4-6 GHz frequency band. (b) The measured radiation pattern of horn antenna at 5 GHz.

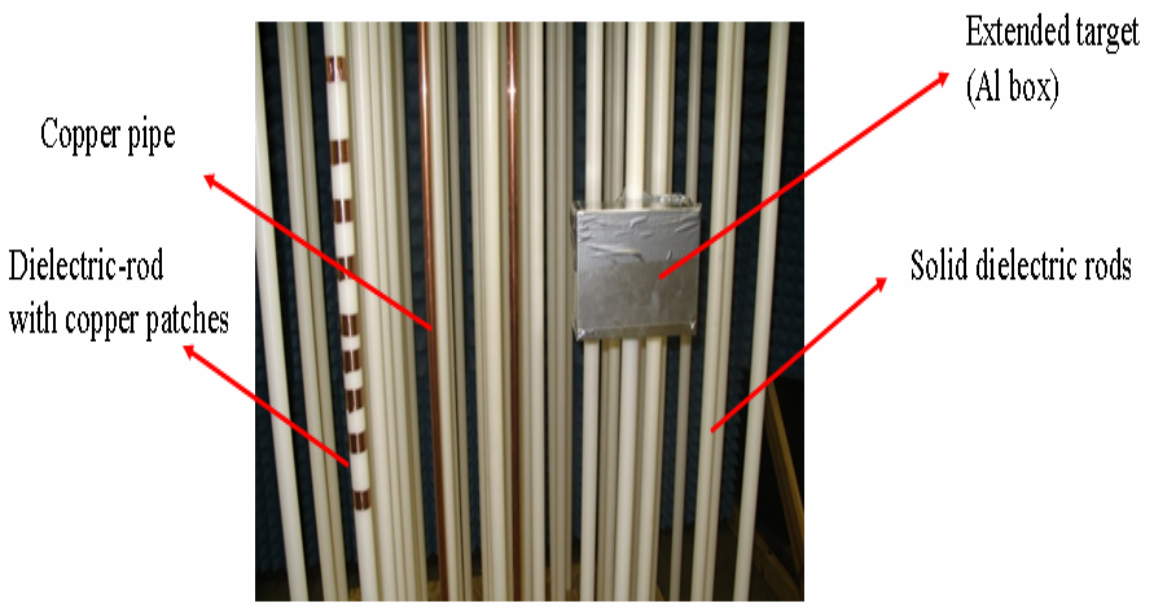


Figure 2.20: Some of the scattering objects used in the experiments.

is a description of how an object reflects an incident electromagnetic wave, and can be extracted from Equation. 2.23 as

$$\sigma = \frac{P_r (4\pi)^2 R^4}{P_t G_t A_r} \tag{2.26}$$

$$\sigma = 4\pi \frac{\frac{R^2 P_r}{A_r}}{\frac{P_t G_t}{4\pi R^2}} \tag{2.27}$$

$$\sigma = 4\pi \frac{\text{power reflected toward source/unit solid angle}}{\text{incident power density}} \tag{2.28}$$

The radar cross section can also be written as

$$\sigma = 4\pi R^2 |\frac{E_r}{E_i}|^2 \tag{2.29}$$

where R is the distance between radar and target, $E_r$ is the reflected field strength at the radar, $E_i$ is the strength of the incident electric field at the target site. For an arbitrary object, the RCS is highly dependent on polarization of the incident wave, the angle of in-

cidence, the angle of observation, the geometry of the target, the electrical properties of the target, and the frequency of operation. The RCS of various objects have been analyzed theoretically, simulated numerically, and measured experimentally [88],[87],[89]. In this section, we will analyze the radar cross-section of long cylindrical objects and compare them with our experiments. The RCS of an infinitely long circular conducting cylinder with electric field parallel to the cylinder axis has been analytically derived starting from the Maxwell's equations [87]. There are two regions of operation where the authors derived simple closed form expressions. These are when the wavelength is much larger than the radius of the cylinder (Model A) and when the radius of the cylinder is much greater than the wavelength (Model B). The closed form expressions are given by [87].

$$\sigma = \begin{cases} \frac{\pi^2 a}{k_0 a[ln(0.8905 k_0 a)+pi^2/4]} & k_0 a << 1, \\ \pi a & k_0 a > 20 \end{cases} \tag{2.30}$$

where $k_0$ is the wave number ($2\pi/\lambda$), and a is the radius of the cylinder. When the radius of the cylinder is very small compared to the wavelength, the RCS is sensitive to the $k_0 a$ parameter. If the radius of the diameter is much greater than the wavelength, the RCS becomes independent of the operating frequency. We have measured the bi-static radar cross section where transmit and receive antennas were 40 cm apart, and each antenna was rotated towards the target which was 2.7 m away from the mid-point of antennas. The comparison between analytical and experimental results have been made. In the experiments, four 2.4 meters long cylinders were used. Even though the cylinders are finite length, the horn antennas are highly directional, illuminating only the mid-part of the cylinders. The four cylinders used in the experiments are a) 0.635 cm radius copper pipe b) 1.6 cm radius dielectric rod c) 1.6 cm radius rod wrapped with Aluminium foil. d) 15.25 cm radius duct. The unitless $k_0 a$ parameters at 5 GHz are 0.66, 1.67, 1.67 and 16 respectively. Fig. 2.21 shows the experimental radar return from each one these objects and the predicted return power by using the radar return power expression of Equation 2.23 along with radar cross section expressions presented in Equation 2.30. Model A refers to the case where $k_0 a << 1$

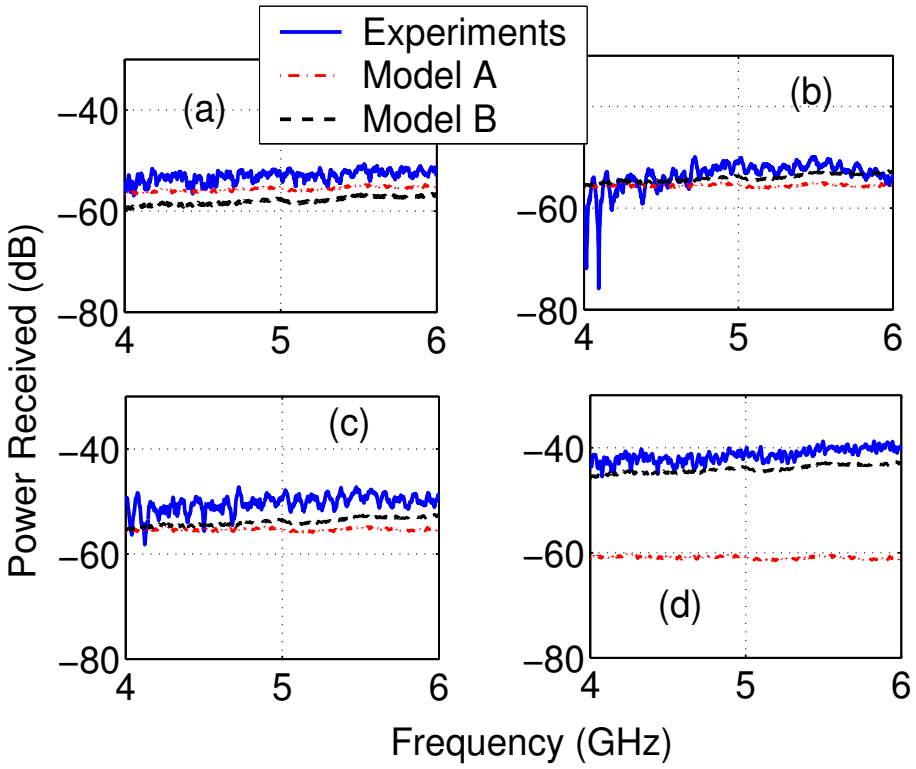


Figure 2.21: The radar return power of different diameter cylinders a) Copper pipe of diameter 1.27 cm b) Solid Dielectric pipe of diameter 3.2 cm c) Aluminum pipe of diameter 3.2 cm d) Steel metal duct of diameter 30.5 cm.

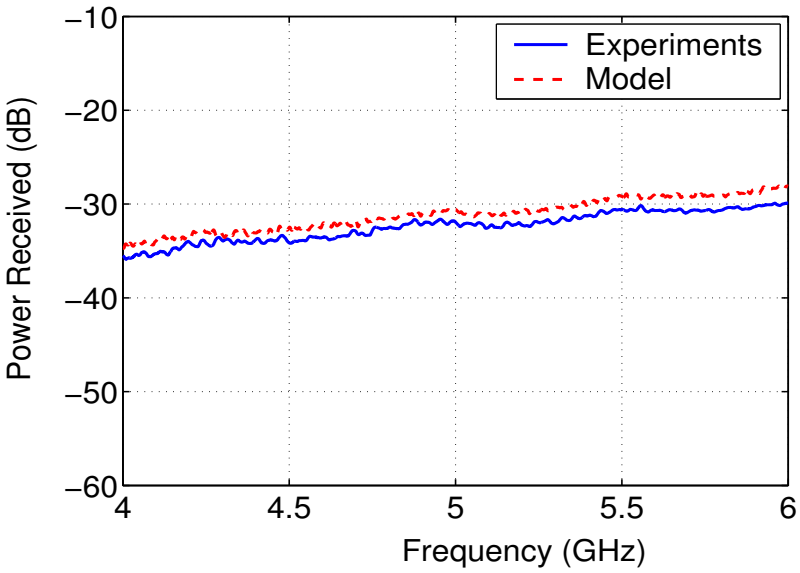


Figure 2.22: The radar return power of Aluminium plate with cross-sections 30 x 17.5 cm.

and Model B refers to the case where $k_0 a > 20$. In Fig. 2.21a, $k_0 a = 0.66$, model A gives a slightly better match to the experimental result. Fig. 2.21d shows the other extreme case where Model B estimates the radar return power better than Model A. That is due to the fact that the cross-section of the duct is larger than the wavelength, so the radar cross-section becomes a constant. The radar cross section expressions are valid for conducting cylinders. In Fig. 2.21b, we compare the expected power return of a conducting cylinder with a dielectric rod. The dielectric material caused some frequency selectivity especially on the lower side of the band, where the wavelength is bigger.

The RCS for a perfect metal plate is given as

$$\sigma = 4\pi a^2 b^2 / \lambda^2 \tag{2.31}$$

where a and b are the cross section of the plate, and the wavelength $\lambda$ is assumed to be smaller than $a$ and $b$. Fig. 2.22 shows a comparison of experimental radar return with the model predicted using the above equation.

After explaining the radar cross-section of individual scattering objects, we can start

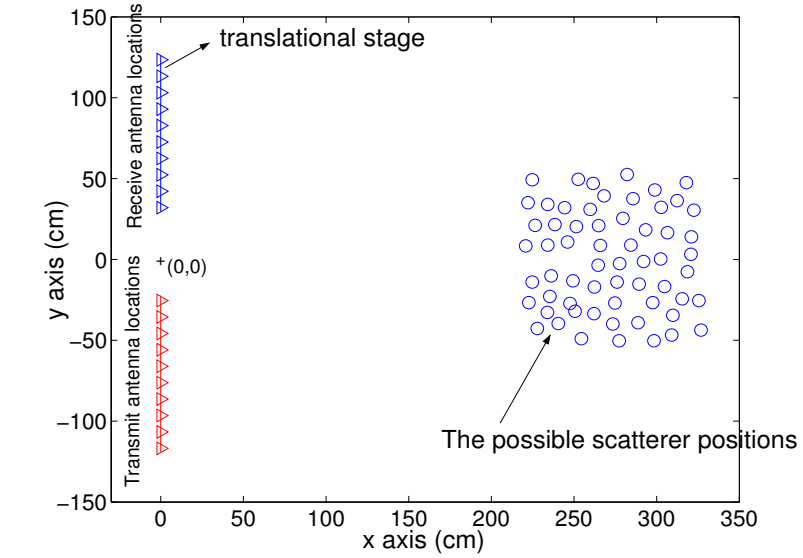


Figure 2.23: We have made 59 holes on the wood platform to hold the scatterers straight.

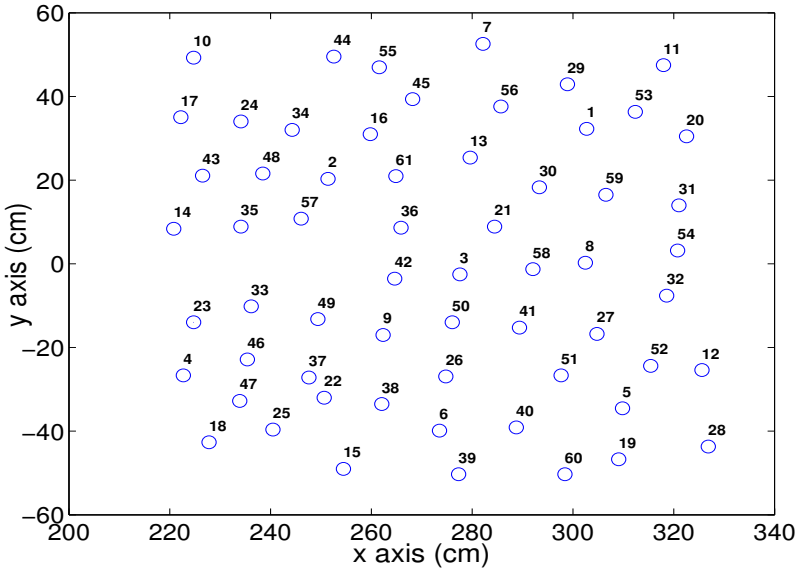


Figure 2.24: The index of positions of the holes on the wood-platform.

discussing the statistical parameters of the complex propagation environment where we have many scattering objects in the medium and the antennas are moved on the linear stage to record the complex channel response from different observation points. The position of holes on the wood platform and the antenna array are shown in Fig. 2.23 and Fig. 2.24. The positions on the wood platform have been indexed as shown in Fig. 2.24. The experimental process can be described as follows: We place a dielectric rod in the medium, make frequency domain measurements by moving the antennas along the rails and record the 10 x 10 complex channel matrix. We repeat the same procedure for different numbers of scattering objects in the medium. The average received power depends on the number of scattering objects in the field and their corresponding radar cross sections. The average power received in the case of multiple objects can be estimated (neglecting multiple scattering) as

$$\frac{\bar{P_r}}{P_t} = \frac{1}{Q} \sum_{i=1}^{Q-1} \sum_{j=1}^{M} \frac{G_{t_i} G_{r_i} \lambda_i^2 \sigma_j}{(4\pi)^3 R_j^4} \tag{2.32}$$

where $P_r$ and $P_t$ are the average received and transmitted powers, $G_t$, $G_r$ are transmit and receive antenna gains, $\lambda$ is the wavelength, $\sigma_j$ is the radar cross section of the $jth$ object, $Q$ is the number of frequencies, and $M$ is the number of scattering objects in the medium. Note that the averaging is performed across all frequency points. In the case of a single target, the wave propagates through the air and reflects back from the target (e.g. a 1.27 diameter copper pipe) and is received by the receive antenna. The returned echo is a delayed version of the transmitted waveform since the cross-section has negligible dispersion (Fig. 2.25a), and a matched filter provides the optimum detection. Note that a Kaiser filter with degree 6 is used to shape the frequency domain response before taking the IFFT to obtain the impulse response. Fig. 2.25 shows the RF representations of the received waveforms. As the number of scattering object increases, the return echo from the medium becomes more complicated. Fig. 2.25b shows the return signal when there are 46 objects in the range of the radar antenna. When there are many objects in

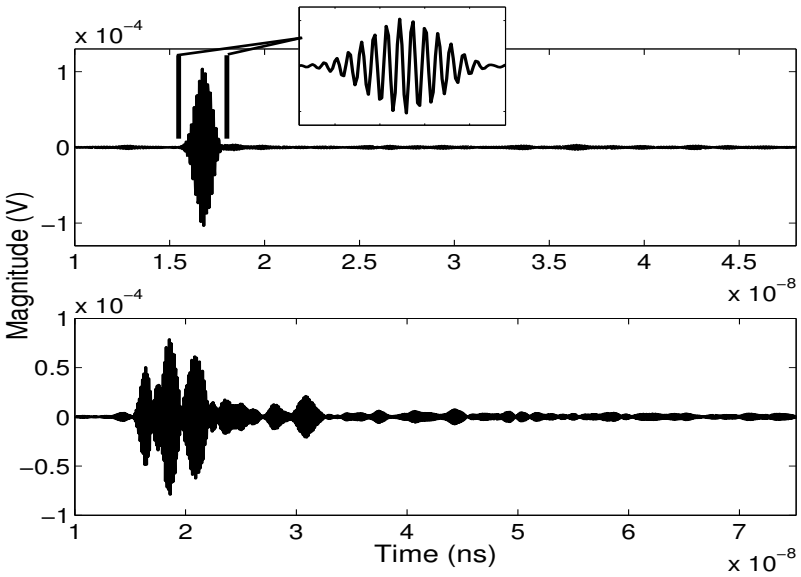


Figure 2.25: RF representation of radar return signals due to (a) single copper pipe and (b) 46 dielectric rods in the medium. A Kaiser filter with degree 6 is used in thr frequency domain response.

the field, as we will show in Chapter 5, matched filter performance deteriorates. We will also show that, in this kind of environment, the time-reversal detection scheme performs very well. As we increase the amount of scattering objects in the field, we also increase the average return power, since what we do effectively is to increase the effective radar cross-section of the medium. Fig. 2.26 shows the return power as a function of the number of scattering objects in the medium. For each case, the 10 by 10 complex channel matrix has been recorded, corresponding to 100 instantiations of the medium from slightly different angles. The dashed line shows the mean power across the 2 GHz frequency band and the error bars show one standard deviation of the return power, determined from the 100 instantiations. The results show that the average mean power increases by 15 times as we increase the number of scattering objects from 1 to 59. The increase is not linear as a function of the number of scattering objects since the antennas do not illuminate all the scatterers in a similar fashion. Some of the objects are partially or completely blocked by other scattering objects, and the scatterers have different distances to the antennas ($R$ in the denominator of Eqn. 2.23). Fig. 2.27 shows the singular values of the measured complex

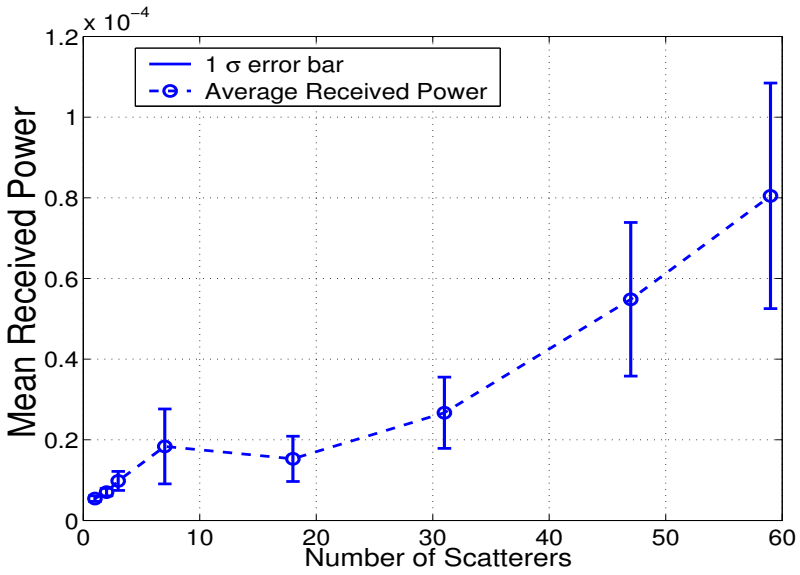


Figure 2.26: The average radar return power versus the number of scattering objects in the medium.

bi-static channel matrix with different numbers of scattering objects in the medium. The SVD values are calculated at a frequency of 5 GHz. The results confirm that the number of significant svd values corresponds to the number of scattering objects in the medium if the number of scattering objects is less than the rank of the channel matrix.

### 2.3.3 Correlation Bandwidth

Fig. 2.28a shows the frequency response of a single dielectric rod of diameter 3.2 cm in the medium and Fig. 2.28b is its normalized autocorrelation function computed using the same frequency band. The dashed line shows the correlation coefficient of 0.5 level, which is the 3-dB power level of the auto-correlation function. For a single scatterer in the medium, the 0.5 level correlation bandwidth is 910 MHz and is limited simply by the frequency window. Fig. 2.28c and 2.28d show the frequency spectrum of 46 dielectric rods randomly placed on a 1.2 m by 1.2 m wood platform (Fig. 2.18). The frequency response shows frequency selective behavior and the auto-correlation function has a much sharper central lobe compared to the previous case. The 0.5 level correlation bandwidth is 118 MHz. This means that the minimum spacing between the frequencies must be 118 MHz so that the responses

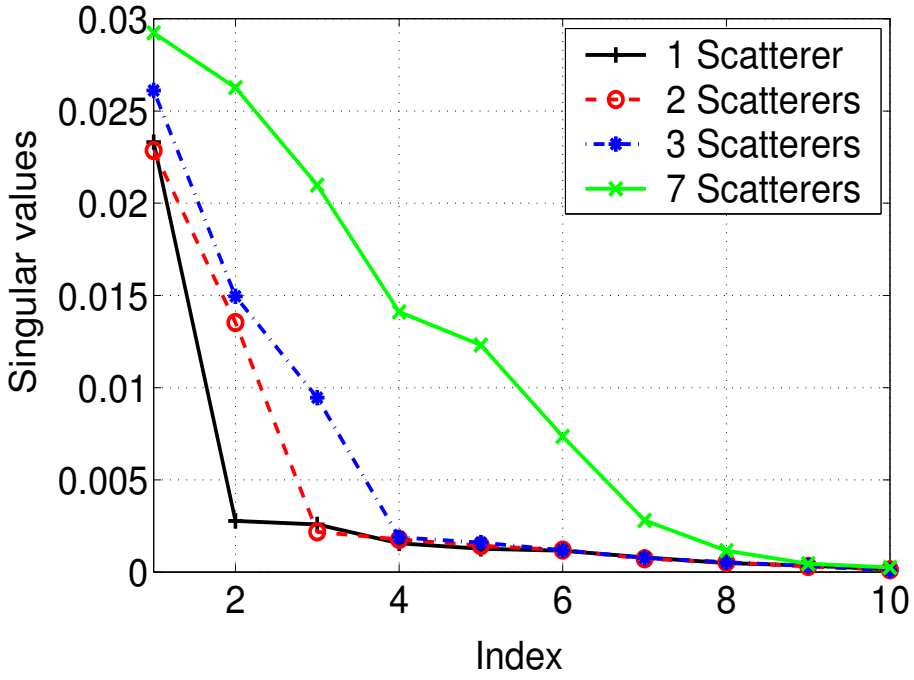


Figure 2.27: Singular value decomposition of mediums with different numbers of scattering objects.

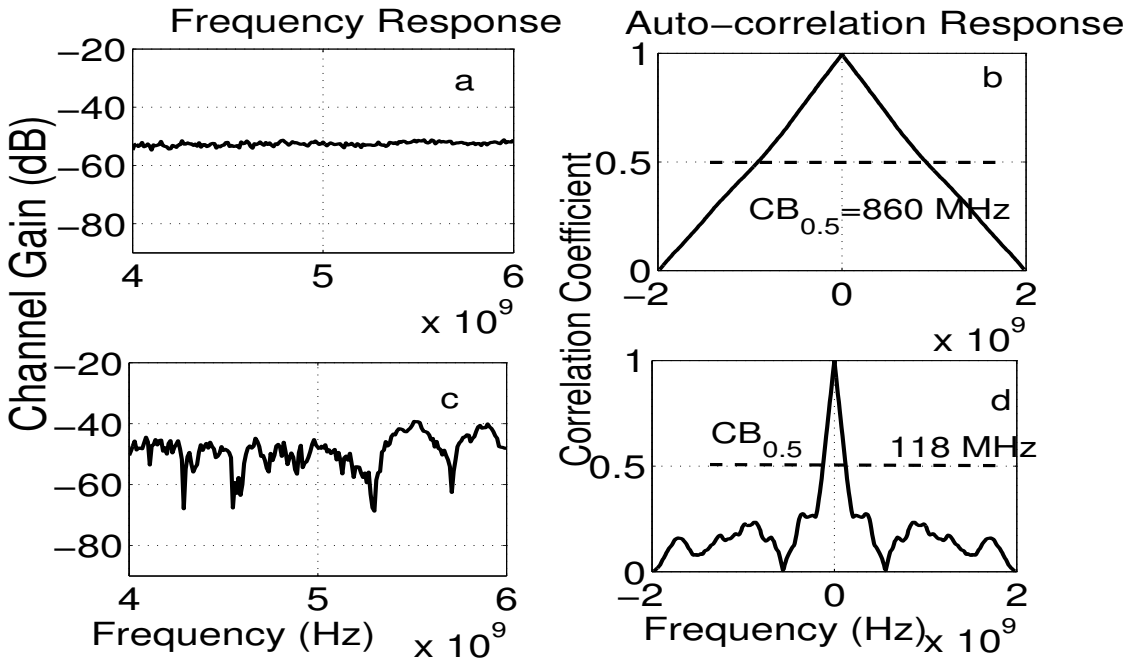


Figure 2.28: The frequency response and autocorrelation response of one dielectric rod (a),(b) and 46 dielectric rods (c),(d) in the channel.

measured at different frequencies are sufficiently independent. The auto-correlation function enables us to calculate the maximum allowed number of frequency samples using a bandwidth of B. As long as the frequency samples are separated from each other by a coherence bandwidth or more, independent information will be obtained from each sample. The more independent samples the channel provides, the more the focusing we can achieve using a time-reversal system. The results show that as we increase the number of scattering objects in the medium, the correlation bandwidth becomes smaller, which means we can have more independent data samples for a given bandwidth.

Fig. 2.29 shows the correlation bandwidth of the “clutter+target" and “(clutter+target)-clutter" channels as a function of number of the scattering objects. The “clutter+target" is called gross channel response, while “(clutter+target)-clutter" is called change detection channel response. In the change detection response, the clutter is subtracted from the gross channel response and the target-only response remains. The correlation bandwidths are computed for each instantiation of 100 channels formed by the 10 by 10 complex matrix. The dashed line shows the statistical average of 100 instantiations and the solid error bars show the amount of deviation from the mean value. In the case of a single scattering object, the mean correlation bandwidth is about 850 MHz, and as we increase the number of scattering objects the correlation bandwidth values drop, saturating at around 20 scatterers. As we increase the number of scattering objects beyond 20 there is minimal change in the value of correlation bandwidth. The fact that the correlation bandwidth of the "clutter+target" channel is very similar of “(clutter+target)-clutter" channel suggests that the medium defines the correlation bandwidth parameter. Even if we do clutter subtraction and concentrate on the target only response, the echoes from the target to the clutter define the correlation bandwidth. Using the target only response after clutter subtraction, we also compare the peaks of time-reversal and change detection signals. Fig. 2.30 shows the ratio of the peak of the time-domain time-reversal waveform to the peak of the change detection waveform for different numbers of scattering objects in the medium. In the case where there is a single object in the medium, time-reversal and change detection should

produce similar waveforms, because there is no dispersion in the medium. As the number of scattering objects increases, the dispersions also increase, making the time-reversal waveform sharper in time as well as focusing tighter in space. As a consequence, the ratio increases with scattering objects, saturating beyond about 30 scattering objects. Note the correlation between Fig. 2.30 and target response of Fig. 2.29. They are inversely proportional, confirming that the time-reversal system performance is indeed a strong function of dispersions in the medium. Fig. 2.30 also shows the TR peak gain over CD as a function of inter-scatterer spacing. Inter-scatterer spacing is found by calculating the shortest distance between the neighbor scattering objects and taking the average. The calculation of the mean inter-scatterer spacing for 59 scattering objects in the medium is illustrated in Fig. 2.31. Since the maximum area of the scattering objects is fixed, as more scattering objects are added to the region, the inter-scatterer spacing becomes smaller. The figure suggests that the TR gain increases until the inter-scatterer spacing is about 4 $\lambda$. If the spacing becomes less than that, the TR gain saturates. This has a close relation with the resolution distance. Using a 2 GHz wide pulse, the resolution time is 0.5 ns, and the resolution distance is 15 cm. The fact that TR gain saturates when the inter-scatterer spacing becomes smaller than $4\lambda = 20cm$ suggests that the antennas can not identify the scattering objects if they are closer than 20 cm and time-reversal gain saturates. The time-reversal gain compared to change detection improves as the bandwidth of the waveform is increased. There is a strong correlation between $TR/CD$ gain to the number of independent frequency samples. Fig. 2.32a shows the auto-correlation of a target response where the target is inside 30 scattering objects. The clutter is subtracted first and the target only response obtained. The correlation bandwidth is 141 MHz, meaning that there are $2GHz/141MHz = 14$ independent frequency samples across the band. Fig. 2.32b shows the $TR/CD$ peak gain with different numbers of frequency samples. The gain improves until the number of frequency points is 20 and saturates afterwards. The initial estimate of 14 independent frequency samples suggests that the bandwidth should be sampled based on the correlation bandwidth. Note that there is approximately $30\%$ variation in the $TR/CD$ gain across the

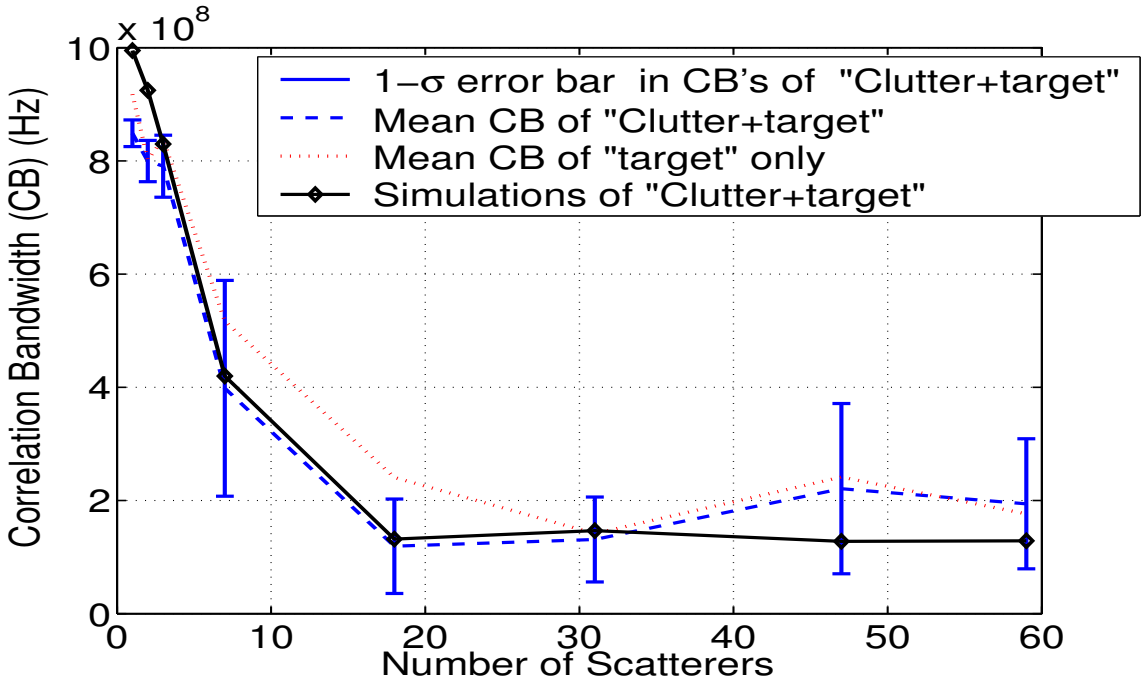


Figure 2.29: The correlation bandwidth as a function of number of scattering objects in "clutter+target" channel as well as "target only" channel after the clutter is subtracted.

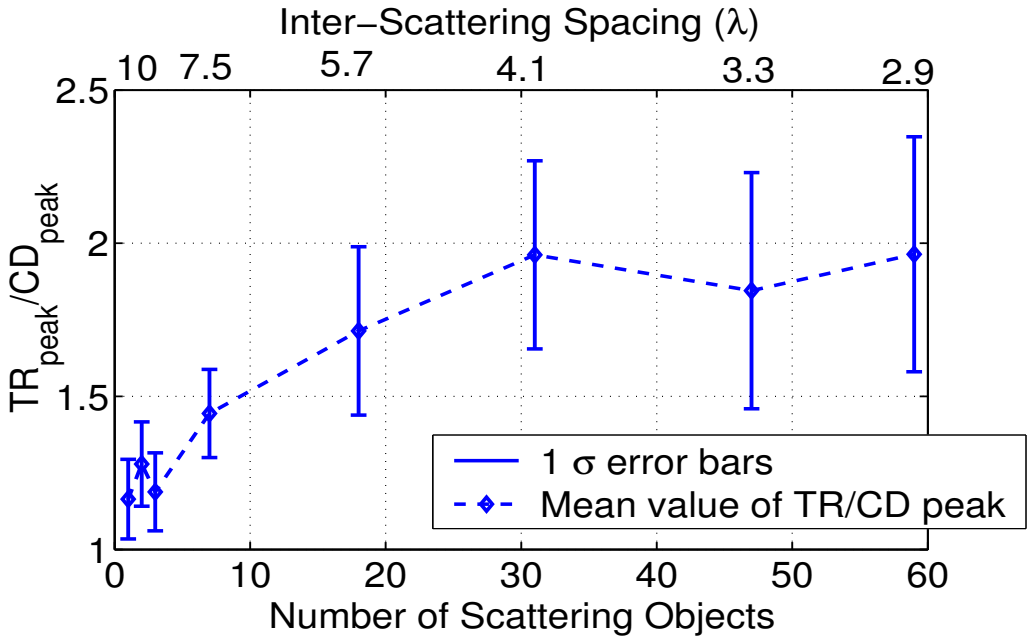


Figure 2.30: The ratio of time-reversal peak to change detection peak as a function of number of scattering objects and inter-scatterer spacing.

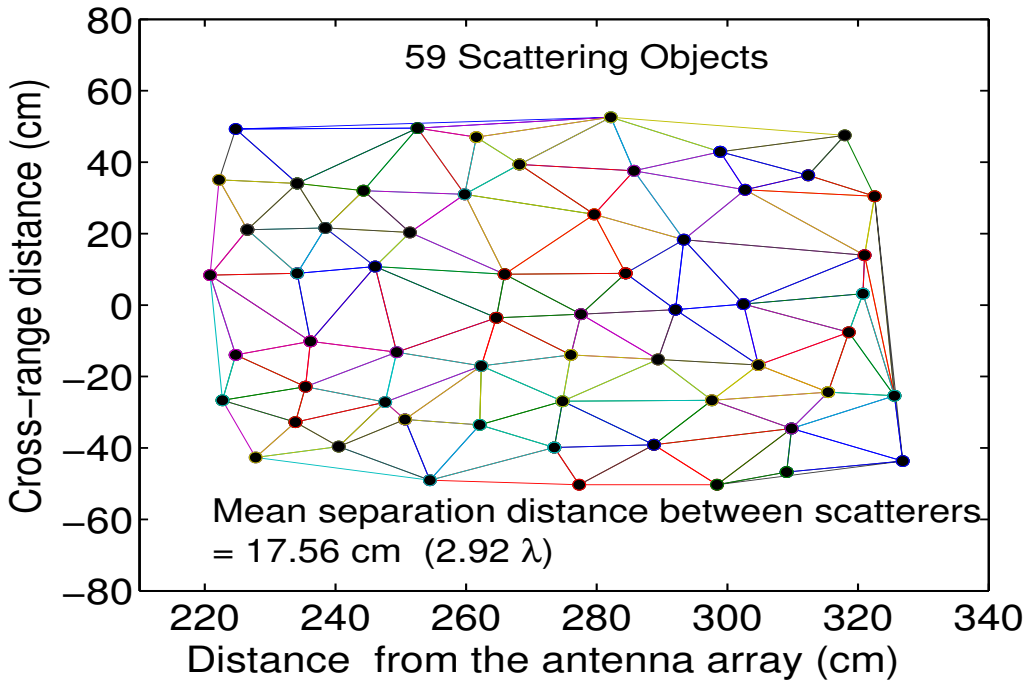


Figure 2.31: The inter-scatterer spacings with 59 scattering objects in the medium,

100 channels that we have recorded. Antenna position plays a big role in the time-reversal system performance and can cause up to $30\%$ deviation from the mean value.

### 2.3.4 Correlation distance

Time-reversal methods work to improve the super-resolution capability in a rich multipath environment. By using a wide-band signal, we can improve the signal to noise ratio of the focusing signal. The bandwidth to the correlation bandwidth ratio gives the number of independent measurements available in a given band. The super-resolution capability can be enhanced by using multiple antennas as well. The more antennas we have, the sharper is the focusing signal. The antennas should be separated such that there is minimal correlation between two antenna locations. The normalized spatial autocorrelation function at a single frequency f is given as

$$R(x) = \frac{\int_{-\infty}^{\infty} H(x+x')H^*(x')df'}{\int_{-\infty}^{\infty} |H(x')|^2 df'} \tag{2.33}$$

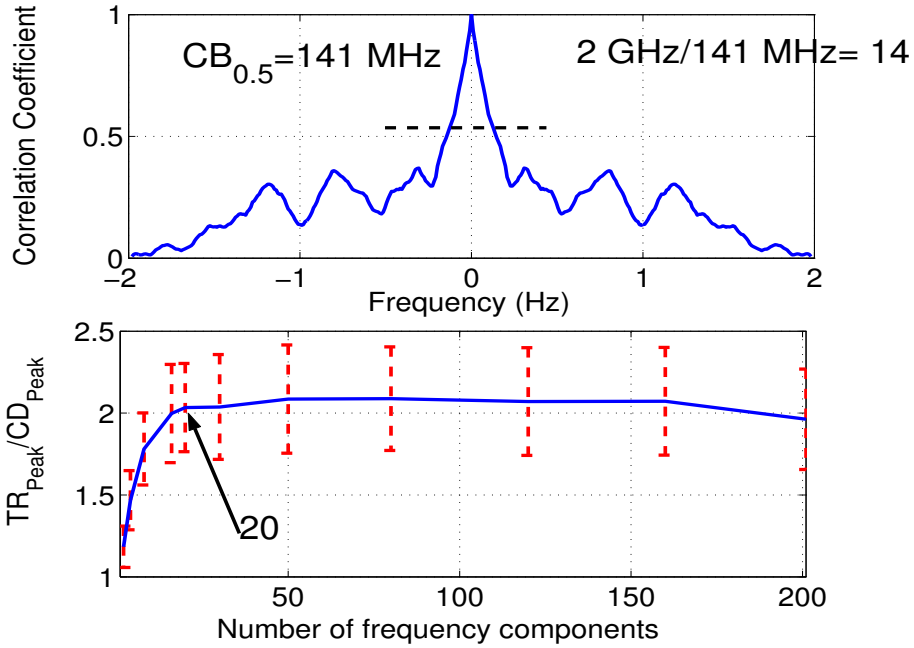


Figure 2.32: The effect of number of frequency samples on TR to CD gain.

We have also done experiments to calculate the spatial correlation in various scattering environments. The experiments were done using two horn antennas and a linear stage. In these experiments, we fixed the position of one of the horn antennas and moved the other one by 1 cm increments for 50 points (Fig. 2.33). For each antenna location we have recorded the complex channel response between 4 to 6 GHz. The mid-point was taken as a reference and as we move to either side, the correlation value drops down. If we move sufficiently away from the reference point, the correlation value drops below the 0.5 level. Fig. 2.34 shows the spatial and frequency correlation of two different channels. In Fig. 2.34a we have just one single dielectric rod in the channel, and in Fig. 2.34b there are 59 dielectric rods in the medium. The central point is the darkest spot in each plot and as we move away from the mid-point in either the vertical or horizontal directions, we lose the coherence. The vertical axis shows the spatial correlation while the horizontal axis shows the frequency correlation. In the case of a single object in the channel, the frequency correlation is about 900 MHz and the spatial correlation is 35 cm. As for the 59 scatterers case, the frequency correlation is 119 MHz while the spatial correlation is 9 cm. These

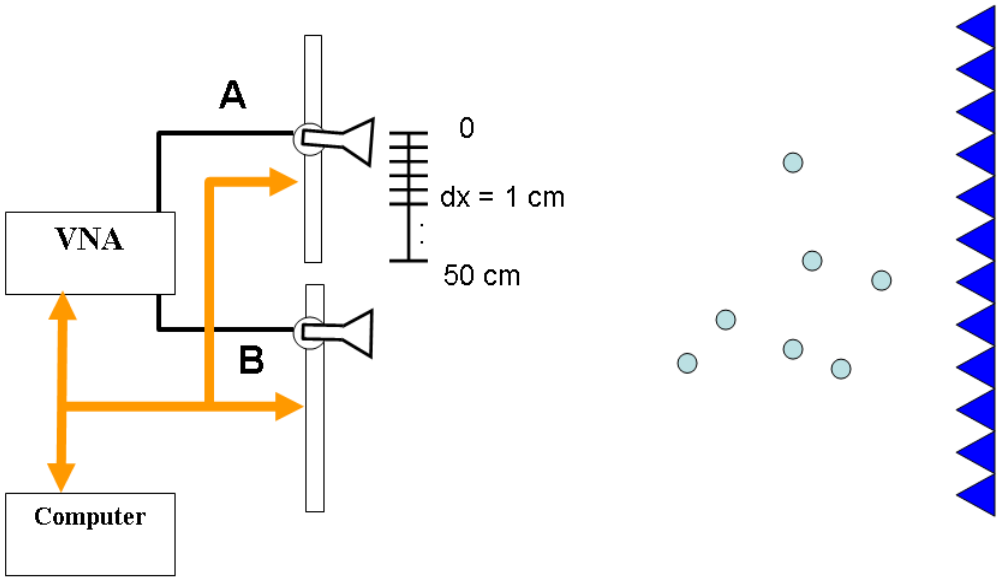


Figure 2.33: The schematics of radar experimental setup for spatial correlation measurements.

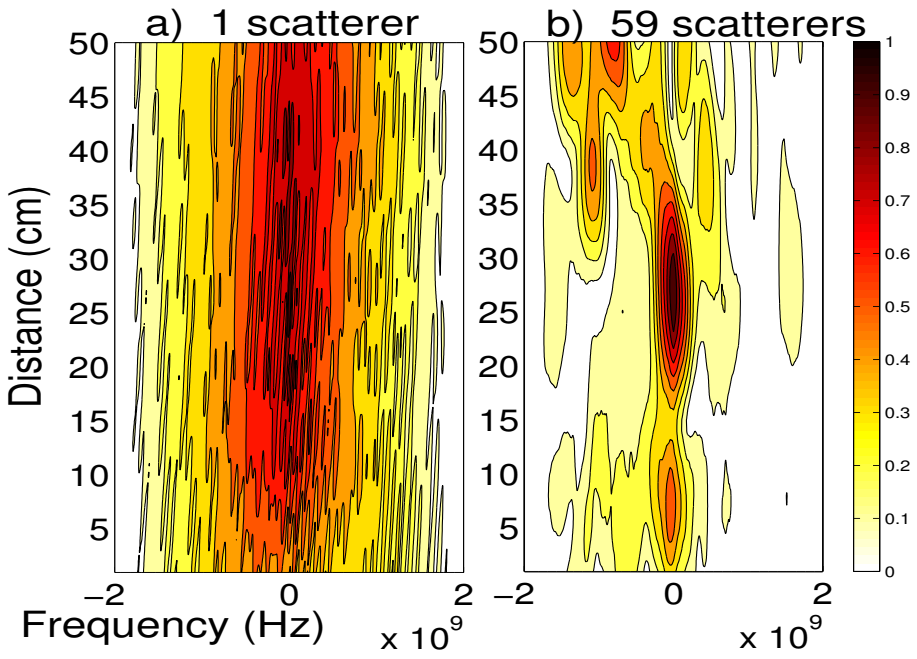


Figure 2.34: The frequency and spatial correlation of a channel that has (a) single scattering object, (b) 59 scattering objects.

results show the minimum frequency separation and spatial distance that we should use to ensure independent measurements. Fig. 2.35 shows the correlation distance for different numbers of scattering objects in the medium. The plot suggests that for smaller numbers of scatterers, the correlation distance is limited by the spatial sampling window to about 35 cm. As the number of scattering objects is increased the correlation distance decreases, reaching a value of about 9 cm with 20-30 scattering objects in the channel.

## 2.4 Conclusions

The time-reversal system performance is a strong function of the propagating medium. The amount of clutter and the distribution of clutter affect the time-reversal focusing. The clutter channel has been analyzed and the main parameters that affect time-reversal system performance have been discussed. The analysis, simulations and experiments have been conducted to characterize the propagating medium. Key parameters such as coherence bandwidth, spatial correlation, bandwidth, frequency of operation, and the numbers of

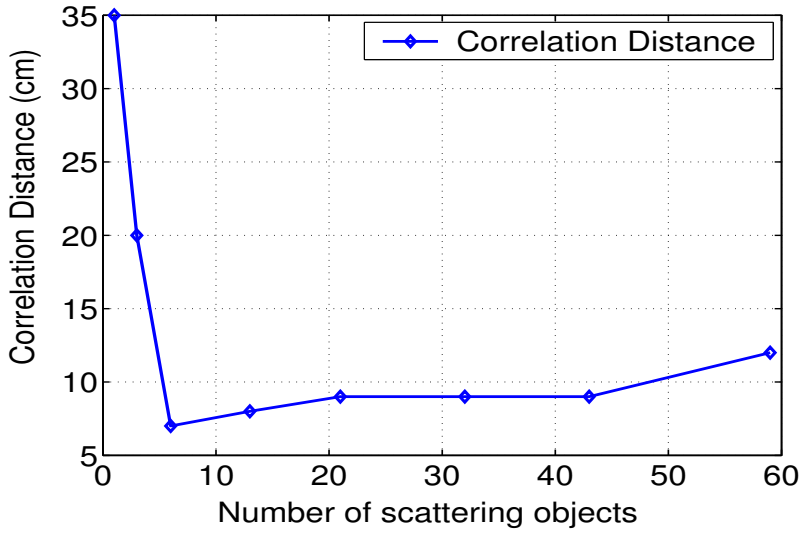


Figure 2.35: The correlation distance with different numbers of scattering objects in the medium.

antennas that should be used for optimum performance have been examined. Under our experimental conditions, we have observed that the correlation bandwidth of the medium saturates when there are about 20 scattering objects randomly distributed over an area of 1.44 $m^2$. The gain of time-reversal over change detection also saturated using the same number of scattering objects.

# Chapter 3

# Time-reversal focusing and nulling in frequency domain

## 3.1 Introduction

The increased demand for broadband communications has spurred extensive research on RF propagation. The objective is to understand the channel properties and make the best use of them to provide high-speed, reliable data communication. The RF propagation channel suffers from time-varying impairments like multipath, interference, and noise. These impairments have resulted in the development of various diversity schemes to overcome the potential problems of wireless communication. Time, frequency, space, and polarization diversities are some of the schemes that have been researched in the literature, and used extensively to provide various services. The main goal of diversity schemes is to create independent channels of propagation to transmit the message signal. Frequency diversity uses the fact that two frequencies, which are separated by more than one coherence bandwidth of the channel, fade independently. Similarly, time-diversity uses the fact that time instants which are separated by more than the coherence time of the channel fade independently [81]. In polarization diversity, different polarization modes can be used to send data through the channel as long as the fields from each polarization state

are independent from each other. Andrews et. al.[90] showed that the data transmission rate in a multipath environment could be increased by 6 times using the 6 components of the electromagnetic field. The implication is that all 6 components are uncorrelated from each other. In space diversity, multiple antennas are used so that if one of the antennas is in a deep fade, the other antennas can be used to provide and improve the communication link. Large spectral efficiencies are possible through multiple antennas based on the premise that a rich scattering environment creates independent transmission paths between each transmit antenna to each receive antenna. Based on Shannon's generalized capacity expression, it has been predicted that when using N transmitting and M receiving antennas, the information capacity of the channel can be $min\{M, N\}$ times higher than that available with a single transmitter and single receiver scheme in a rich scattering channel [2]. Thus multiple antennas and space-time coding schemes can convert the traditionally hostile multipaths into capacity-boosting elements.

Time-reversal methods use multiple antennas and the multipath components available in the medium to provide super-resolution focusing. The time-reversed waves propagate through the medium and focus around the initial source location from which they started. This is like creating a virtual cable between the antenna array and target antenna location. The waves move through the channel and reach the target antenna location at exactly the same time, producing sharp focusing both in space and time. This method can be used in two-way communications systems as well as radar, detection, and imaging algorithms. In [61] and [62], the authors have demonstrated electromagnetic time-reversal focusing using the phase-conjugation technique in the frequency domain. Their experiments have shown that by using a single-frequency phase-conjugation approach, they could focus energy around two targets which were separated by one-half wavelength. Following a similar experimental setup and a wide-band frequency spectrum, in this chapter we describe a multiple antenna time-reversal system that we can use to focus or null RF energy at certain points in space. Two sets of experiments are discussed in this chapter. In the first, we have implemented a completely physical time-reversal system using the

phase-conjugation technique in the frequency domain. The results show that RF waves propagate backwards through the stationary channel and focus around the initial source. This approach works when the channel response is reciprocal ($S_{21} = S_{12}$) and the channel remains stationary during the process. In the second set of experiments, we measured the channel response using a network analyzer and studied the characteristics of the time-reversal system using a computer. When we compare physical time-reversal with back-propagation on a computer, we experimentally verified that the focusing signal spectrum is exactly the same as the one that we could obtain on a computer using the forward channel measurement information. The frequency domain experiments have shown that by using the time-reversal technique with multiple antennas, we can maximize (focus) as well as minimize (null) RF energy at active or passive target points in the medium. We have performed experiments between 4 and 6 GHz in a complex laboratory environment [70]. The degree of nulling as well as focusing depends on the multipath components in the channel and the bandwidth of the waveform. By using a 2-D grid, we have shown the impact of the number of antennas and bandwidth on RF focusing on active targets. By using the degrees of freedom available from either the frequency bandwidth or the multipath components in the medium, it has been demonstrated that RF waves can focus or null at multiple targets simultaneously. The experimental results have shown that it is possible to have sharp nulling by using a zero-forcing time-reversal waveform. The noise is always an important part of system design. By using experimental data and computer generated noise, we have demonstrated that time-reversal focusing is very robust against noise. The back-propagated time-reversal waveform might be different than the forward propagation waveform, but still we can achieve spatial and temporal focusing using the time-reversal methods.

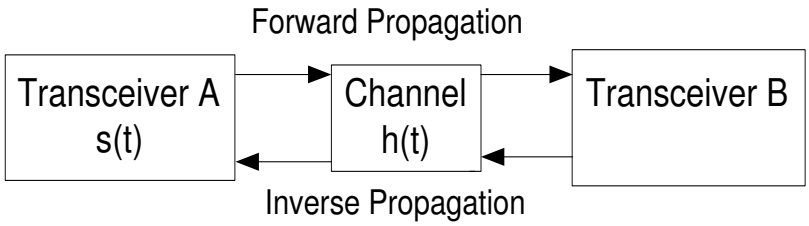


Figure 3.1: The general time-reversal signal flow graph.

## 3.2 Analysis of time-reversal focusing and nulling

In time reversal, the antenna array acts as a mirror that refocuses the time-reversed signals back onto the source, owing to the time-reversal symmetry of Maxwell's equations. The general time-reversal signal flow graph is shown in Fig. 3.1. First a pulse s(t) is sent from the transceiver A, the received pulse at B is given by $s(t) * h(t)$. The time-reversed waveform $s(T-t) * h(T-t)$ is sent back from B. The signal received at A is now $s(T-t) * h(T-t) * h(t)$. As pointed out in Chapter 2, the last two-terms in the equation can also be thought of as the autocorrelation of the channel impulse response. The more multipaths we have, the more random the channel becomes and the autocorrelation response has a sharp center-lobe. That sharpness defines the degree of focusing and it distinguishes the target position from neighboring points. The multipath components thus enhance the superresolution capability of the system. In the case of focusing, all the multipath components constructively add up at the receive position. In the frequency domain, time-reversal is equivalent to phase conjugation. The channel magnitude response (FFT of $h(t)$) can be described by

$$H(f) = A(f)e^{j\phi(f)}, \tag{3.1}$$

where A(f) is the amplitude response and $\phi(f)$ is the phase response across the frequency band. We can write the focused signal from multiple antennas as follows

$$Y_{focus}(f) = \sum_{i=1}^{M} k_i \cdot S_i(f)^* \cdot A_i(f) e^{-j\phi_i(f)} A_i(f) e^{j\phi_i(f)} \tag{3.2}$$

$$Y_{focus}(f) = \sum_{i=1}^{M} k_i \cdot S_i(f)^* \cdot |A_i(f)|^2 \tag{3.3}$$

where $S_i(f)$ is the frequency response of initial probing pulse ($s(t)$), $k_i$ is a normalization constant during the retransmission of time-reversed waveforms and $M$ is the number of antennas in the array. The signals from multiple antennas constructively add and result in a focusing signal.

In the multiple antenna system, by modifying the time-reversed signal, we can have a nulling instead of focusing around the initial source. By inverting the polarity of time-reversed signals for every other antenna before retransmission, we can null out the source. That is, signals from even numbered antennas will add coherently, signals from odd numbered antennas will add coherently but the combination of the odd and even antenna signals will be 180 degrees out of phase, resulting in minimal signal strength at the original source point.

$$Y_{nulling}(f) = \sum_{i=1}^{M} k_i \cdot S_i(f)^* (-1)^i \cdot A_i(f) e^{-j\phi_i(f)} A_i(f) e^{j\phi_i(f)} \tag{3.4}$$

$$Y_{nulling}(f) = \sum_{i=1}^{M} k_i \cdot S_i(f)^* (-1)^i \cdot |A_i(f)|^2 \tag{3.5}$$

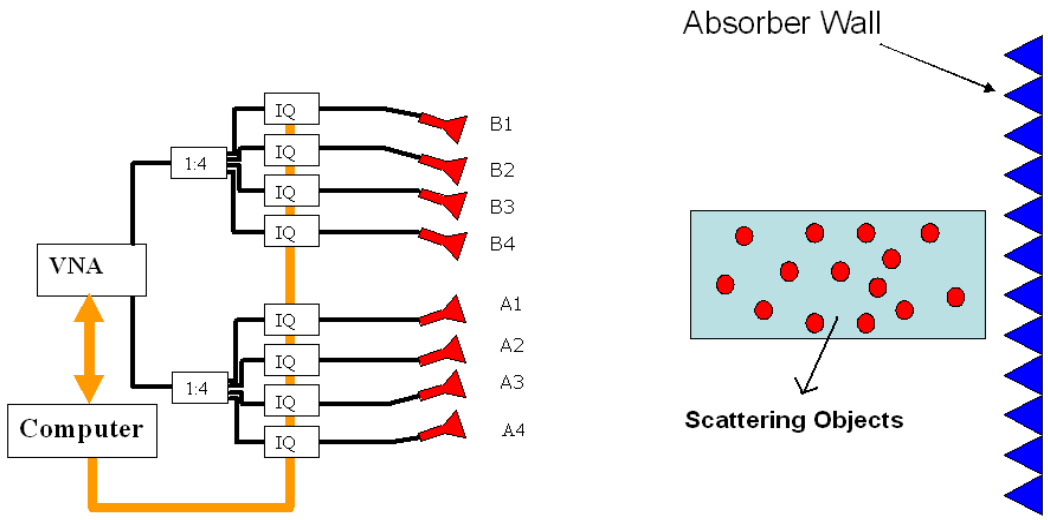


Figure 3.2: Physical time-reversal experimental setup.

## 3.3 Experiments and Results

### 3.3.1 Wide-band Physical Time-Reversal System Implementation

The frequency-domain time reversal system constructed for the experiments is shown in Fig. 3.2 and Fig. 3.3. The system is designed to take advantage of I-Q modulators as amplitude and phase shifters that can operate between 2-6 GHz.

The I-Q modulators multiply an RF signal by a complex exponential, $Ae^{j\theta}$. The attenuation ($20log_{10}(A)$) through the I-Q modulators is programmable between 0 and 70 dB with an accuracy of 0.2 dB. The phase shift $\theta$ can be between 0 and 360 degrees with an accuracy of 5 degrees. Separate transmit and receive arrays were constructed using horn antennas that operate between 4 and 6 GHz. The arrays have 4 antennas each, with elements spaced by 25 cm ($\sim$ 4 wavelengths). In this set-up, a vector network analyzer is used to measure the transmission response between the horn antennas pointed at the region to be probed. The frequency range to be probed is 4-5.5 GHz, equivalent to transmitting a pulse with a duration of about 0.67 ns. Operation of the system is as follows. An initial probing signal is transmitted from the array A (transmitting array). In this case, all of the I-Q modulators in array A are set to zero attenuation and phase, while all but one of the


Figure 3.3: Photos of the physical time-reversal experimental system. a) View of the A and B antenna arrays b) Rear view of the antenna arrays also showing copper pipes as scattering objects with the absorber wall in the background.

I-Q modulators in array B (the receiving array) is set to highest attenuation, effectively turning off all but one receive element ($B_1$). The frequency is then stepped between 4 and 5.5 GHz, measuring the amplitude and phase at the receive element for each frequency. This process is then repeated for each element in the receive array. The complex responses measured at each element are then conjugated and these values are used to set the I-Q modulators in array B on transmit back. To realize time-reversal, array B is used as the transmit array. At each frequency, the I-Q modulators are set to the conjugate values from the previous measurement and re-transmitted to the channel simultaneously. The time-reversal signals propagate through the paths that they undertake in the forward direction and focus around the initial source. The outputs of the antennas in the A array are then summed with a power combiner. After repeating this process for each one of the frequency points, the time-response is obtained by taking the IFFT of the frequency domain signal. Fig. 3.4 shows the frequency spectrum and time-response of the focusing signal. Fig. 3.4a compares the physical time-reversal focusing spectrum and estimated focusing spectrum

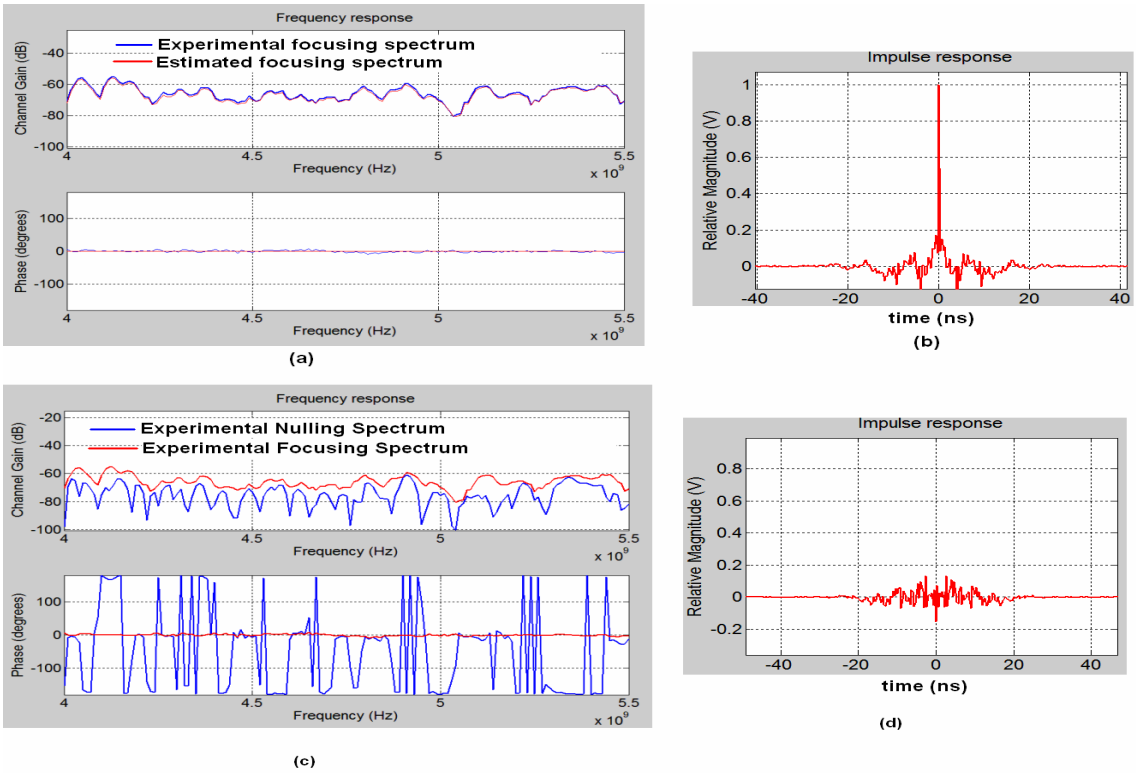


Figure 3.4: a) Frequency response of physical time-reversal focusing signal b) Time-response of focusing signal c) Frequency response of physical time-reversal nulling signal d) Time-response of nulling signal

using the forward channel information only. The close match between the two curves verifies that reciprocity holds in the medium and we can do back-propagation on the computer and still obtain a very similar frequency spectrum as to the one obtained through physical back-propagation. Fig. 3.4b is the impulse response of the physical time-reversal focusing signal. By changing the polarity of the time-reversal waveforms before re-transmission from antenna array B, we can have nulling instead of focusing at the initial source position. Fig. 3.4c shows the frequency response and Fig. 3.4d shows the time-response of the nulling waveform where the polarity of even-numbered antennas on the B-array has been changed before retransmission. In the case of focusing, backward and forward waves match perfectly resulting in cancellation of phase across the whole band (Fig. 3.4a). That is why in the time-response the dispersive components in the forward channel disappear and compress in time. As for the nulling case, the forward and backward propagating

waves again lead to cancellation of phase for each antenna, but the sum signal can be positive or negative. If the sum signal is positive, then the phase is 0 degrees, if it is negative the phase is 180 degrees. That is why the phase is alternating in the phase response of nulling signal (Fig. 3.4c).

### 3.3.2 Time-reversal focusing and nulling in an indoor environment

The time-reversal experiments were done in a multipath-rich laboratory environment (see Fig. 3.5). A six element antenna array consisting of 2 dBi omni-directional discone antennas [91] were used to focus and null the target spot using the time-reversal method *. Another discone was used as a target antenna and moved on a 10 by 10 grid (see Fig. 3.6 and Fig. 3.7). This 2-D grid was scanned with increments of 5 cm and 1 cm that corresponds to an area of 50 cm x 50 cm and 10 cm x 10 cm respectively. A vector network analyzer was used to measure the complex channel responses between the target antenna and each element of antenna array using a frequency band of 2 GHz between 4 and 6 GHz. In the experiments, we used 201 frequency points resulting in a frequency resolution of 10 MHz. The measurement was repeated for every point on the grid (100 measurements). So for each frequency point, we have a 6x100 matrix that has the complex channel response between each element in the antenna array and the target antenna on each one of 100 points on the grid.

Time-reversal methods work to provide super-resolution in rich-scattering environments. The autocorrelation response describes the amount of dispersion in the channel. Fig. 3.8a shows the channel magnitude response between the first element of the antenna array and the target antenna that is at the center of the grid. Fig. 3.8b is its autocorrelation response. The 50% coherence bandwidth of the channel is approximately 8 MHz. The delay spread is inversely proportional to the coherence bandwidth. In this case, the root mean square (RMS) delay spread is about 30 ns.

*The array was actually synthesized by moving a single antenna to 6 different positions and combining the measurements on a computer.

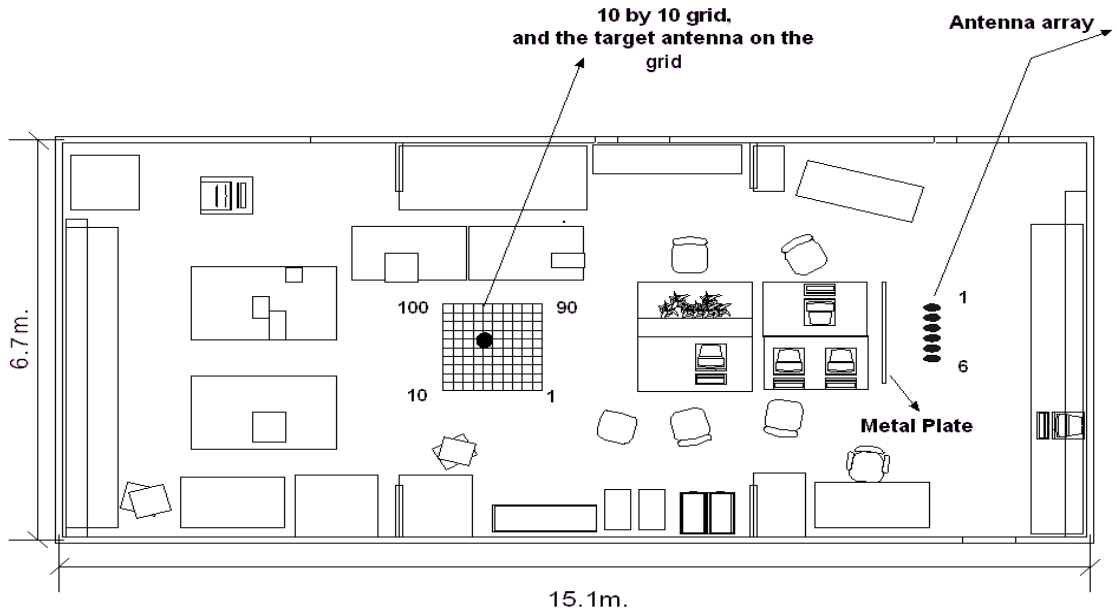


Figure 3.5: Cluttered laboratory layout where the experiments were conducted to focus (null) RF energy on the target antenna location which is placed on the 2-D grid on the left. The lab is a multi-path rich channel with many metal objects around. (Modified from [61])

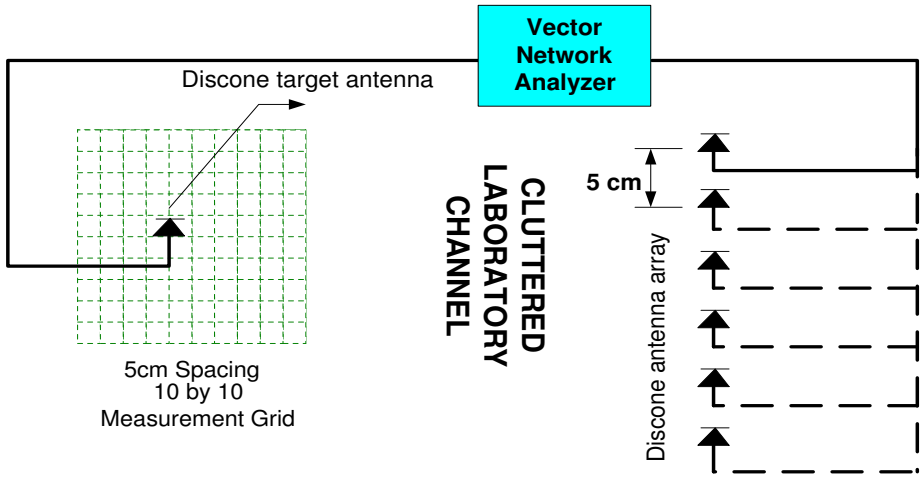


Figure 3.6: Signal mapping in range and cross range directions. Both directions were scanned by 5 cm increments and 1 cm increments.

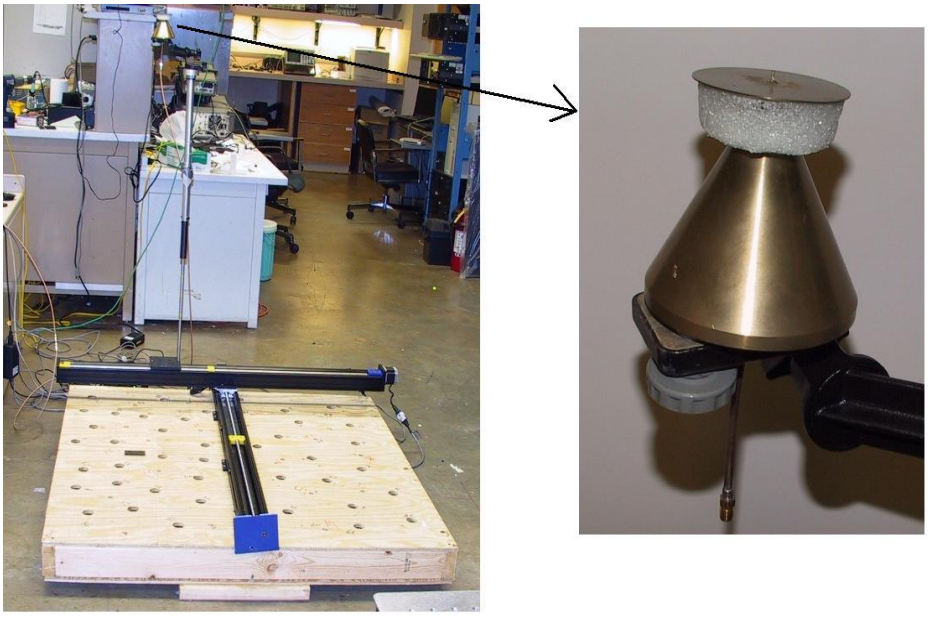

Figure 3.7: The experimental setup. Two computer controlled linear stages were used to measure the complex channel response on the 100-point grid.

By using the analysis described through Equations 3.1- 3.5, we have shown the focusing and nulling signals using the experimental data. Fig. 3.9 shows the focusing and nulling frequency spectrum and impulse response between the center point of the 2-D grid and the antenna array. First a probing pulse is sent from the mid-point on the grid (pixel 45 on the grid as shown in Fig. 3.5). Each antenna on the antenna array captures the received waveforms, phase-conjugates them and sends them back. The waves propagate backward through the same paths to the antenna array and focus around the starting point. Note that we have experimental results from the target antenna to the antenna array. The back-propagation is done on a computer. The frequency domain signals suggest that the focusing signal is, on the average, 10 dB stronger than the nulling signal. In the time-domain, the focusing signal has a sharp peak at the mid-point and some small side-lobes. The multipath components all reach the target antenna and cause constructive interference at the focusing spot. It is a compressed version of the delay-spread profile, with the center half-power pulse-width 0.5 ns, which is the resolution that could be obtained by using a 2 GHz wide signal. The nulling signal amplitude is smaller than even the side-lobe level of

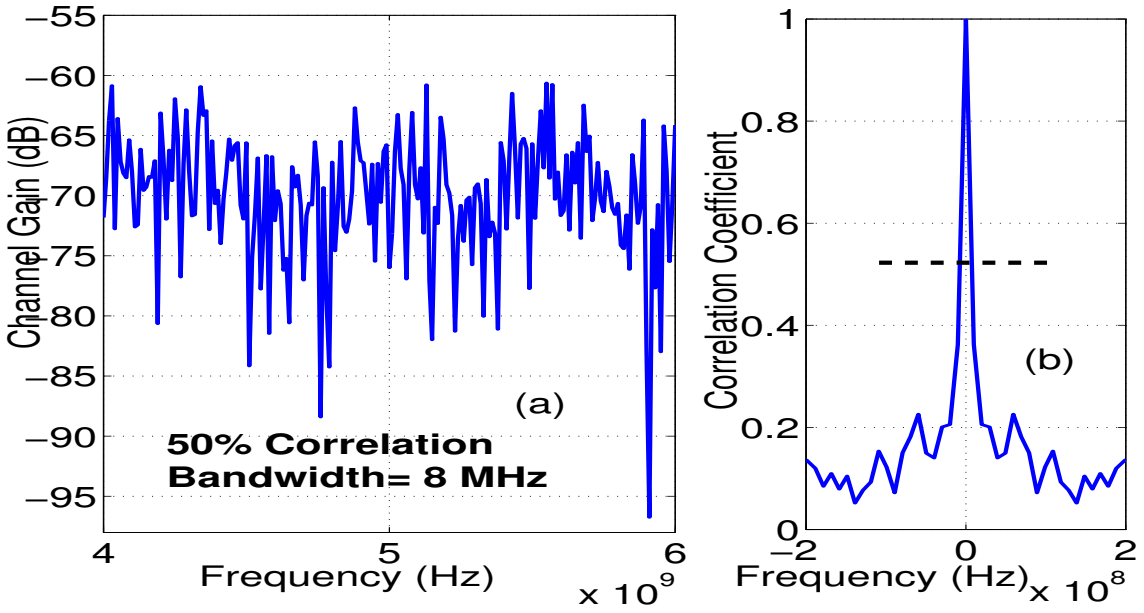


Figure 3.8: (a) Channel frequency response, (b) Auto-correlation response of the channel between the first element of antenna array and the center spot of the 2-D grid.

the focusing waveform. It has a slightly smaller value at the time when focusing occurs. Fig. 3.10 shows the spatial focusing and nulling signal power on the 10 by 10 grid. The fact that we have been using 2 GHz bandwidth and operating in a multipath rich environment resulted in a sharp focused spot on the grid. The peak-to-spatial side-lobe ratio of the focusing waveform on Fig. 3.10a is about 4.5 dB, and the half-power area of the focused spot is approximately 4 cm by 9 cm in the cross-range and range directions respectively. As for the nulling, the alternate sign change before retransmission of the RF signals caused destructive interference all along the grid locations and caused minimal signal strength on the grid points. The nulling energy at the target antenna location is slightly less than the surrounding area. The nulling power (across 2 GHz band) is 10 dB weaker than the focusing power at the same spot.

#### 3.3.2.1 Time-reversal focusing with multiple antennas and multiple frequency points

Time-reversal methods utilize the independent information available through multiple antennas as well as multiple frequency points. The number of multipath components also

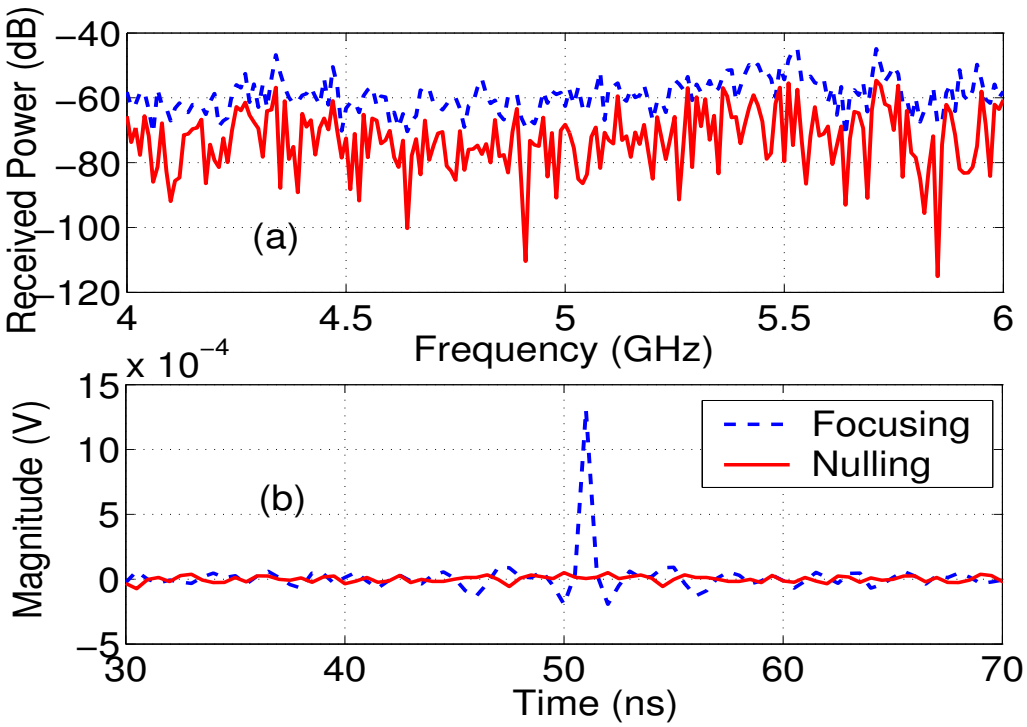


Figure 3.9: (a) The frequency response and (b) impulse response of focusing and nulling waveforms between the antenna array and the mid-point of the 2-D grid.

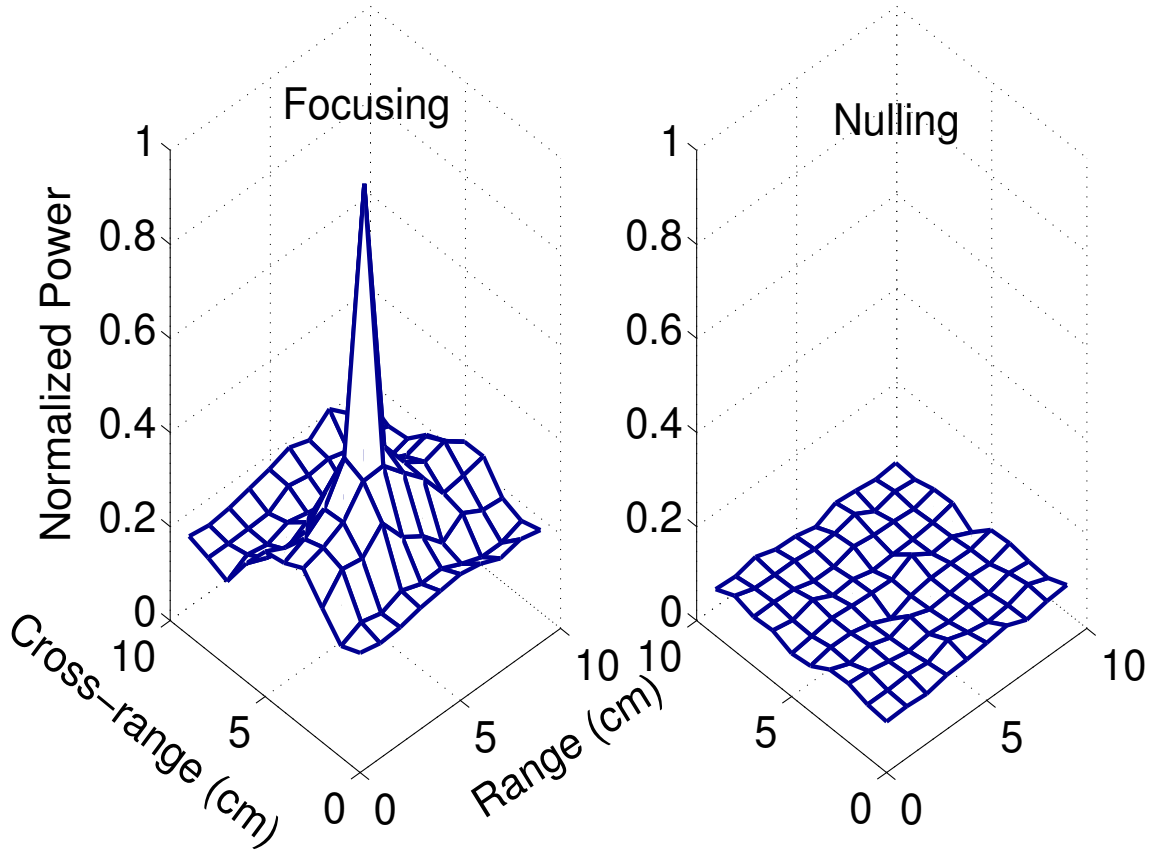


Figure 3.10: 3-D plot of spatial focusing and nulling signal power around the mid-point of the grid.

affect the quality of spatial and temporal focusing, improving the peak-to-sidelobe ratio both in space or time. In our experimental setup, the multipath dispersion is fixed since we are operating in a stationary channel (i.e., no objects move inside the lab environment). Thus the degrees of freedom can be obtained through the number of antennas in the array as well as the bandwidth. The more antennas we use, or the larger the bandwidth we operate on, the sharper the focused signal obtained using the time-reversal method. Fig. 3.11 shows the focused power across the 2-D grid for different numbers of antennas and frequency points. In the case of a single antenna and single frequency point, there is almost no focusing present on the target antenna location which has been marked with $'+'$ sign (Fig. 3.11a). As we increase the number of antennas and still use a single frequency as plotted on the left column, the focused spot becomes more visible. By using 2 antennas, it seems that we get a focused spot that is about 5 cm off from the target antenna location. 4 antennas and 6 antennas caused focusing at the correct location with varying degrees of range and cross-range resolutions. Using multiple antennas as well as multiple frequency points results in a sharper focusing spot. On Fig. 3.11h, we have used 6 antennas and 201 frequency points and obtained a sharp focusing signal at the target location. The resolution is related to the degree of multipath components as well as the bandwidth of the channel. Using all 6 antennas on the antenna array, Fig. 3.12 shows the range and cross-range resolution of the target as a function of bandwidth. If a single frequency point is used, the range resolution (depth of focus) is 25 cm, and cross-range resolution is 15 cm. For comparison, the Rayleigh criterion for range-resolution is

$$\lambda \cdot (\frac{L}{a_e})^2 = 0.06 * (\frac{6}{0.25})^2 = 35m. \tag{3.6}$$

Similarly the cross-range resolution based on the Rayleigh criterion is

$$\lambda \cdot (\frac{L}{a_e}) = 0.06 * (\frac{6}{0.25}) = 1.44m. \tag{3.7}$$

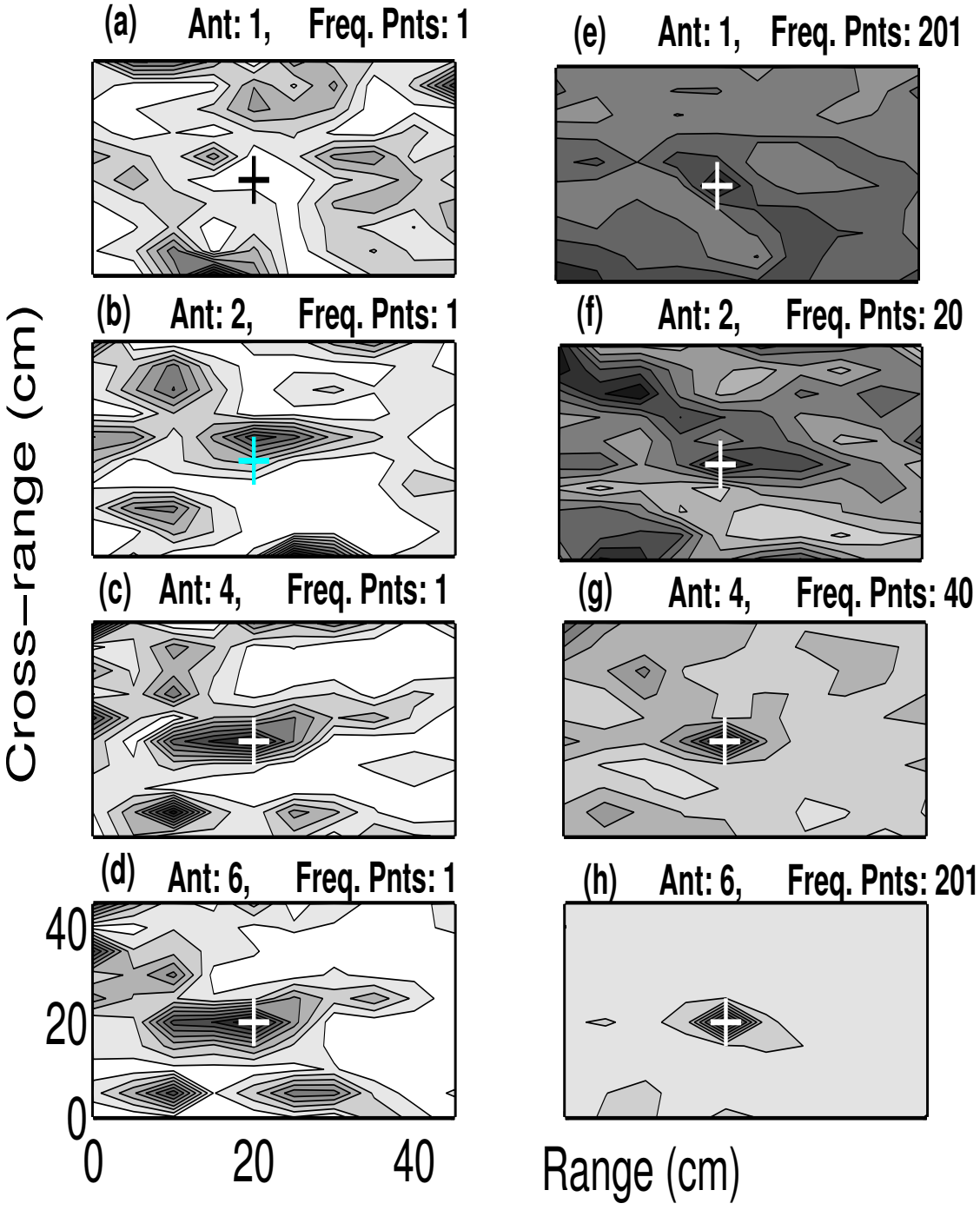


Figure 3.11: The focusing quality as a function of number of antennas and number of frequency points used.

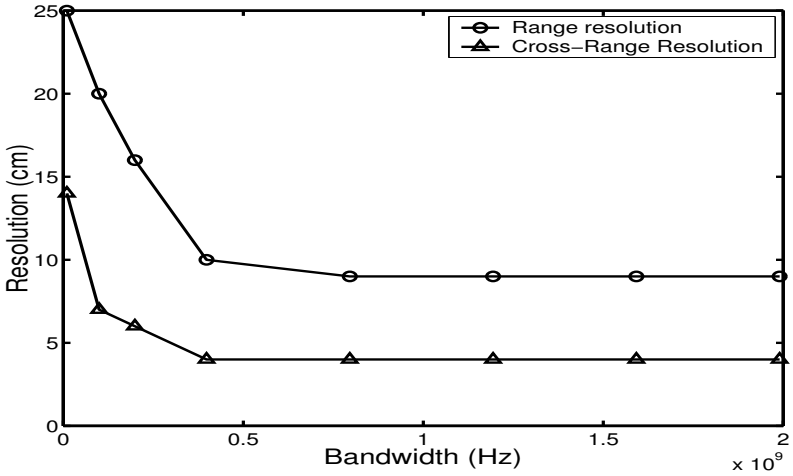


Figure 3.12: Range and cross-range resolution as a function of bandwidth. Six antennas were used on the transmit array.

Even a single frequency point along with time-reversal back-propagation produced a much tighter focused spot compared to the Rayleigh resolution limits. As we increase the bandwidth, the focused spot becomes tighter. By using a 2 GHz bandwidth signal, the cross-range resolution becomes 4 cm and the range resolution 9 cm. This is a significant improvement over the Rayleigh limit, hence the term super-resolution.

#### 3.3.2.2 Time-reversal focusing and nulling more than one target antenna location

By using time-reversal methods, we can have focusing as well as nulling for more than one point. To achieve this, each target antenna should send their beacon signal to the antenna array. The antenna array receives all the echos from the target antennas, and sends the time-reversed version of the received signal back to the channel. Note that the received signal is the sum of forward propagation waves from each target location that can be described as follows

$$y_k(t) = \sum_{j=1}^{P} s(t) * h_{jk}(t) \tag{3.8}$$

where $s(t)$ is the initial beacon signal and $h_{jk}(t)$ is the channel impulse response between $j^{th}$ target antenna and $k^{th}$ antenna on the antenna array and P is the number of target antennas that send beacon signals to the antenna array. The time-reversed sum signal propagates back through the complex channel environment and focuses around the target positions at the same time. This is simultaneous transmission and simultaneous focusing and nulling on the target sites. The time-reversed waveform at the $k^{th}$ antenna on the array is given as follows

$$r_k(t) = y_k(T-t) = \sum_{j=1}^{P} s(T-t) * h_{jk}(T-t) \tag{3.9}$$

A delay T is introduced to make the system causal. T is long enough such that all the echoes reach the antenna array. The focusing happens at time $t = T$ at the same time at all target antenna locations. The focused signal at the $p^{th}$ site is given by

$$z_p(t) = \sum_{k=1}^{M} s(T-t) * h_{pk}(T-t) * h_{pk}(t) + \tag{3.10}$$

$$\sum_{k=1}^{M} \sum_{j=1, j\neq p}^{P} s(T-t) * h_{jk}(T-t) * h_{jk}(t) \tag{3.11}$$

where M is the number of antennas in the antenna array. The first term contributes to the focusing power while the second term behaves like interference. Fig. 3.13 shows time-reversal focusing and nulling using 2 GHz bandwidth in the laboratory environment. Fig. 3.13a shows that using 6 antennas, we can focus RF energy on 7 spots simultaneously. Fig. 3.13b shows nulling those 7 spots using a modified time-reversal waveform (namely changing the polarity of every other antenna). In Fig. 3.13b, the time-reversed signals from consecutive antennas cancel each other and result in minimal RF energy around the target positions. The reason why perfect cancellation on the target spots does not occur is that the channel magnitude is not exactly the same between consecutive antenna pairs to the target antenna. It thus results in minimizing the RF power level throughout the region.

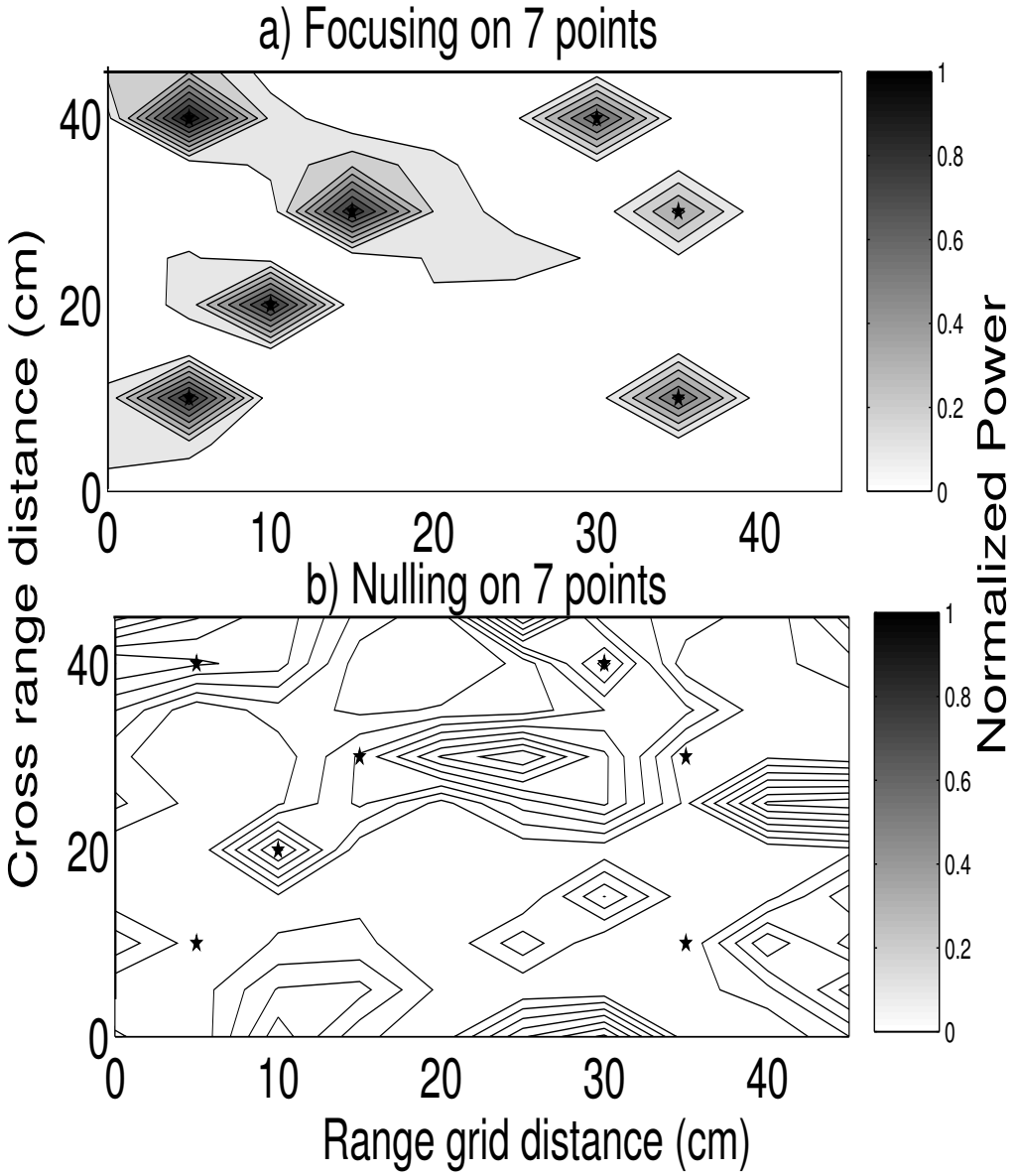


Figure 3.13: a) Time-reversal focusing on 7 spots on the 10 by 10 grid. b) Time-reversal nulling on the same spots.

#### 3.3.2.3 Time-reversal nulling using zero-forcing back-propagation signal

It is also possible to produce very sharp nulling around the target position. One can use a zero-forcing equalizer on the transmitter instead of receiver and send such a modified time-reversal waveform back to the channel. By multiplying the time-reversed signal with appropriate coefficients and changing the polarity for every other antenna, we can get very sharp nulling just around the target antenna.

The mathematical equations are described below. The time-reversed waveform is adjusted so that it is the inverse of the forward channel. The back-propagated waveform from $i^{th}$ antenna is given as

$$r_i(f) = \frac{k}{A_i(f)e^{j\phi_i(f)}} \tag{3.12}$$

where k is a normalization constant. The time-reversed waveforms are sent back with alternating polarities as before:

$$Y_{nulling}(f) = \sum_{i=1}^{M} k \cdot S_i(f)^* \frac{(-1)^i \cdot A_i(f)e^{j\phi_i(f)}}{A_i(f)e^{j\phi_i(f)}} \tag{3.13}$$

$$Y_{nulling}(f) = \sum_{i=1}^{M} k \cdot S_i(f)^* (-1)^i \tag{3.14}$$

Fig. 3.14 shows the experimental results in which we have used the time-reversal method to achieve sharp focusing around the target antenna and the zero-forcing equalizer type of time-reversal waveforms to produce sharp nulling around the target antenna. The single target antenna coherently receives all the echoes from the environment and has the maximum signal strength compared to its surroundings. In the case of nulling, the back-propagated signals have equal magnitude but alternating phase at the target antenna location and cause a sharp null.

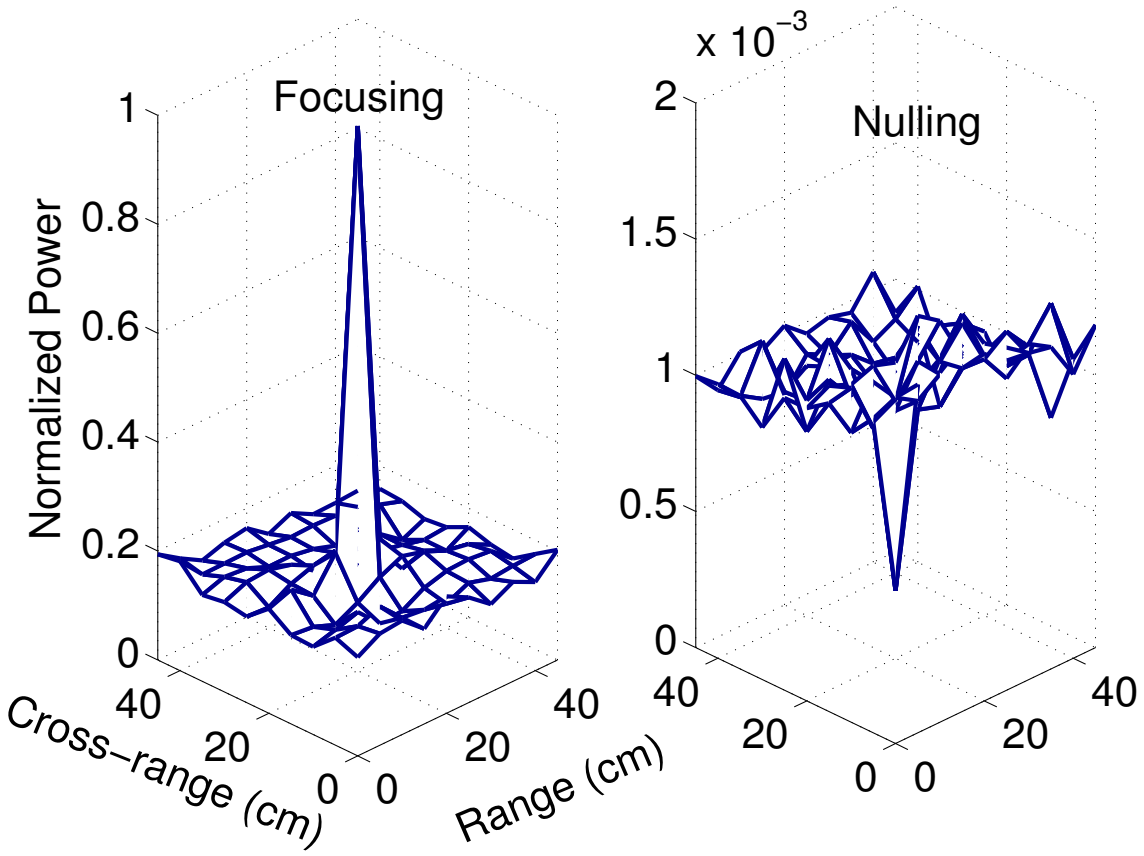


Figure 3.14: a) Time-reversal focusing on a single target. b) Time-reversal nulling using zero-forcing algorithm.

#### 3.3.2.4 Time-reversal performance in the presence of noise

The forward channel and back-propagation channels should be the same for the ideal performance from a time-reversal system. But in reality, there is noise present in the system. The performance of time-reversal focusing should be studied in the presence of noise. In this section, we study the performance of time-reversal focusing in the presence of complex Gaussian noise. If the time-reversed signal contains noise, the received signal at the focused spot from the $i^{th}$ array element is

$$Y_{focusing_i}(f) = k[S(f)H_i(f) + N_i(f)]^* H_i(f) \tag{3.15}$$

where f spans the whole frequency band, and k is a normalization constant for the retransmission waveform $[S(f)H_i(f) + N_i(f)]^*$. The above expression can be decomposed into two terms: the time-reversal focusing term and a noisy signal term.

$$Y_{focusing_i}(f) = kS^*(f) \cdot H_i(f)^* H_i(f) + k \cdot N_i(f)^* H_i(f) \tag{3.16}$$

The signal-to-Noise ratio (SNR) is the ratio of signal power (the magnitude square of the first term) to noise power (the magnitude square of the second term):

$$SNR = \frac{\sum_{i=1}^{M} |S^*(f)H_i(f)^* H_i(f)|^2}{\sum_{i=1}^{M} |N_i(f)^* H_i(f)|^2} \tag{3.17}$$

The performance of the time-reversal system in the presence of noise is shown in Fig. 3.15. We have 4 cases with various levels of noise present in the back-propagated waveform. If the noise is small compared to the ideal-back propagated waveform, the focusing spot will not be affected. This is shown in Fig. 3.15a with an SNR of 4 dB. As we reduce the SNR, the noise starts affecting the back-propagated waveform and results in losing the coherence at the original target location. Even with an SNR of 0 dB and -4 dB, the focusing spot is still visible (Fig. 3.15b and Fig. 3.15c). If the SNR becomes too low, then the focusing spot completely disappears as shown with -11 dB of SNR on Fig. 3.15d. The spectra of the ideal

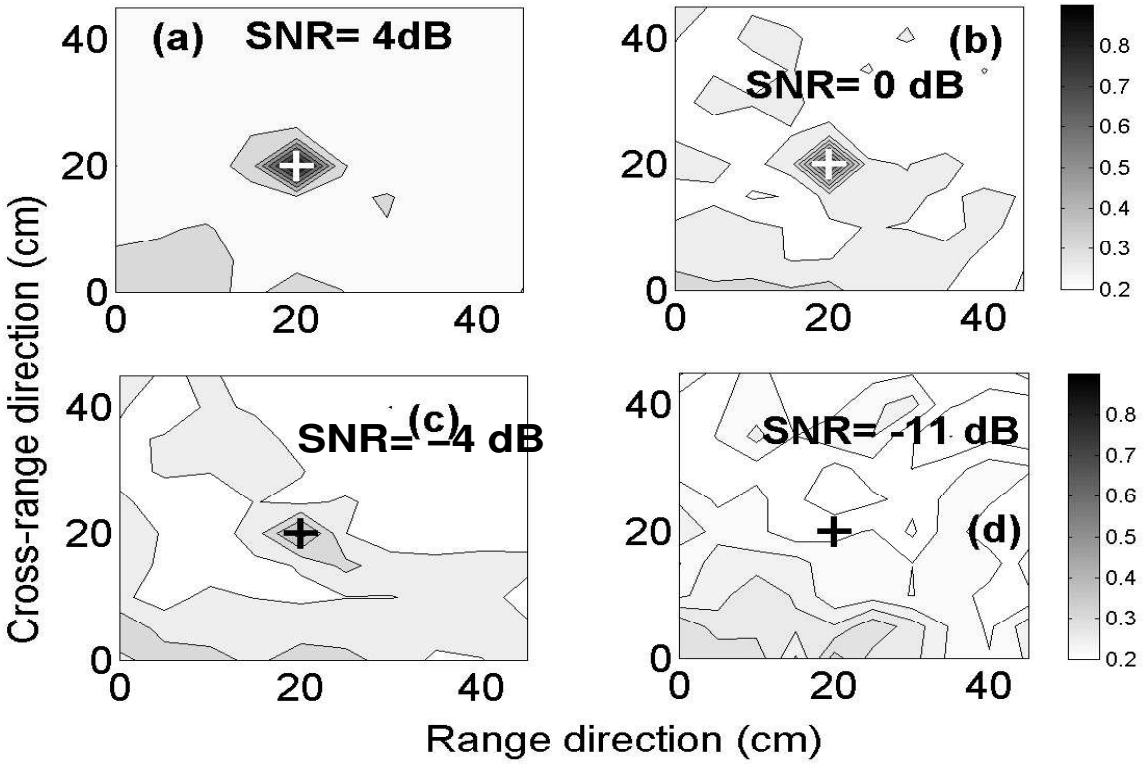


Figure 3.15: The time-reversal waveform is back-propagated in the presence of various amount of noise.

back-propagated waveform and the noisy back-propagated waveform with an SNR of -4 dB is shown in Fig. 3.16. Even though the two spectra show significant differences, the time-reversal procedure can focus RF energy at the target location. This shows that time-reversal is robust against noise that may be present in the system, such as receive circuit noise or finite resolution of the analog-to-digital converter at the receiver.

## 3.4 Conclusions

We have described multiple antenna microwave focusing and nulling experiments that make use of time-reversal concepts. The experiments were done using a bandwidth of 2 GHz at the center frequency of 5 GHz in a laboratory environment. We have experimentally shown microwave nulling as well as focusing results in a 2-D plane. We analyzed the performance of time-reversal focusing using different numbers of antennas and frequency

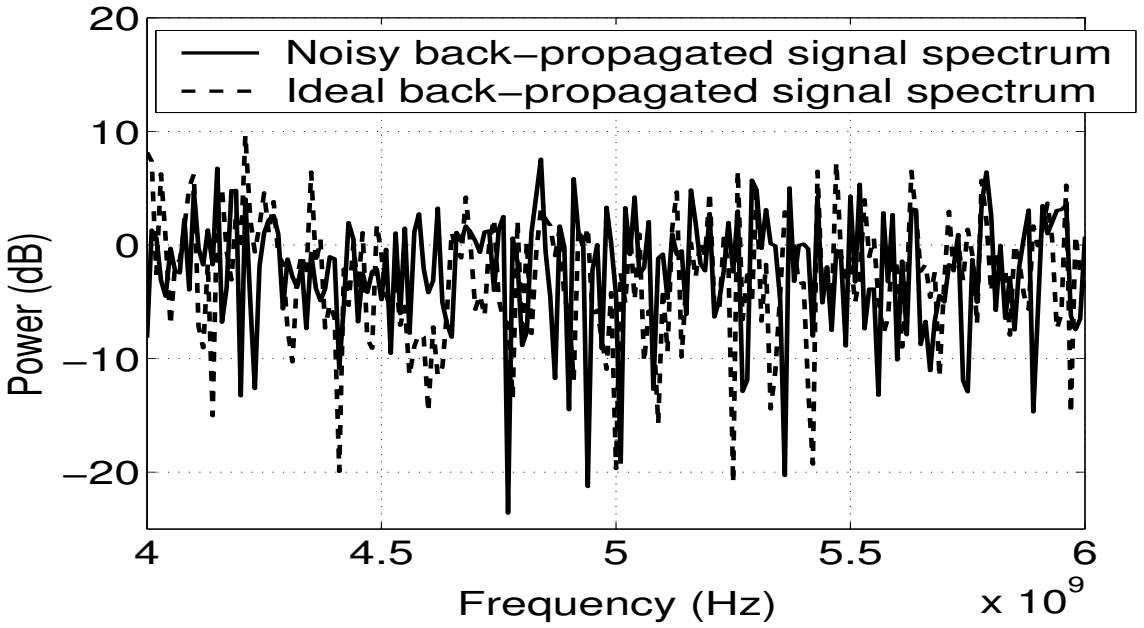


Figure 3.16: The ideal and noisy time-reversal signal spectra transmitted back from the fourth antenna on the array.

points. We have demonstrated that we can, simultaneously, focus or null RF energy at more than one spot. In fact, it has been shown that RF energy can focus around 7 spots using only 6 antennas on the time-reversal array. The nulling algorithm deployed resulted in minimizing the RF energy around the target neighborhood rather than just the target locations. The zero-forcing time-reversal method resulted in very sharp nulling at the target antenna location. We have also studied the performance of time-reversal methods in noisy environments. The results have shown that time-reversal techniques are robust against noise that may be present in the system. The ideas presented in this chapter can be used for wireless communications, high-resolution microwave imaging systems, and detection algorithms. In the time-reversal nulling technique, for example, electromagnetic waves can be made to destructively interfere on the objects and the medium becomes virtually transparent. When the target appears in the medium, it will be easier to detect it. The nulling schemes can also be used in conventional communication systems in which the base station wants to null a specific user in the cell. The resolution achieved by this method can

be orders of magnitude smaller than that achieved by using conventional beam-steering techniques.

# Chapter 4

# Single Antenna Microwave Focusing and Nulling using Time-Reversal Techniques

## 4.1 Introduction

Time-reversal methods work to provide super-resolution focusing in a rich multipath environment. Time-reversal systems are generally implemented using multiple elements on the antenna array. The reason for this is to utilize the degrees of freedom available through space. Given that the multipath components are sufficiently rich in the medium, it is possible to observe time-reversal focusing using a single antenna. In this chapter, we describe a single antenna microwave focusing and nulling technique that makes use of time-reversal concepts. The time-domain experiments have shown that by using a single antenna and time-reversal techniques, we can have focusing as well as nulling at any point in space. We have done experiments at 2.45 GHz in a metal cylindrical duct channel that was terminated with metal caps on either side. This cavity environment provided with rich multipath components. The degree of focusing or nulling depends on the multipath components in the channel as well as the bandwidth of the signal. The cavity provides a

multipath rich-environment where we can show focusing and nulling by using a relatively small bandwidth compared to that required by an open laboratory experiment.

In [63], the authors presented a single antenna time-reversal focusing experiment at microwave frequencies. They used a 1 MHz wide pulse to show the focusing effect in a reverberant cavity. By following similar steps and using a wider bandwidth (3-dB pass-band bandwidth of 36 MHz), in this chapter we will show experimental results of single antenna focusing and nulling at 2.45 GHz. The physical properties of the duct channel will be briefly described since the medium determines the quality of time-reversal energy focusing. By using a simple propagation model developed for a duct channel [93], some important characteristics of the time-reversal method will be described. In a single antenna system, the bandwidth of the transmit pulse and reflections in the medium are two main parameters that affect the time-reversal system performance. The impact of these physical parameters will be analyzed using simulation. After discussing the time-reversal performance inside a duct channel, experiments will be described that show time-reversal spatial and temporal focusing and nulling using a single antenna.

## 4.2 Characteristics of Waveguide Channel

The duct channel that we used in the experiment was a 9.14 m long and 0.3 m diameter waveguide with metal caps on either side. The duct behaves as an overmoded waveguide when driven at RF frequencies. A generic duct channel is shown in Fig. 4.1. Coaxially fed monopole transmitting and receiving antennas are used to couple into and out of the duct cavity. The channel between the two antennas is strongly affected by the duct channel structure, operating frequency, and propagating modes in the duct. At the transmitter side, RF signals are fed to an antenna that excites waveguide modes in the duct. The number of TE (transverse electric) and TM (transverse magnetic) modes excited in the duct depends on the antenna structure, geometry, and dimensions of the duct. For example, the cylindrical duct that we used in the experiments has 17 propagating modes in the

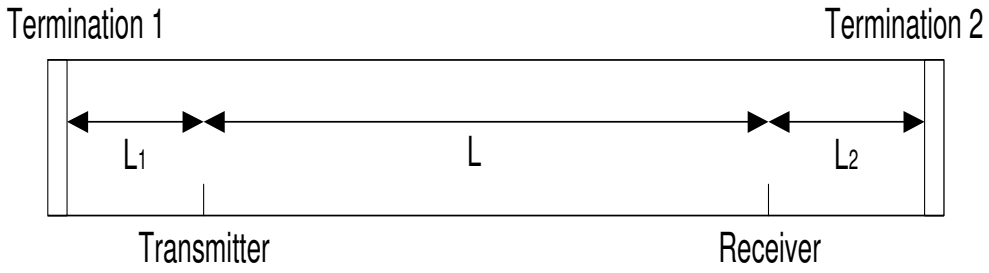


Figure 4.1: A simple duct channel.

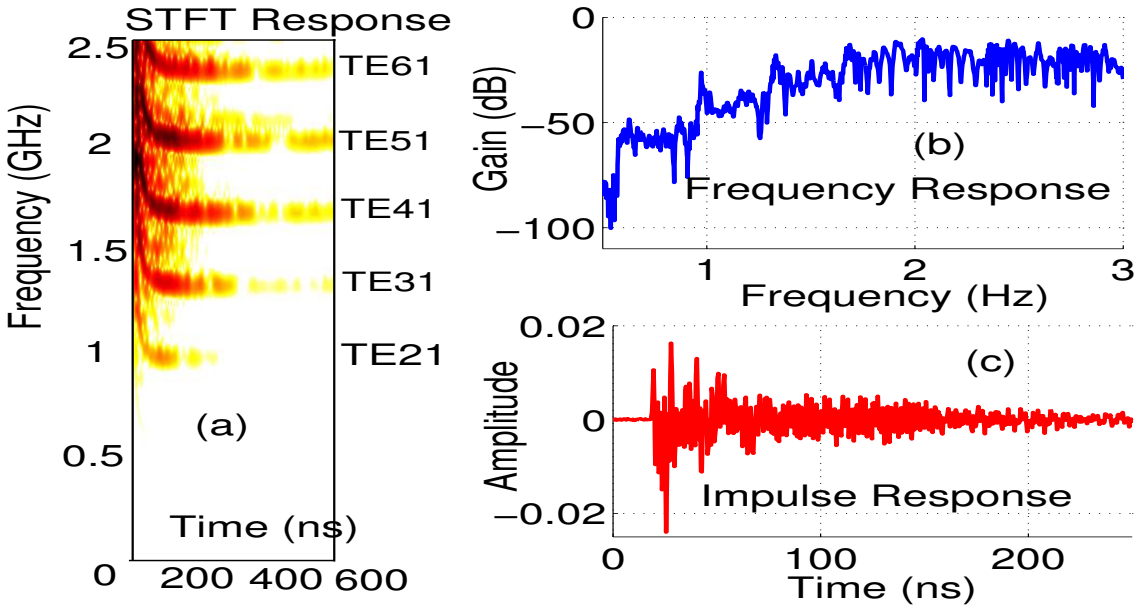


Figure 4.2: (a)Short-time fourier transform (STFT), (b) frequency response, (c) impulse response of the waveguide channel. The modes produce dispersion inside the duct.

2.4-2.5 GHz range. Each mode has different frequency characteristics. One can think of the mode transfer function as a high-pass filter. The cut-off frequency depends on the dimensions of the waveguide. The excited modes propagate through the duct system with different group velocities and attenuation constants, reflecting from terminations and non-uniformities along the path, and are captured by the receiving antenna. Fig. 4.2a shows the temporal-frequency response, Fig. 4.2b the frequency response, and Fig. 4.2c the impulse response of a 5.2 m long duct channel that has open ends on both sides. The antenna used in the experiment was a quarter wavelength monopole probe antenna tuned at 2.45

GHz. The temporal-frequency response is obtained by using short-time Fourier transform. It shows the frequency content of the waveform inside the duct at various time-intervals. For the 0.3 m diameter duct channel, the first cut-off frequency is 570 MHz (the transition region from no propagation to the first mode propagation can be observed on Fig. 4.2b). Below the first cut-off frequency, there is no wave propagation [94]. For a given operating frequency band, there may exist different numbers of propagating modes carrying the energy inside the duct. In our simulations and experiments, monopole probe antennas were used that excited 5 dominant modes inside the duct (five dominant paths in the time-frequency plot of Fig. 4.2a). The fact that each mode propagates with a different velocity results in inter-modal dispersion. Based on the frequency bandwidth, even the same mode shows intra-modal dispersion. If the duct channel is terminated with reflective metal caps, there will also be multiple reflections from the metal ends, producing multipath dispersion. These three dispersion mechanisms (inter-modal, intra-modal and multipath) affect the frequency response of the duct channel and produce delay spreads in the time-domain [95].

## 4.3 Analysis and Simulation

The propagation modelling approach used here is based on the waveguide mode theory that allows one to model the channel response in the frequency domain [93]. Once we obtain the frequency response for a particular configuration, we can study time-reversal focusing in the medium. Fig. 4.1 shows a simple straight duct component. The channel properties between the transmitting and receiving antenna depend on the duct dimensions, type of terminations (reflection coefficient of the terminations are $\Gamma_1$ and $\Gamma_2$ ), operating frequency, and the distances ($L_1$, $L$, and $L_2$). The transfer function of this channel can be expressed as a sum of transfer functions of all propagating modes. The final closed-form expression for the magnitude of the complex frequency response of the duct channel

is given as [93]

$$|H(f)| = \frac{2R_0}{|R_0 + Z_a|^2} \left| \sum_{n=1}^{N} Z_n e^{-\gamma_n L} \frac{(1 + \Gamma_{1_n} e^{-2\gamma_n L_1})(1 + \Gamma_{2_n} e^{-2\gamma_n L_2})}{1 - \Gamma_{1_n} \Gamma_{2_n} e^{-2\gamma_n (L + L_1 + L_2)}} \right| \tag{4.1}$$

where $Z_a$ is the antenna impedance, $R_0$ is the internal impedance of the transmitter and receiver, $\gamma_n$ is the complex propagation constant, $Z_n$ is the probe impedance due to mode n, and N is the number of modes in the waveguide. The details of the propagation model have been described in [93].

Using the above propagation model, we first analyze the cylindrical waveguide cavity channel. Then the effect of bandwidth and the reflections are analyzed in a time-reversal system.

### 4.3.1 Single Antenna Time-Reversal focusing

The duct channel used for the simulations was a 0.3 m diameter cylindrical duct with a conductivity of $9 \cdot 10^5$. The antennas were quarter wavelength monopole antennas centered at 2.45 GHz. The distance between transmit and receive antennas ($L$) was 10 m, and the distance between the antennas to the end-cap ($L_1$ and $L_2$) was 1 m. The ends of the duct were terminated with a high-reflectivity material with a reflection coefficient of -0.88. The bandwidth of the transmit signal was set to 100 MHz centered at 2.45 GHz. The number of frequency points used was 1601, resulting in a frequency resolution of 62.5 kHz. The channel magnitude and frequency response is shown in Fig. 4.3. Fig. 4.4a shows the impulse response of the channel. The time domain response shows that the channel is quite dispersive with echos ringing up to $2\mu sec$. The RMS delay spread for the duct channel is 360 ns.

The impulse response is time-reversed, normalized in power, and re-transmitted back through the channel. After propagating back through the stationary and reciprocal channel, the signal focuses on the initial source position. Fig. 4.4b shows the focusing waveform obtained after the time-reversal waveform is resent through the channel. The next step is

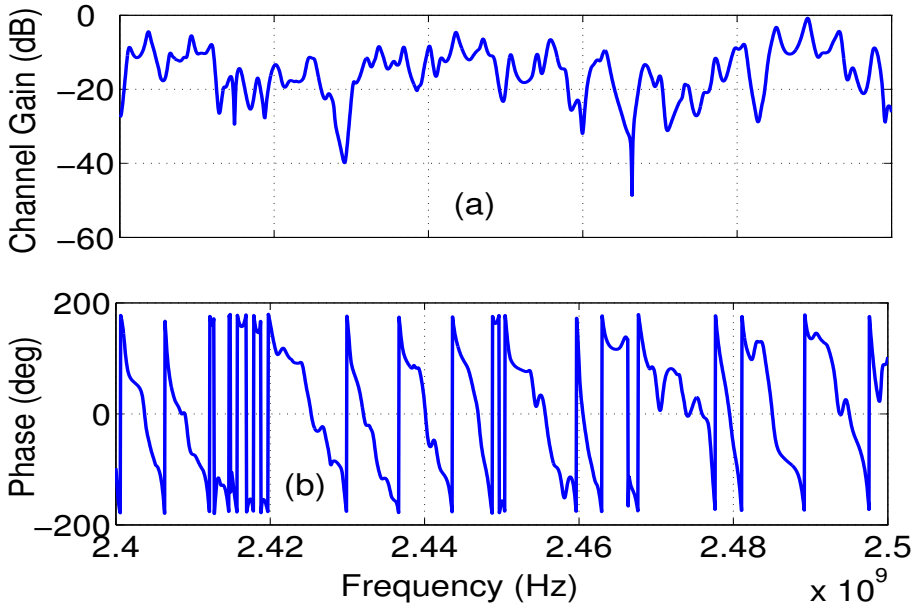


Figure 4.3: The simulated magnitude (a) and phase (b) response of the duct channel between 2.4-2.5 GHz.

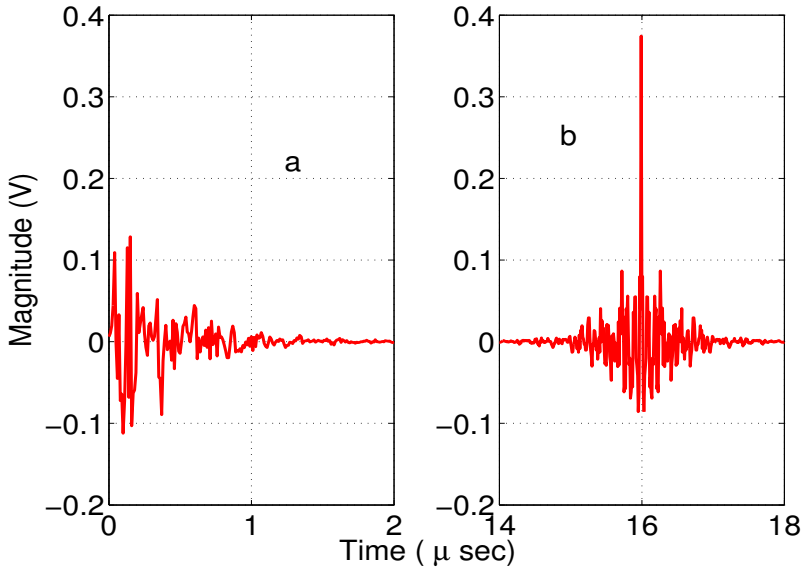


Figure 4.4: a) The forward channel impulse response b) The time-reversal waveform propagation results in focusing of time-domain waveform at the initial source.

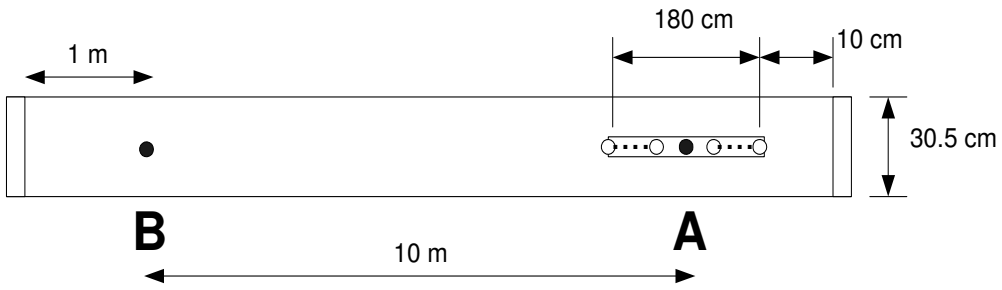


Figure 4.5: A waveguide slit is used to examine spatial focusing property of time-reversal system.

to analyze the spatial and temporal focusing property of the time-reversal system inside the duct channel. To that end, we did simulations using the setup as shown in Fig. 4.5. While transmitting a time-reversed signal intended to focus at A, the antenna is moved to both the right and left by 1 cm increments, and the focusing performance is examined. As we move away from the mid-point, we expect the focusing performance to be degraded. Fig. 4.6a shows the spatial and temporal power dispersion when a pulse is transmitted. As the horizontal axis in the figure illustrates, the time response extends to almost 400 ns. The vertical axis shows that the power is also distributed along a 16 cm long waveguide slit around the reference spot. Fig. 4.6b shows the focusing waveform after time-reversal signals are transmitted from the antenna at B. The time-reversal signals resulted in sharp focusing in time ( about 9 ns) and sharp focusing along the waveguide slit (6.4 cm). Note that the temporal focusing value is very close to the 10 ns time-resolution of the 100 MHz probing signal. Similarly the spatial resolution of the time-reversal signal is very close to the half-wavelength of the transmitted signal ($\lambda/2 = 6cm$). These results show that time-reversal back-propagation results in compression of the waveform both in time and space, focusing the RF energy around the initial source location.

### 4.3.2 Single Antenna Time-Reversal nulling

By modifying the time-reversed signal, we can have a nulling point at the receiver. In the case of focusing, all the multipath components add constructively at the receive position. For example, changing the polarity of the time-reversed signal during some portion of the

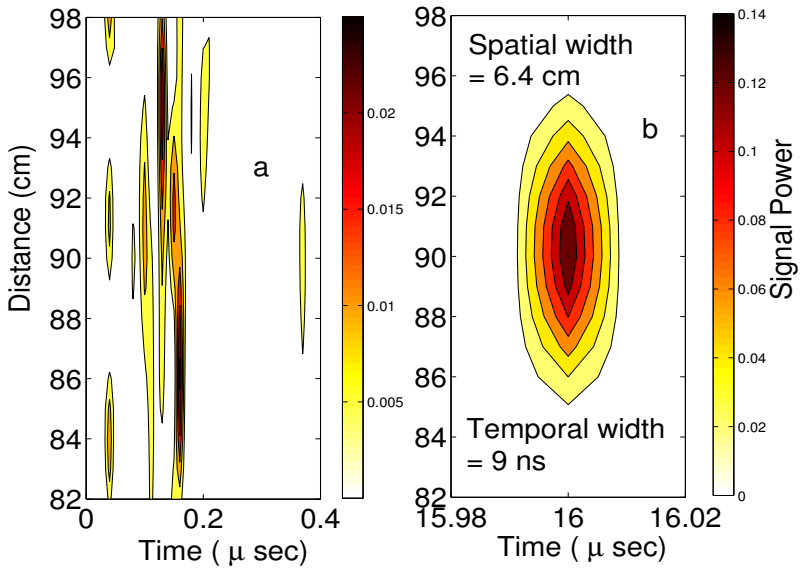


Figure 4.6: The temporal and spatial focusing of RF waves inside the duct channel. (a) Impulse response, and (b) response to the time-reversed signal. Note the difference in time-scales between parts (a) and (b).

waveform, we can create destructive interference, minimizing the signal amplitude at the receive antenna. Let us assume that the discrete time representation of the probing signal is $s(n)$, and the discrete time channel response is $h(n)$. The signal that reaches the receiver is $s(n)*h(n)$. As previously mentioned, the time-reversed waveform is $s(N-n)*h(N-n)$, where N is the maximum number of samples. The time-reversal waveform propagation results in focusing of the RF signal at the initial source, $y(n) = s(N-n) * h(N-n) * h(n)$, where the last two terms form the autocorrelation of the channel response:

$$r(n) = h(N-n) * h(n) = \sum_{k=-\infty}^{\infty} h(N-k) \cdot h(n-k) \tag{4.2}$$

When $n = N$, all the multipath components add in phase and the focused amplitude results. In contrast, consider the following waveform:

$$r_2(n) = \widetilde{h}(N-n) * h(n) \tag{4.3}$$

$$r_2(n) = \sum_{k=-\infty}^{L} h(N-k) \cdot h(n-k) + \sum_{k=L+1}^{\infty} (-1) \cdot h(N-k) \cdot h(n-k) \tag{4.4}$$

In the above equation, the sum is split into two parts. In the first part, the time-reversal waveform is the same as before. In the second part, time-reversal polarity has been changed. This is equivalent to multiplying the time-reversal waveform with a window function as shown in Fig. 4.7a. If $L$ is selected so that the two terms in Eqn. 4.4 have the same magnitude, at the instant $n = N$ they will cancel each other, minimizing the energy reaching the receiver. Another way to achieve minimum energy at the target location is to flip the sign of every other sample of the time-reversal waveform (Fig. 4.7b). So that when the time-reversal signal reaches the receiver, each sample will be 180 degrees out of phase with the previous sample. Fig. 4.8 and Fig. 4.9 show temporal and spatial time-reversal nulling and compare them with the focusing signal. In the simulations, we have used both nulling windows. They lead to different levels of nulling at the target location. In Fig. 4.8, the first nulling window resulted in attenuation of the focusing signal by 20 dB while the second nulling window reduced the focusing signal by 45 dB. Note that these nulling values are valid for one single time-instant. Fig. 4.9 shows that similar nulling results are valid for the spatial direction as well. By using conventional time-reversal, RF energy concentrates around the target antenna location and as we move away the energy becomes less. In the nulling case, we can produce a deep null at the target spot and as we move away the energy level increases.

### 4.3.3 Performance of time-reversal system with bandwidth

When a single antenna is used, the degrees of freedom arise from the bandwidth of the signal. Fig. 4.10 shows spatial focusing with bandwidths from 20 MHz to 1 GHz centered at 2.45 GHz. For lower bandwidths, due to the limited degrees of freedom available from the channel, the spatial sidelobes are quite strong. At 20 MHz for example, the spatial sidelobe levels are as big as the focusing waveform. As we increase the frequency, the sidelobe

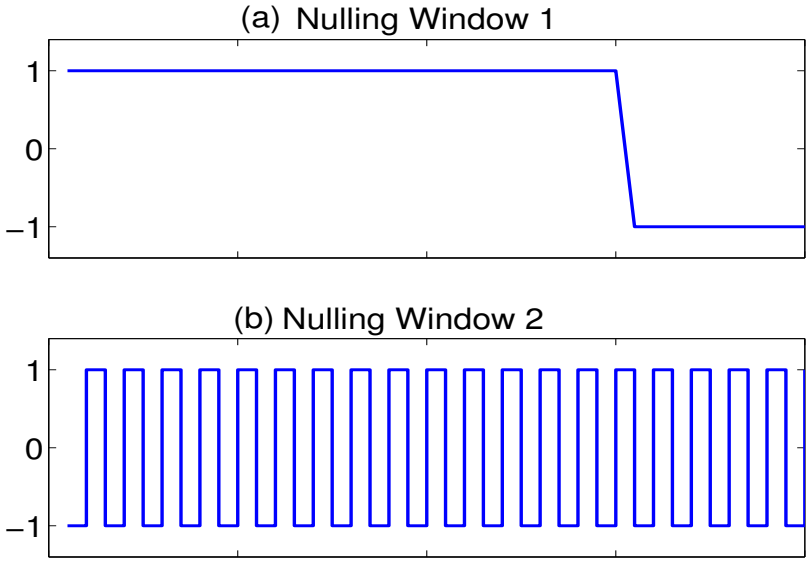


Figure 4.7: Nulling windows that result in minimal energy at the initial source when used with time-reversal. (a) The window equivalent to Equation 4.4, (b) window equivalent to reversing the sign of every sample.

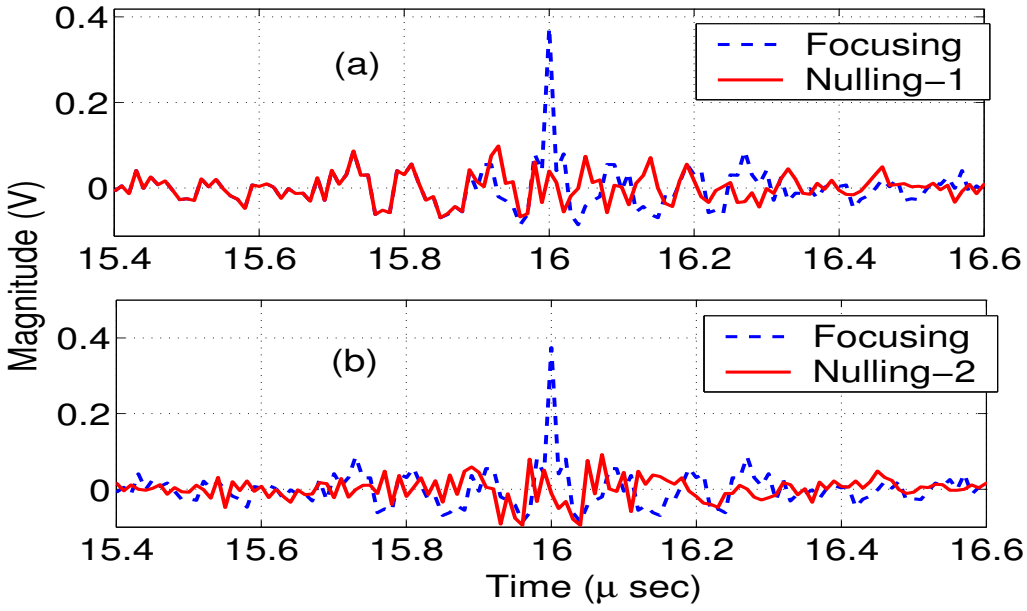


Figure 4.8: Temporal nulling at the target antenna site using the nulling windows shown in Fig. 4.7.

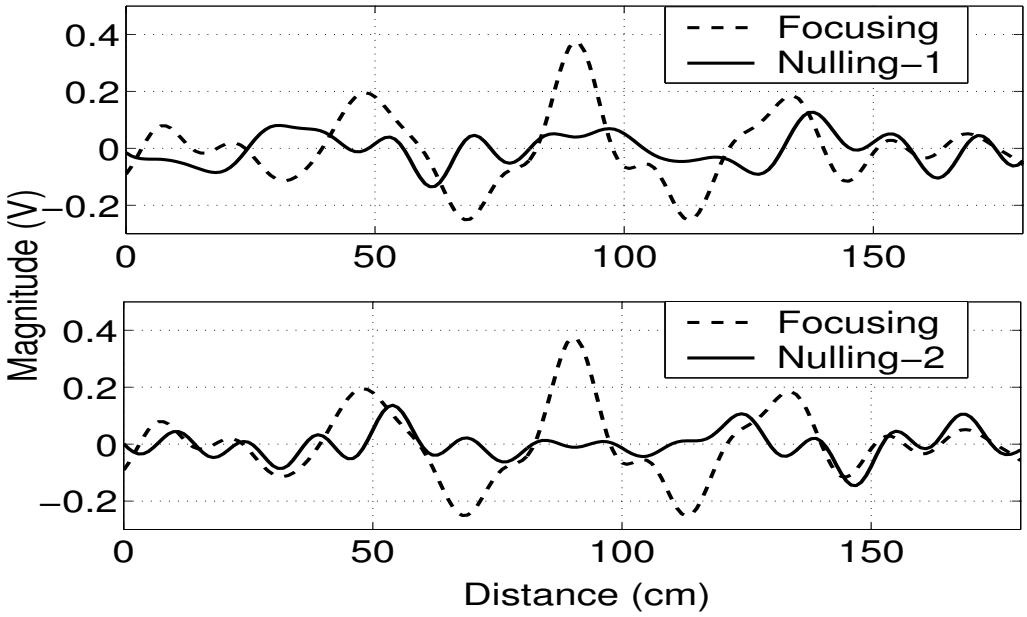


Figure 4.9: Spatial nulling at the target antenna site using the nulling windows shown in Fig. 4.7.

levels get smaller and the focusing waveform becomes more apparent. For example, using a bandwidth of 1 GHz, the peak-to-sidelobe ratio becomes as high as 13 dB. Fig. 4.11 shows the time-reversal temporal focusing with different bandwidths. The results suggest that for lower bandwidths, the temporal focusing is poor and the side-lobes are dominant. As we increase the bandwidth of the signal, temporal resolution becomes much sharper and the sidelobes get attenuated. Fig. 4.12 shows the spatial and temporal nulling across the same frequency band. We have used the nulling window as shown in Fig. 4.7a. The results show that the window function that we applied before re-transmission of the time-reversal waveform forces the mid-point to have as little power as possible. This minimum is localized in space and time in a manner similar to the focused signal.

### 4.3.4 Performance of time-reversal system with different reflectivities

In this section, we present results obtained by varying the reflectivity of the end-cap of the duct channel so that we obtain different amounts of dispersion in the channel. This is equivalent to changing the number of scattering objects in a free space environment. By

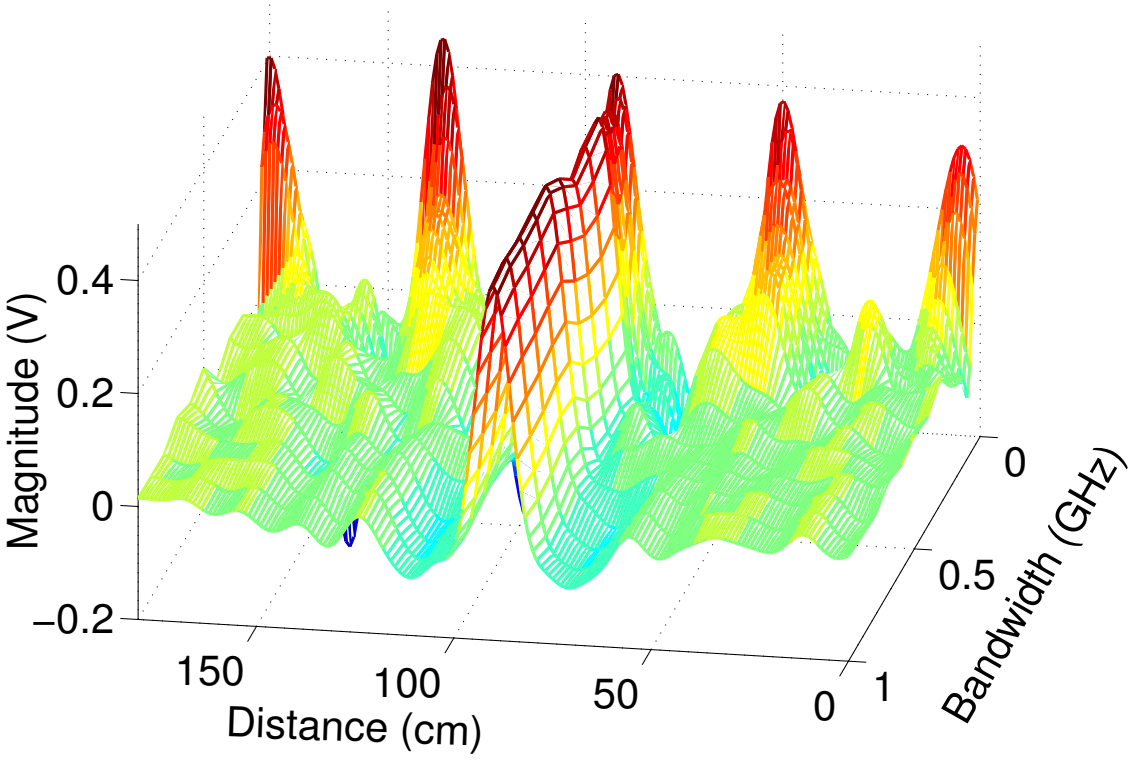


Figure 4.10: The performance of spatial time-reversal focusing with bandwidth.

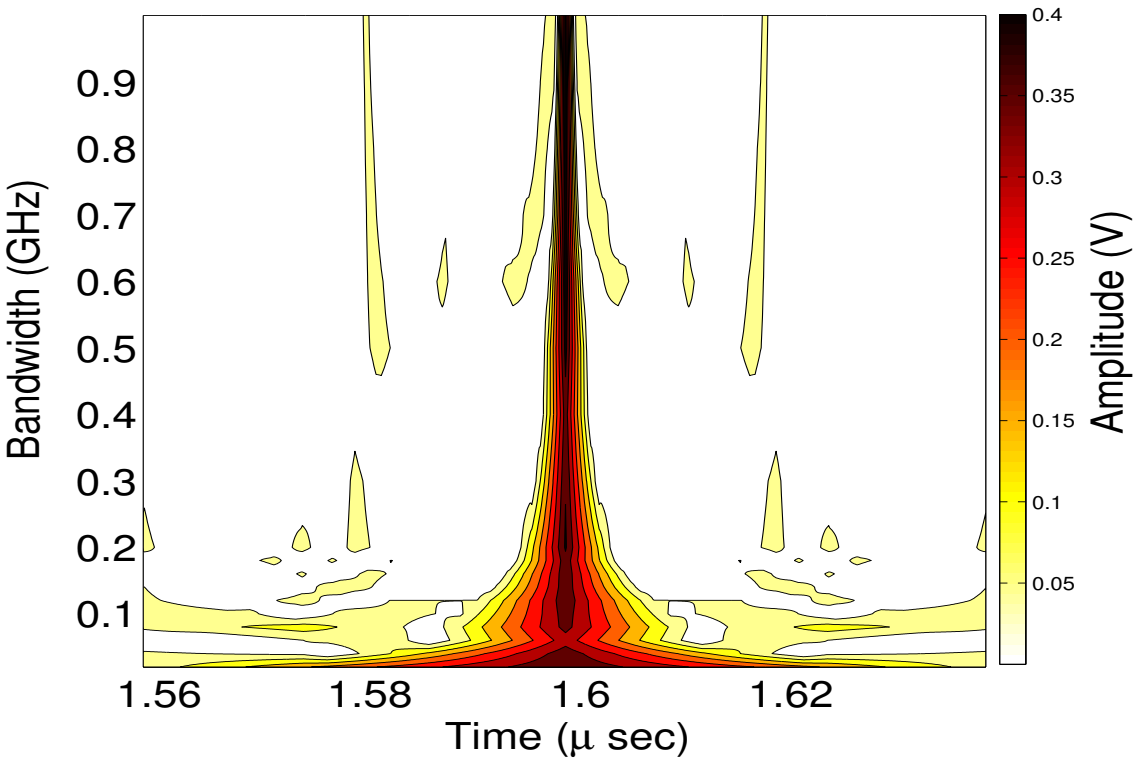


Figure 4.11: The performance of temporal time-reversal focusing with bandwidth.

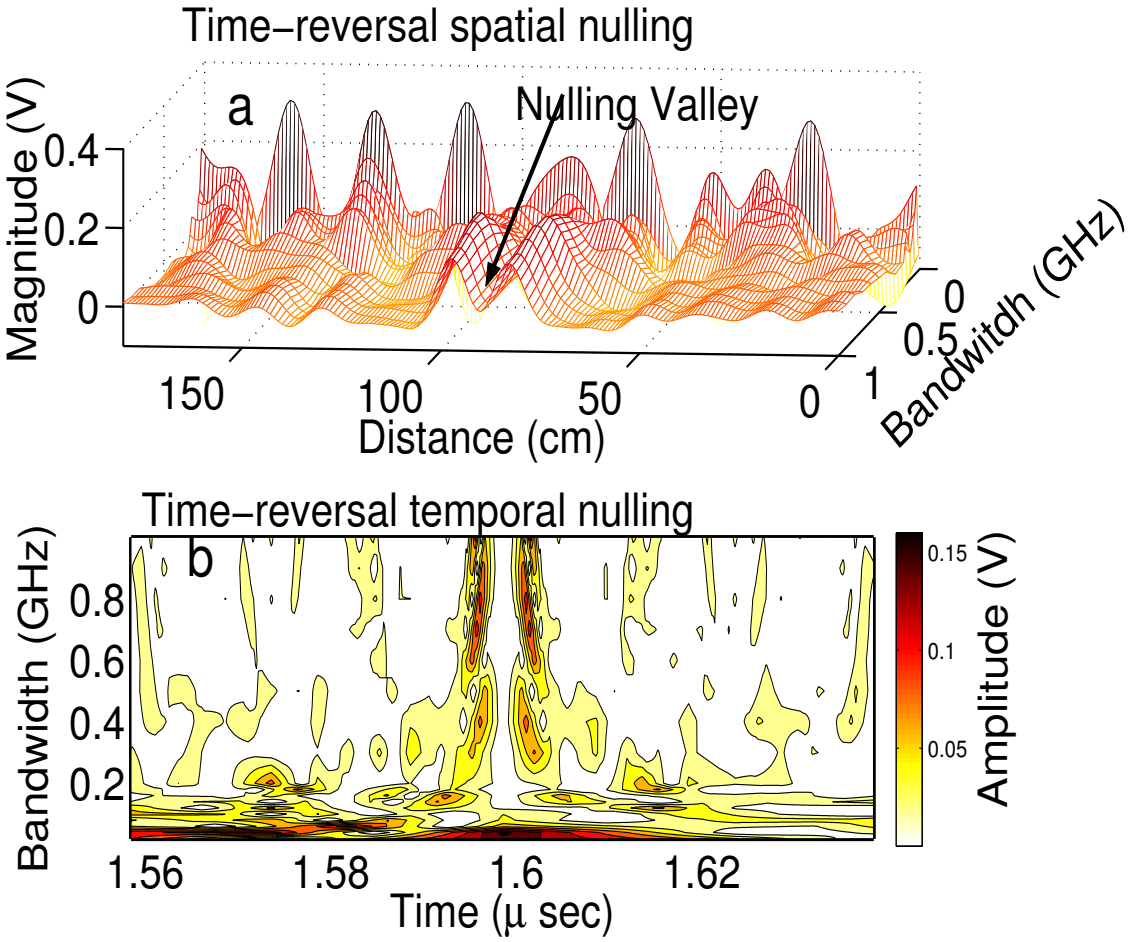


Figure 4.12: The performance of spatial (a) and temporal (b) time-reversal nulling with bandwidth.

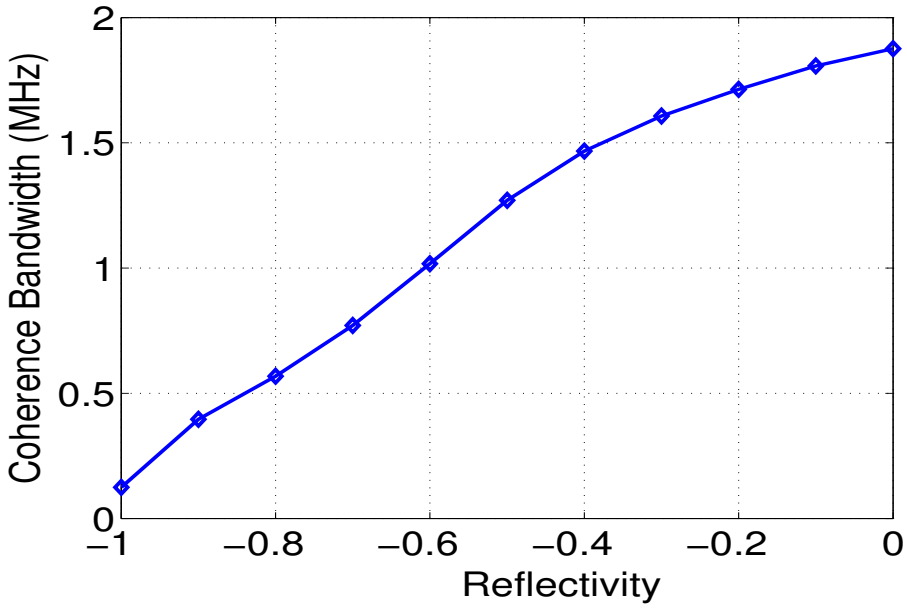


Figure 4.13: 90 % Coherence bandwidth with different reflectivity of the end-caps.

having different numbers of scattering objects in the medium, the power delay profile is changed. In a duct channel, as outlined before there are three mechanisms that affect the delay spread. These are intra-modal, inter-modal dispersion and multipath components. By changing the reflectivity of the end-cap, we can change the multipath components and change the delay spread of the medium. In the simulations, we have used the duct channel that was described before. The frequency bandwidth was set to 100 MHz with center frequency of 2.45 GHz. The reflectivity of the end-caps of the duct was changed from 0 (open ended) to -1 (perfect reflector) with an increment of 0.1. Fig. 4.13 shows the coherence bandwidth of the channel with different reflectivity end-caps. With open ends (reflectivity=0), the 90% coherence bandwidth is about 1.8 MHz, and with perfect reflector (reflectivity=-1), the coherence bandwidth drops to 0.1 MHz. Delay spread is inversely proportional to coherence bandwidth. Fig. 4.14 shows the temporal and spatial focusing with different levels of reflectivity. The focusing waveform to side-lobe ratio gets better as the medium becomes more reflective.

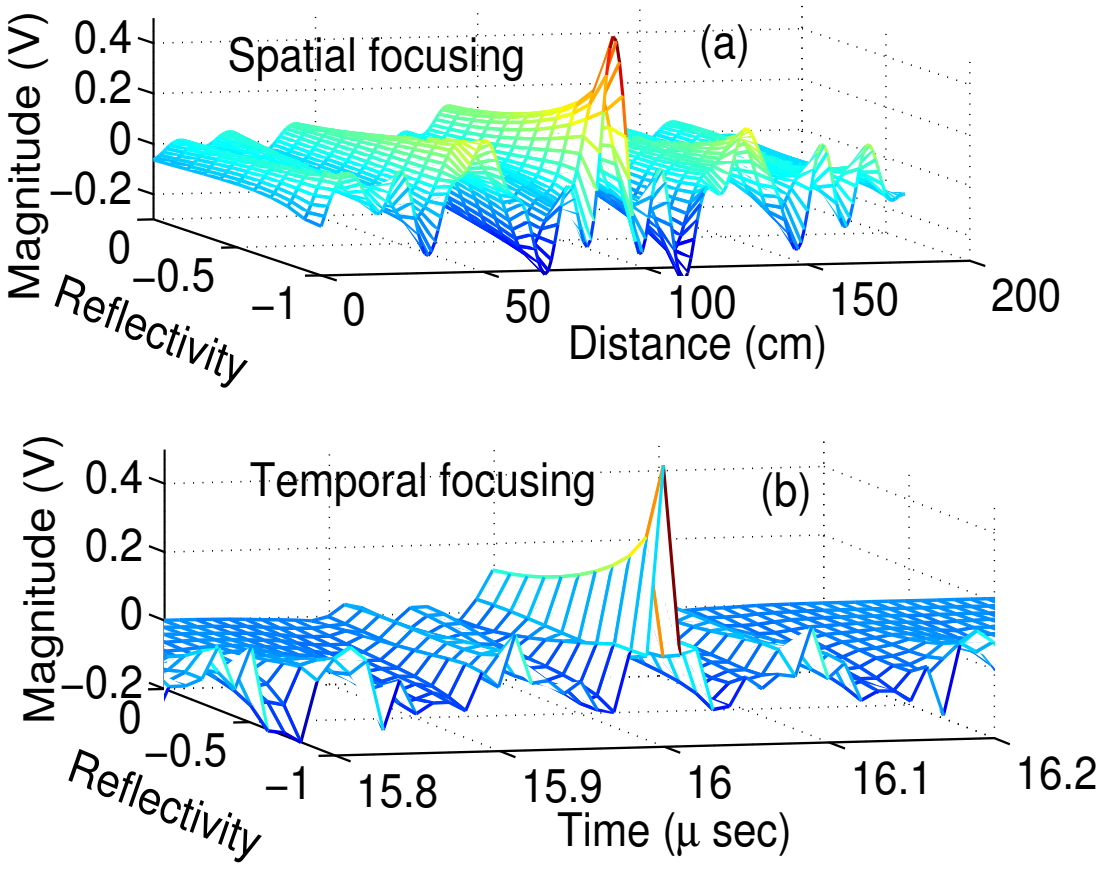


Figure 4.14: The performance of spatial (a) and temporal (b) time-reversal nulling with different reflectivity of the end-caps.

## 4.4 Experimental Setup

Time-domain experiments were performed using a digital signal generator and vector signal analyzer. The bandwidth of the instruments used is limited to 40 MHz. To observe the time-reversal effects, the channel response must be complex enough such that this bandwidth can be divided into several subbands that are relatively uncorrelated. Such a channel is provided by the cylindrical duct cavity used for the experiments. The experiments were done by using a 9.14 m long cylindrical duct with a diameter of 30.5 cm (see Fig. 4.15 and 4.16). The duct, simply a cylindrical waveguide, was made of galvanized steel with conductivity $\sigma = 10^6$. Both ends were closed with steel caps, resulting in a highly dispersive medium. In this experiment, we used omni-directional quarter wavelength monopole probe antennas with a center frequency of 2.45 GHz. In the time-reversal experiments, we used the points A and B (see Fig. 4.15) on the duct to place transceiver antennas. The antenna location B has multiple holes on the longitudinal and circumferential direction so that the antenna can be moved to make range and cross-range resolution measurements. There are a total of 13 antenna points on the duct spanning a distance of 33 cm in both the longitudinal and circumferential directions. The spacing between the antenna points was 3 cm. To have finer resolution around the reference point, we have 4 more antenna positions, each one of them 1.5 cm away from the reference point. The channel frequency response between point A and the mid-point on the B array is shown in Fig. 4.17a. The duct channel, viewed as an over-moded waveguide at RF frequencies, has the multipath richness through various propagating modes and reflections within the system. The multipath components in the cavity manifest themselves as frequency selective fading. The impulse response of the channel is shown in Fig. 4.17b. The maximum delay spread is approximately $2\mu s$, and the RMS value is approximately 270 ns.

Due to the bandwidth limitation of the instruments available in the lab, we generated a probing pulse that has 36 MHz frequency span (as shown in Fig. 4.18). The null-to-null pulse width is 100 ns and pulse spacing is 10 $\mu s$. All the echoes from the transmitter reach

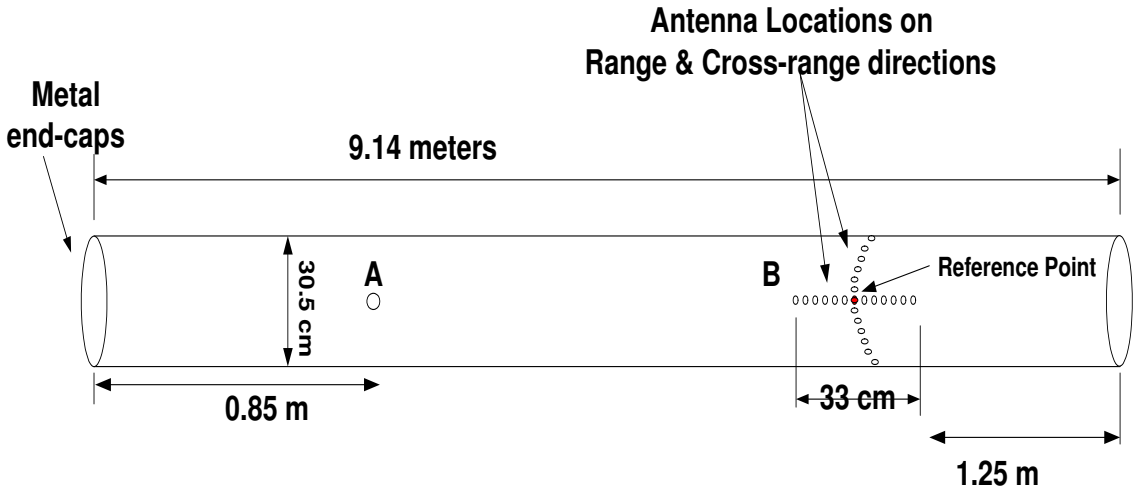


Figure 4.15: Duct channel used as a cavity environment.

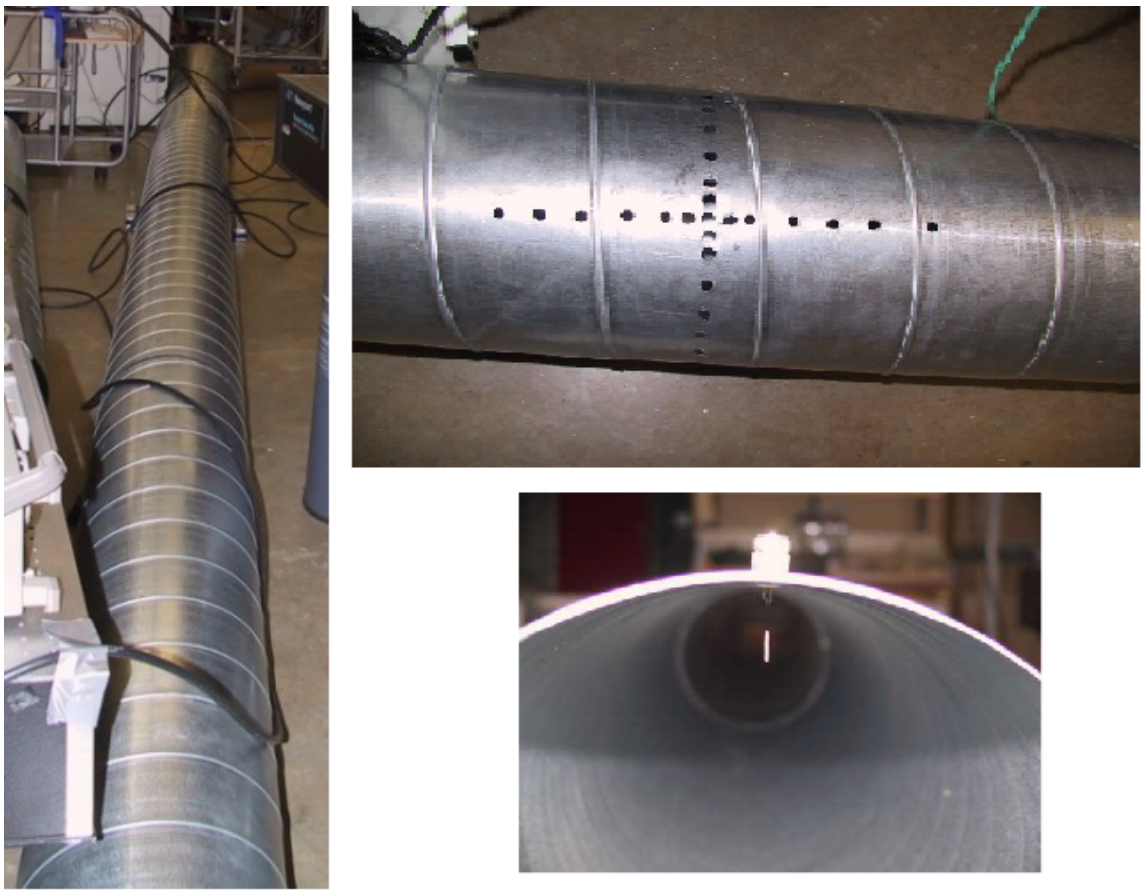

Figure 4.16: The duct that we used in the experiments. The range and cross range directions have antenna locations by 3 cm intervals. There are additional 4 more antenna locations which are just 1.5 cm away from the mid-point.

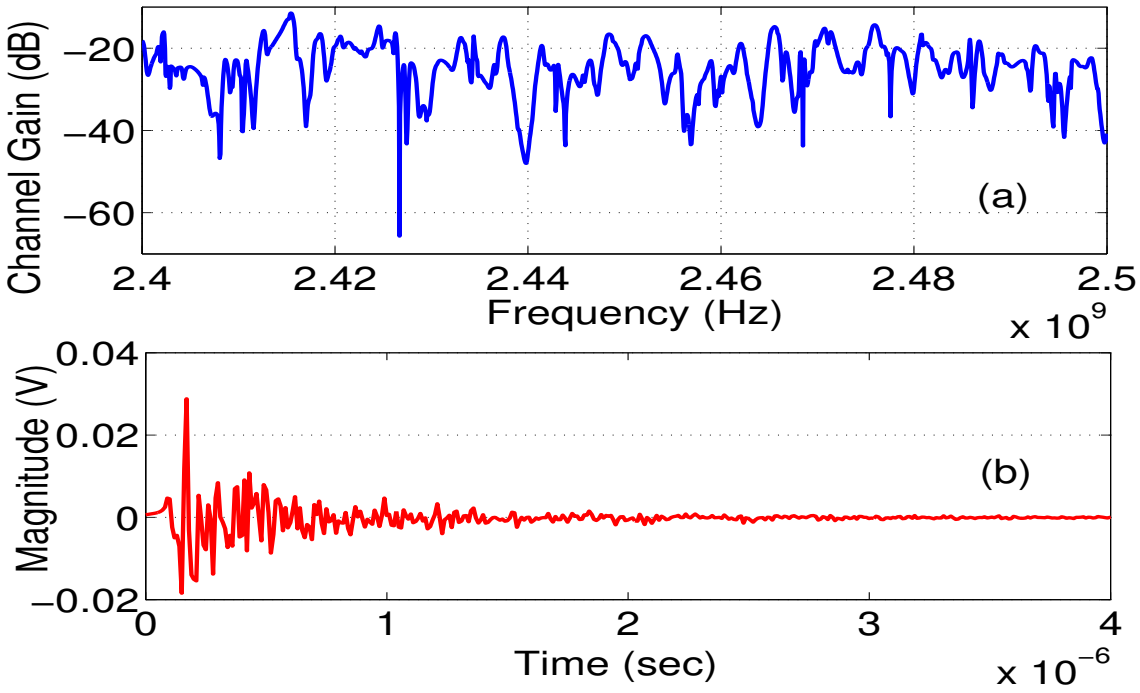


Figure 4.17: a) Frequency response of the channel b) The channel impulse response.

the receiver within this duration. The pulse spectrum, real and imaginary part of the pulse and I-Q plot are shown in Fig. 4.19 as taken from the instruments.

As an in-phase component (I-data), this pulse is uploaded to an Agilent Digital Signal generator (E4433B) and upconverted to a frequency of 2.45 GHz as shown in the signal flow graph of Fig. 4.20. The RF signal propagates through the duct in multiple modes and the dispersed waveform is captured with a probe antenna. The signal is downconverted to 20 MHz by using an Agilent E8251A PSG-A as a local oscillator and Miteq TB02118LA1 mixer. The downconverted signal is digitized for the in-phase (I-channel) and quadrature (Q-channel) components with the help of an Agilent 89610A vector signal analyzer. The I and Q waveforms of the baseband received pulse are shown in Fig. 4.21a and b. The time-reversed I and Q waveforms (Fig. 4.21c and d) are sent back from the same antenna. Note that we change the sign of the Q-waveform to account for the phase conjugation of the carrier frequency [63].

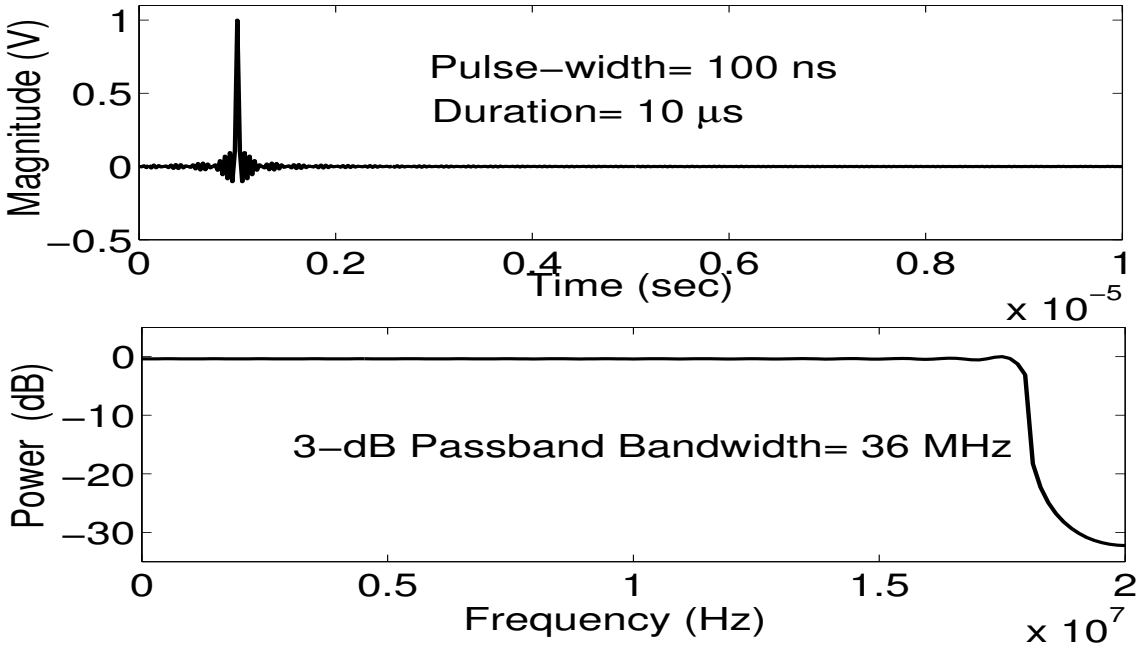


Figure 4.18: The 100 ns pulse is generated in Matlab and uploaded to the signal generator.

### 4.4.1 Results and Discussions

After sending the time-reversed signal from transceiver A, we observe focusing both in the longitudinal (Fig. 4.22) and circumferential (Fig. 4.23) directions at transceiver B. As we move the probe antenna on the waveguide in either direction from the original location, we can see that the signal loses its focusing effect. The degree of degradation can be found by doing spatial correlation between all the neighboring points [96]. In the case of nulling, we again use the same time-reversed waveforms (Fig. 4.21c and d). This time, we change the polarity of part of the I and Q waveforms so that there will be destructive interference. We have used both nulling windows described before. The experimental spatial and temporal nulling results using the first nulling window (Fig. 4.7a) is shown in Fig. 4.24. Fig. 4.25 shows the temporal and spatial nulling results using the second nulling window as shown in Fig. 4.7b. It can be seen that there is a null at the original point, and as the probe moves away from the original point, the signal starts to become stronger. Fig. 4.26 compares the focusing and nulling waveforms at the reference point. The first nulling algorithm

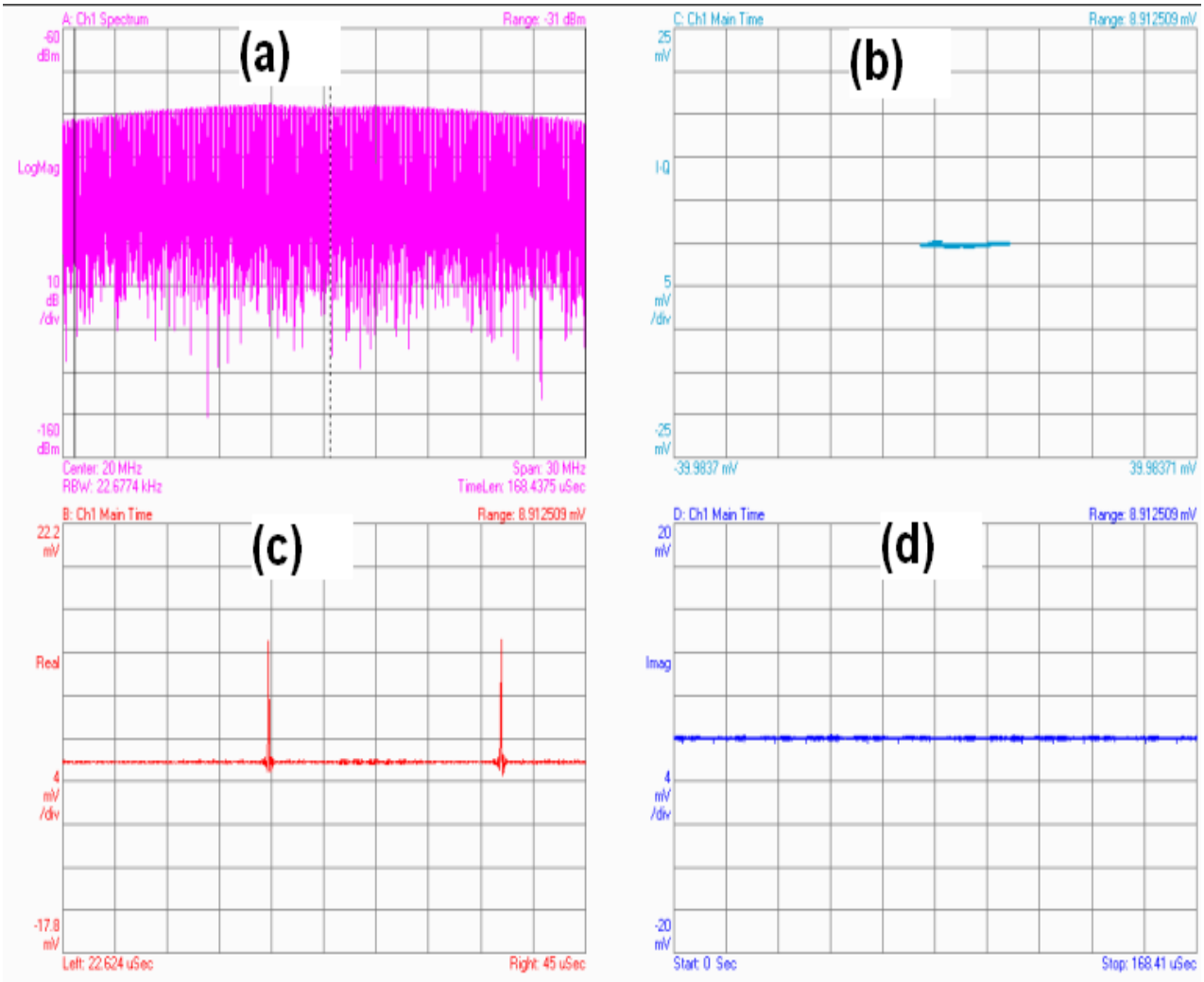


Figure 4.19: The uploaded signal is up-converted to 2.45 GHz and through a short cable down-converted to IF frequency of 20 MHz. a) Pulse spectrum, b) I-Q plot of pulse waveform, c) Time-dependence of in-phase component, d) time-dependence of quadrature component of pulse.

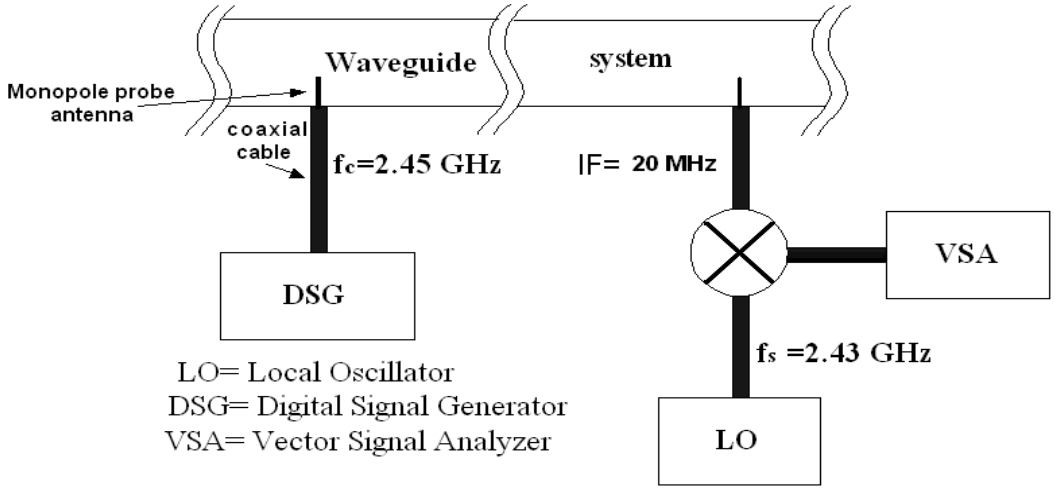


Figure 4.20: Digital signal generator and vector signal analyzer are used to transmit and receive time-reversed signals.

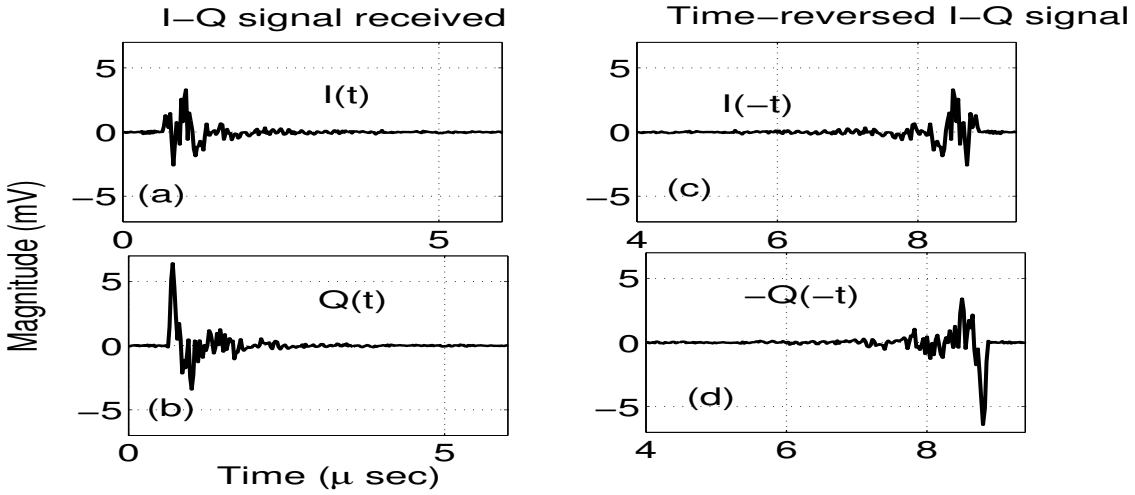


Figure 4.21: (a)-(b) The I and Q signals captured at the receiver. (c)-(d) Time reversed I and Q waveforms transmitted back.

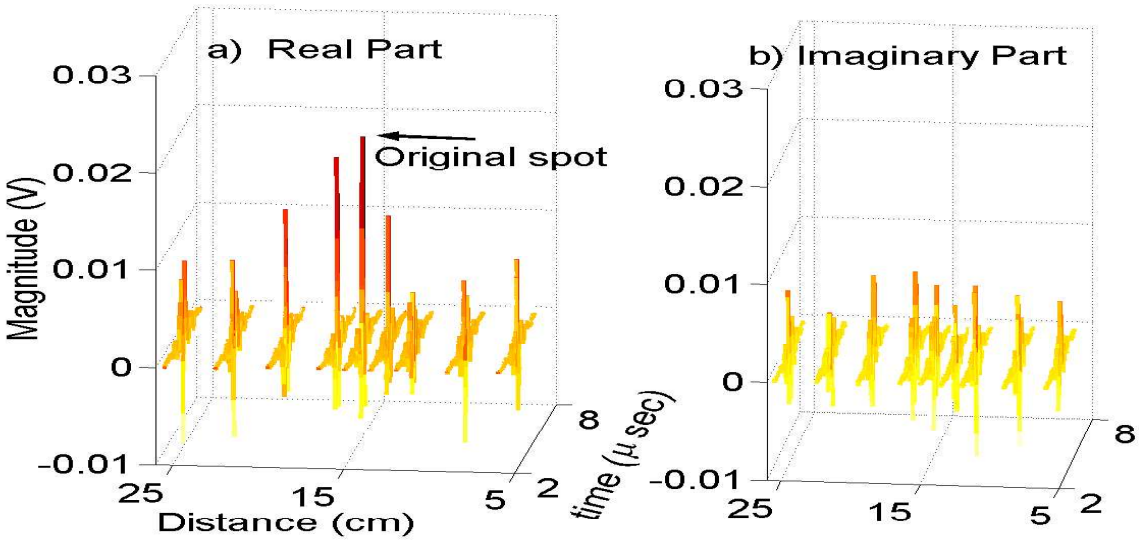


Figure 4.22: Spatial and temporal focusing along the longitudinal direction on the waveguide.

attenuated the focusing signal by 20 dB, while the second one 12 dB.

## 4.5 Conclusions

Time-reversal systems have been generally constructed using multiple antennas. The main reason for that is to utilize the spatial degrees of freedom. In this chapter, we have shown that it is also possible to construct a time-reversal system using a single antenna. The spatial and temporal microwave signal focusing and nulling have been shown using a single antenna and the time-reversal method. The simulation results have shown that time-reversal focusing depends on the bandwidth of the waveform and the reflectivity of the medium. We have described a novel method of interference cancellation using a single antenna. The multipath components in the duct have been utilized to cancel the signal at the target location. The physical time-reversal experiments have been conducted in a cylindrical cavity environment and we have demonstrated single antenna focusing and nulling both in the longitudinal direction as well as in the circumferential direction. The focusing and nulling waveforms were obtained using 36 MHz bandwidth at 2.45 GHz. The single antenna interference cancellation schemes presented in this chapter can be used

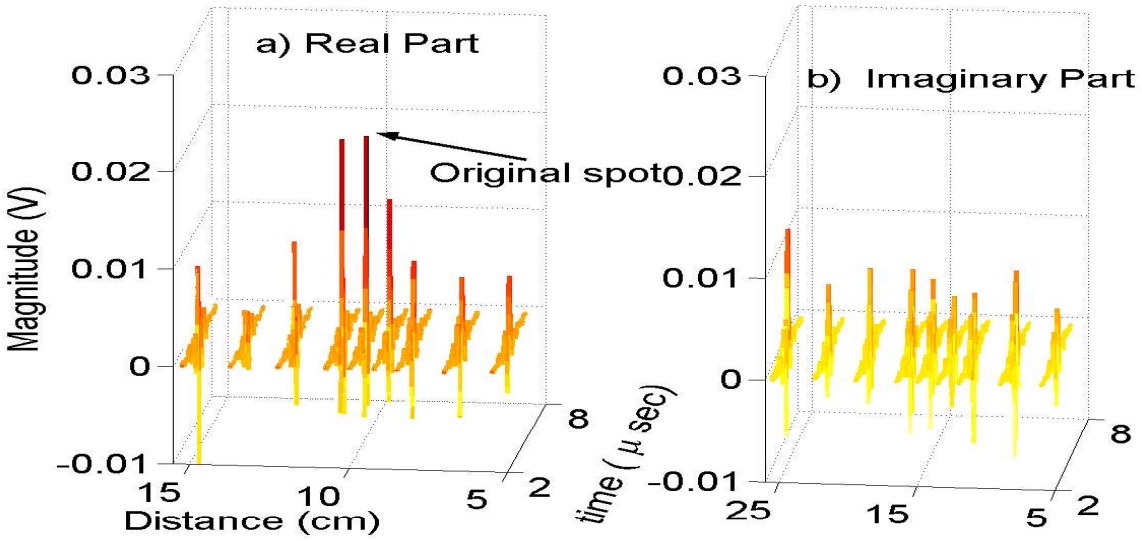


Figure 4.23: Spatial and temporal focusing along the circumferential direction on the waveguide.

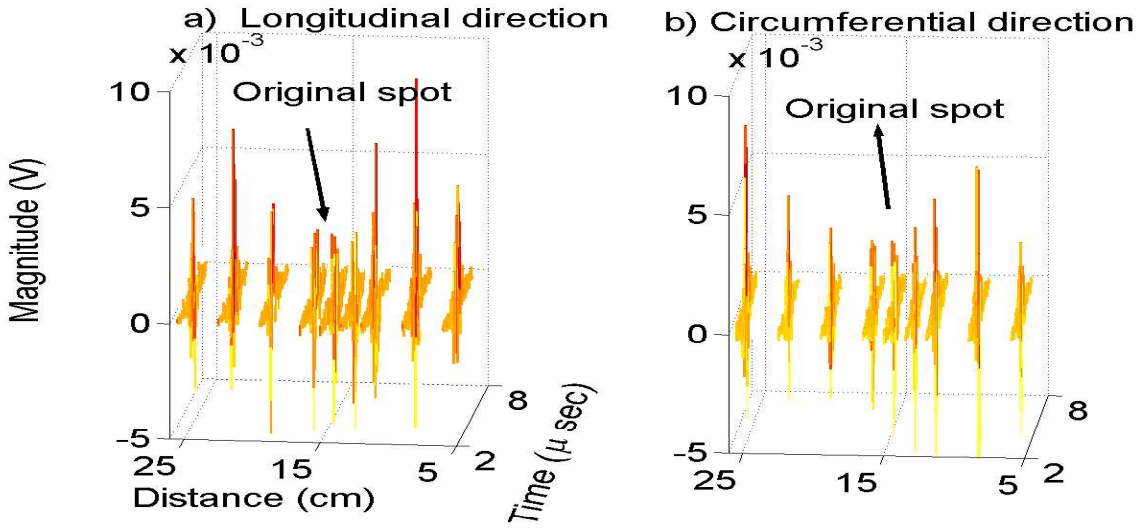


Figure 4.24: Spatial and temporal nulling along longitudinal and circumferential directions using the nulling window 1. a) Longitudinal direction b) Circumferential direction.

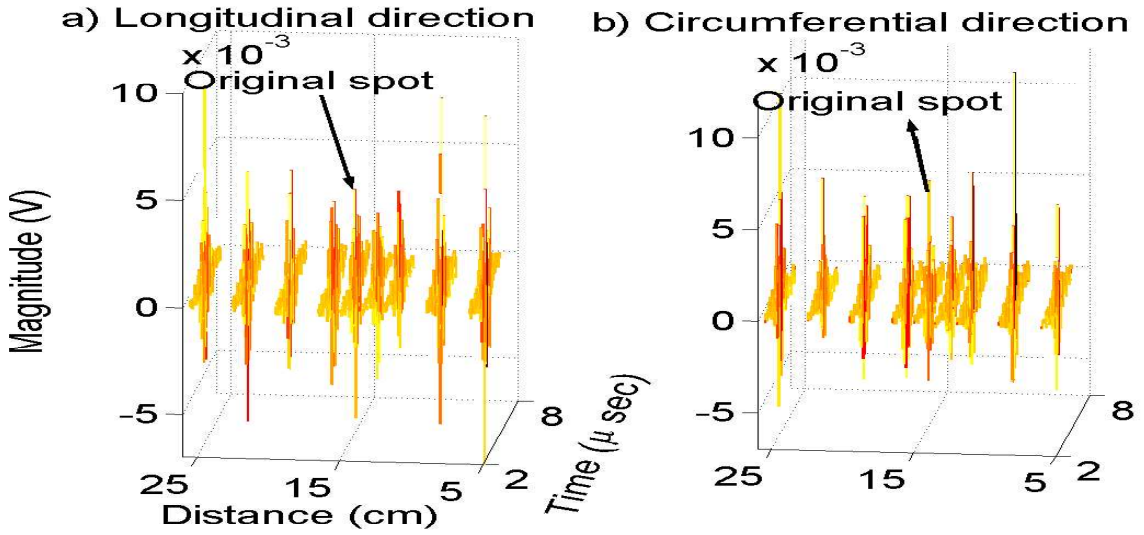


Figure 4.25: Spatial and temporal nulling along longitudinal and circumferential directions using the nulling window 2. a) Longitudinal direction b) Circumferential direction.

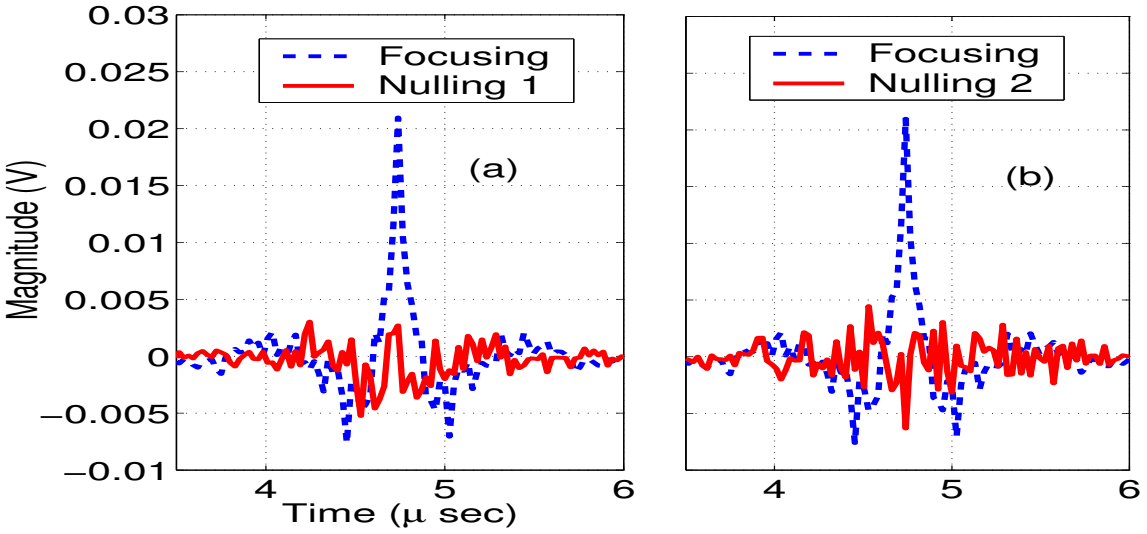


Figure 4.26: Focusing and nulling waveforms at the original point. a) Nulling with window 1 b) Nulling with window 2.

for target detection algorithms in highly cluttered environments. The later topic will be discussed further in Chapter 5.

# Chapter 5

# Target detection using time-reversal techniques

## 5.1 Introduction

In a conventional radar system, the signal emitted by a radar propagates through the medium between the radar and the target, reflects from the target, and is received by the radar antenna. The performance of the radar depends on the channel which can be analyzed by considering two limiting scenarios. In the first one, the target is the only object in the range of the radar, i.e. the channel impulse response is a delta function. The optimum solution is achieved by using a matched filter approach. In the second case, a large number of scattering objects exist in the channel so that the signal emitted by the radar is scattered by these objects and the channel impulse response is now very complex. When the channel propagation structure is complex, the performance of the matched filter rapidly deteriorates. In complex scattering environments, time-reversal processing can be used to focus the energy around the target and improve the detection performance of a conventional radar system. In this chapter, we analyze target detection performance using time-reversal techniques at RF frequencies. The time-reversal based detection schemes will be examined that use a single antenna as well as multiple antennas. We will examine two

methods using multiple antennas. The first one simply uses time-reversal to focus energy on the target. The second method uses time-reversal nulling to first minimize the response from the clutter. When the target enters into the medium, time reversal focusing is then used to increase the energy on the target so that a stronger echo is obtained. This method is called time-reversal adaptive interference cancellation technique (TRAIC) and has been analyzed through simulations [65], and experimentation [68]. It utilizes an even number of antennas and a time-reversal method to maximize energy on the target that enters into a cluttered medium. The experimental results have shown that using the TRAIC algorithm, we can improve the signal-to-noise ratio of the return-echo due to the target compared to conventional change-detection radar. The detection performance of a target that is hiding behind a metal object is also improved with the TRAIC algorithm. The TRAIC algorithm was also implemented using a single antenna [66].

## 5.2 Single Antenna Time-Reversal Detection

### 5.2.1 Matched Filter in cluttered Medium

In the simplest case where there is only one target in the range of the radar, the channel response can be characterized as

$$h(t) = a \cdot e^{j\theta}\delta(t - t_0) \tag{5.1}$$

where $a$, $\theta$ and $t_0$ are the channel gain, channel phase and the propagation time delay respectively. The received radar signal due to an input signal *s(t)* is

$$r(t) = \int_{-\infty}^{\infty} s(\tau)h(t - \tau)d\tau + n(t) \tag{5.2}$$

$$r(t) = a \cdot e^{j\theta}s(t - t_0) + n(t) \tag{5.3}$$

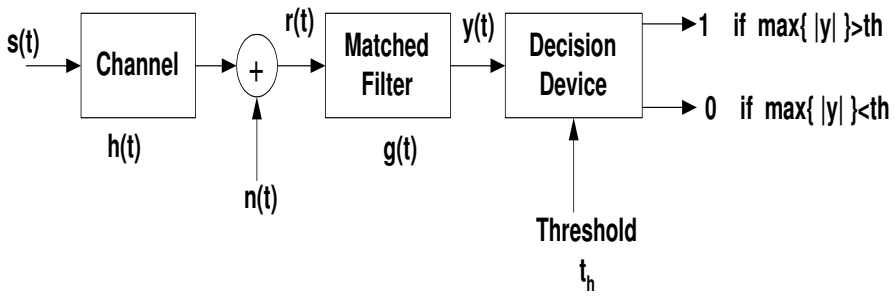


Figure 5.1: The signal flow graph in matched filter detection.

where *n(t)* is complex additive white Gaussian noise. Equation 5.3 represents the received signal when there is only a single object in the range of the radar and the object to the antenna distance is $c \cdot t_0/2$, where $c$ is the speed of light. The output SNR is defined as the ratio of signal power received from the channel to the additive noise power. It is given as

$$SNR_{output} = \frac{\int_{-\infty}^{+\infty} |r(t)|^2 dt}{\int_{-\infty}^{+\infty} |n(t)|^2 dt} - 1 \tag{5.4}$$

It is possible to improve this ratio by using a filter to emphasize the signal component. It is well known that the optimal filter to improve the $SNR_{output}$ is a matched filter [97]. The general signal flow graph is shown in Fig. 5.1. The transmitted waveform propagates through an environment and reflects from the objects in the medium and the echoes are collected with the help of a receive antenna. Complex noise is added due to the receiver circuitry. Then, the summed signal passes through a matched filter with an impulse response given by

$$g(t) = \begin{cases} k \cdot s(T-t) & 0 \leq t \leq T, \\ 0 & elsewhere. \end{cases}$$

where k is a constant. The matched filter simply correlates the received signal with the original transmitted waveform. After matched filtering, a threshold is used to make the decision as to whether or not there is an object in the medium. Since the matched filter is a linear device, the received signal after the matched filtering can be divided into two parts:

the signal component ($y_s(t)$) and the noise component ($y_n(t)$). The signal component $y_s(t)$ can be described by

$$y_s(t) = \int_{-\infty}^{\infty} S(f)H(f)G(f)e^{j2\pi ft}df \tag{5.5}$$

$$y_s(t) = \int_{-\infty}^{\infty} S(f)ae^{j\theta}e^{-j2\pi ft_0}kS^*(f)e^{-j2\pi fT}e^{j2\pi ft}df \tag{5.6}$$

where $S(f)$ is the Fourier transform of the transmitted waveform $s(t)$, $H(f)$ is the frequency domain representation of the propagation channel, $G(f)$ is the Fourier transform of the matched filter response $g(t)$. The maximum value of $y_s(t)$ happens at $t = T + t_0$ and is given as

$$max[y_s(t)] = kae^{j\theta}\int_{-\infty}^{\infty} |S(f)|^2 df \tag{5.7}$$

The additive white complex noise $n(t)$ has a power spectral density of $N_0/2$. The power spectral density of noise after the matched filter is equal to the power spectral density of the input noise times the power spectral response of the matched filter. The power spectral density of noise after the matched filter is given as

$$Y_N(f) = \frac{N_0}{2}|G(f)|^2 = \frac{N_0|S(f)|^2}{2} \tag{5.8}$$

The average noise power $y_n(t)$ is therefore

$$E[y_n(t)^2] = \frac{N_0}{2}\int_{-\infty}^{\infty} k^2|S(f)|^2 df \tag{5.9}$$

The maximum value of peak signal-to-noise ratio occurs at time $t = t_0 + T$ and the ratio is given as

$$SNR_{max} = \frac{|y_s(t_0+T)|^2}{E[y_n(t_0+T)^2]} \tag{5.10}$$

$$SNR_{max} = \frac{|kae^{j\theta} \int_{-\infty}^{\infty} k^2 |S(f)|^2 df|^2}{E[\frac{N_0}{2} \int_{-\infty}^{\infty} |S(f)|^2 df]} \tag{5.11}$$

$$SNR_{max} = \frac{2a^2 \int_{-\infty}^{\infty} |S(f)|^2 df|}{N_0} \tag{5.12}$$

$$SNR_{max} = \frac{2a^2 E_s}{N_0} \tag{5.13}$$

where $E_s = \int_{-\infty}^{\infty} |S(f)|^2 df$ is the signal energy of the transmitted waveform.

When the channel propagation structure is complex, the channel impulse response becomes

$$h(t) = \sum_{k=0}^{N-1} a_k \cdot e^{j\theta_k} \delta(t - t_k) \tag{5.14}$$

where N is the number of multipath components. The matched filter transfer function stays the same, as does the average noise power at the output of the matched filter. The signal component changes to

$$y_s(t) = \int_{-\infty}^{\infty} S(f) \sum_{k=0}^{N-1} a_k \cdot e^{j\theta_k} e^{-j2\pi f t_k} k S^*(f) e^{-j2\pi f T} e^{j2\pi f t} df \tag{5.15}$$

The maximum value of $y_s(t)$ happens at time $t = T + t_M$, where $t_M$ is the delay of the strongest multipath component that has amplitude $a_M$ and phase $\theta_M$. In other words, the decision device of Fig. 5.1 finds the peak value after the matched filter and compares to a threshold level. We have used the experimental test setup described in Chapter 2 to test the performance of a matched filter in various degrees of clutter. Measurements were made of 201 points between 4 and 6 GHz, using single transmit and receive antennas. The impulse responses are obtained through IFFT of the complex channel frequency responses, and the matched filter is implemented in the time-domain. The following steps were followed to

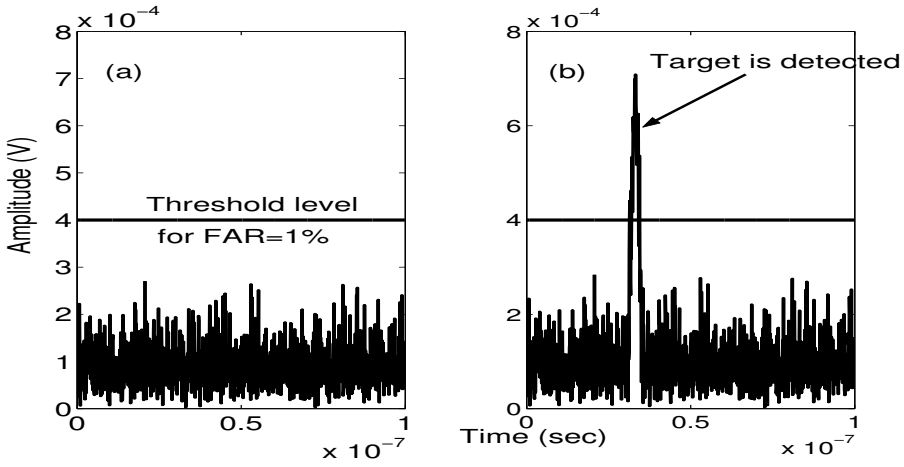


Figure 5.2: The steps in the detection scheme. (a) The threshold level is calculated for a given false alarm rate (FAR) (b) The peak-output of matched filter is compared with the threshold.

compute the performance.

1. An SNR value of -10 dB is chosen (as given by Eqn. 5.4).

2. In the absence of any object in the medium, the threshold levels are calculated for different false alarm rates (FAR) between 0 and 1 (Fig. 5.2a).

3. In the presence of object(s) in the medium, the matched filtering operation is performed and the peak is compared to the threshold level for a particular FAR (Fig. 5.2b). If it is greater than the threshold, the target is detected, otherwise not. This process is repeated 1000 times, each time with a different noise realization. The performance of the detector is evaluated by computing the probability of detection $P_D$ for different false alarm rates (FAR).

4. The detection probability of the matched filter is averaged over 20 channels with the same channel configuration but different antenna position. 20 channels have been chosen randomly among 100 channels measured for the 10 x 10 virtual antenna array (Chapter 2).

The performance of the matched filter for various numbers of scattering objects is plotted in Fig. 5.3. It is clear from this figure that the performance is the best in the case of

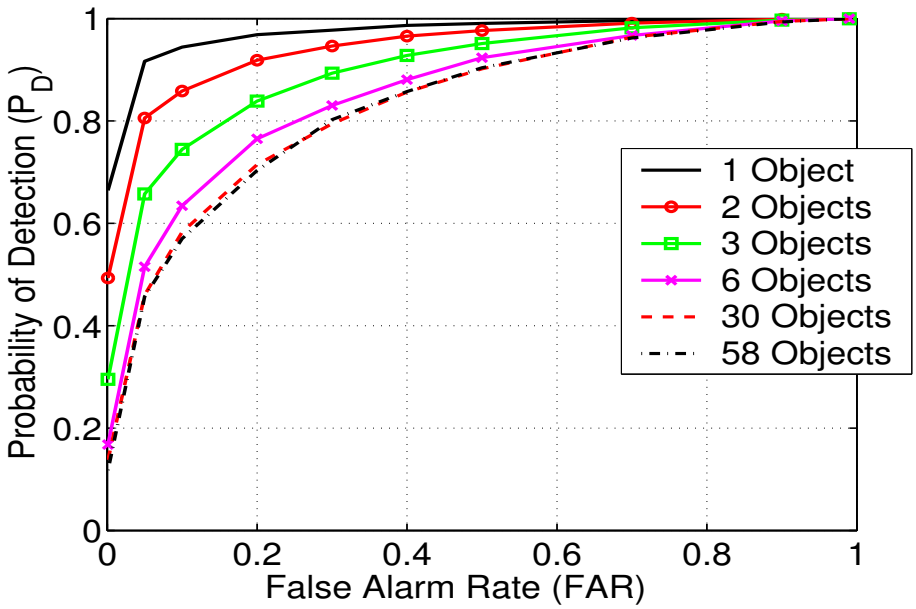


Figure 5.3: The performance of matched filter with various numbers of scattering objects in the field. The SNR is -10 dB.

single object in the channel. As we increase the number of objects in the medium, the matched filter performance deteriorates. The matched filter performance saturates as the number of scattering objects is increased. The performance of the matched filter using 30 scattering objects is very similar to the one using 58 scattering objects. This is due to the density saturation effects described in Chapter 2.

The optimal detector would use a test statistic that is sampled from the output of a filter matched to $h(t) * s(t)$, not to $s(t)$. This is referred to as the matched field receiver. The problem with the matched field receiver is that it requires knowledge of the channel response $h(t)$ between the radar antenna and the target for every possible target position. This is a difficult process that involves intensive field measurements or computations. Time reversal provides a practically feasible way of using the channel structure, without actually modelling the channel or knowing explicitly the channel's impulse response. In the next section, we will describe a time-reversal based detection scheme in complex scattering environments.

### 5.2.2 Energy Detector: Comparison of Time-reversal detection and Change Detection

Time-reversal is equivalent to phase-conjugation in the frequency domain. The energy detector analysis will be carried out in the frequency domain. In the absence of the target, the clutter channel response is given by $H_c(f)$. This is the background channel response. When the target enters into the medium, the channel frequency response becomes as $H_{ct}(f)$. This can be decomposed into a component due to clutter ($H_c(f)$) and a component due to the target ($H_t(f)$). The target component also includes all higher order scattering from the clutter to the target. In the following, we assume that we can null-out the clutter and work only with the response from the target. The channel is assumed to be stationary, i.e. the forward and backward channel frequency response is identical. The forward and time-reversal channel responses can be written as

$$Y(f) = H_t(f) + N_1(f) \tag{5.16}$$

$$Z(f) = kY^*(f)H_t(f) + N_2(f) \tag{5.17}$$

where $N_1(f)$ and $N_2(f)$ are additive white noise at the two ports and $k$ is a back-propagation constant that is used to make sure that the transmitted power is normalized in each cases. In the above equation $Y(f)$ is the waveform due to change detection and $Z(f)$ is the time-reversal waveform. The normalization of k will enable us to do a fair comparison of time-reversal based detection schemes and conventional change detection schemes. $k$ is given by

$$k^2 \sum_{q=0}^{Q-1} |Y(f_q)|^2 = Q \tag{5.18}$$

where Q is the number of frequency components. The energy of the time-reversal based detector can be calculated as

$$E_{TR} = \sum_{q=0}^{Q-1} |Z(f_q)|^2 = \sum_{q=0}^{Q-1} |kY^*(f_q)H_t(f_q) + N_2(f_q)|^2 \tag{5.19}$$

Similarly the energy for a change-detection scheme is

$$E_{CD} = \sum_{q=0}^{Q-1} |Y(f_q)|^2 = \sum_{q=0}^{Q-1} |H_t(f_q) + N_1(f_q)|^2 \tag{5.20}$$

In the high SNR scheme where $|H_t(f)|^2 >> |N(f)|^2$, the ratio of the time-reversal energy to change detection energy is given by

$$R = \frac{E_{TR}}{E_{CD}} = \frac{k^2 \sum_{q=0}^{Q-1} |H_t(f_q)|^4}{\sum_{q=0}^{Q-1} |H_t(f_q)|^2} \tag{5.21}$$

$$R = \frac{E_{TR}}{E_{CD}} = \frac{Q \sum_{q=0}^{Q-1} |H_t(f_q)|^4}{(\sum_{q=0}^{Q-1} |H_t(f_q)|^2)^2} \tag{5.22}$$

This ratio gives the advantage of time-reversal detection to change-detection. We now examine the time-reversal based detection gain compared to change detection for two different channel conditions.

1. No scattering objects in the medium other than the target itself, where the target channel response is perfectly flat i.e. $H_t(f) = Ae^{j\theta}$.

$$R = \frac{E_{TR}}{E_{CD}} = \frac{Q \sum_{q=0}^{Q-1} |A|^4}{(\sum_{q=0}^{Q-1} |A|^2)^2} = \frac{Q(QA^4)}{(QA^2)^2} = 1 \tag{5.23}$$

   This shows that the time-reversal gain over change detection is just unity. The performance of the time-reversal energy detector is exactly the same as the change detection based energy detector.

2. In the second case, the channel frequency response is assumed to follow a Gaussian distribution with variance $\sigma^2$. The expected value of even powers of the Gaussian random variable ($x$) is given by [98]

$$E[|x|^n] = 1 \cdot 3 \cdots (n-1)\sigma^n \tag{5.24}$$

The TR over CD energy gain of Equation 5.22 can also be written as

$$R = \frac{E_{TR}}{E_{CD}} = \frac{E[|H_t|^4]}{|E[|H_t|^2]|^2} \tag{5.25}$$

where

$$E[|H_t|^4] = E[|x|^4] = 3\sigma^4 \tag{5.26}$$

$$E[|H_t|^2] = E[|x|^2] = \sigma^2 \tag{5.27}$$

Therefore the TR-to-CD gain becomes

$$R = \frac{E_{TR}}{E_{CD}} = \frac{3\sigma^4}{\sigma^2\sigma^2} = 3 \quad (4.77dB) \tag{5.28}$$

Thus, using a single antenna, a time-reversal based system can provide a 4.77 dB gain over change detection. The actual performance of time-reversal gain depends on the field distribution in the medium.

We have studied the performance of time-reversal detection schemes using experimental data that were presented in Chapter 2. The test statistics can be described as follows

a) Change Detection:

In the presence of a target

$$Y_1(f) = H_t(f) + N_1(f) \tag{5.29}$$

In the absence of a target

$$Y_0(f) = N_1(f) \tag{5.30}$$

b) Time-reversal detection:

In the presence of a target

$$Z_1(f) = k(H_t(f) + N_1(f))^* H_t(f) + N_2(f) \tag{5.31}$$

In the absence of a target

$$Z_0(f) = N_2(f) \tag{5.32}$$

By using 15 dielectric rods as clutter and a copper pipe as the target (see Fig. 5.4), the performance of the time-reversal method is compared with change detection. Fig. 5.5 shows the power distributions of noise, time-reversal and change detection signals using an SNR of -7 dB and 0 dB. 201 frequency points have been used between 4 GHz and 6 GHz. In the experimental setup, there are 100 available single pair channels (10 by 10 antenna array). 20 of them have been used for averaging purposes which were selected randomly. As the plot suggests, when the SNR is low (-7 dB), the change detection and time-reversal power distributions approach to each other. This suggests that the time-reversal gain can be observed more clearly for low false alarm rates (FAR). By using 0 dB of SNR, the difference between time-reversal and change detection becomes more visible. Fig. 5.6 shows the mean power in noise, change detection and time-reversal signals using the set-up described in Fig. 5.4. As the plot clearly shows, as the SNR gets bigger, the difference between time-reversal and change detection becomes more visible. Fig. 5.7 shows the mean power of noise, change detection and time-reversal waveform using different numbers of scattering objects and a single object as a target. The results show that as the medium becomes more cluttered, the performance of time-reversal system gets better. The advantage of

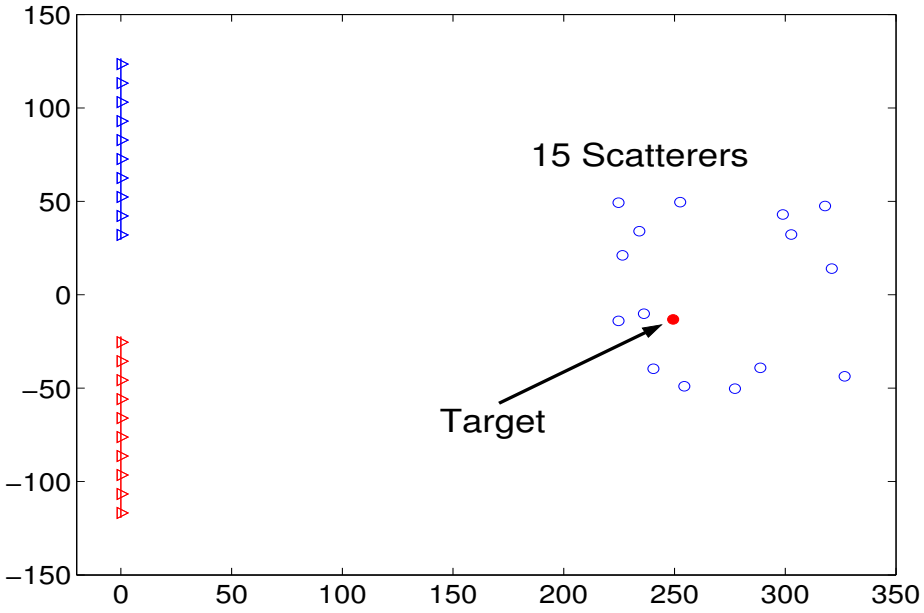


Figure 5.4: The experimental test setup. 15 scattering objects (dielectric rods) and a target (a copper pipe) are placed in the channel.

time-reversal based detection over change detection is more visible at higher SNR values. In the absence of any scattering objects in the medium, change detection and time-reversal power are supposed to be the same, but the target object has some slight frequency dependencies across the 2 GHz band which produce small dispersions in the time-domain. That is why the time-reversal power is slightly greater than that of change detection.

The time-reversal based detection suffers from back-propagated noise. At low SNRs, the performance of time-reversal based detection becomes close to change detection. The main reason for that is the back-propagation constant $k$ is matched to $H_t + N_1$ instead of $H_t$. When the noise becomes bigger than the signal, noise affects the back-propagation constant. If we can eliminate the back-propagated noise by averaging or if we multiple the back-propagated constant $k$ taking into account the signal component only, we can considerably improve the detection performance of a time-reversal system. Another way to eliminate noise is through filtering in the time-domain. If the approximate range of scattering and target environment is known, a filter can be designed to filter out the noise components outside the expected range. This can considerably reduce the noise power in

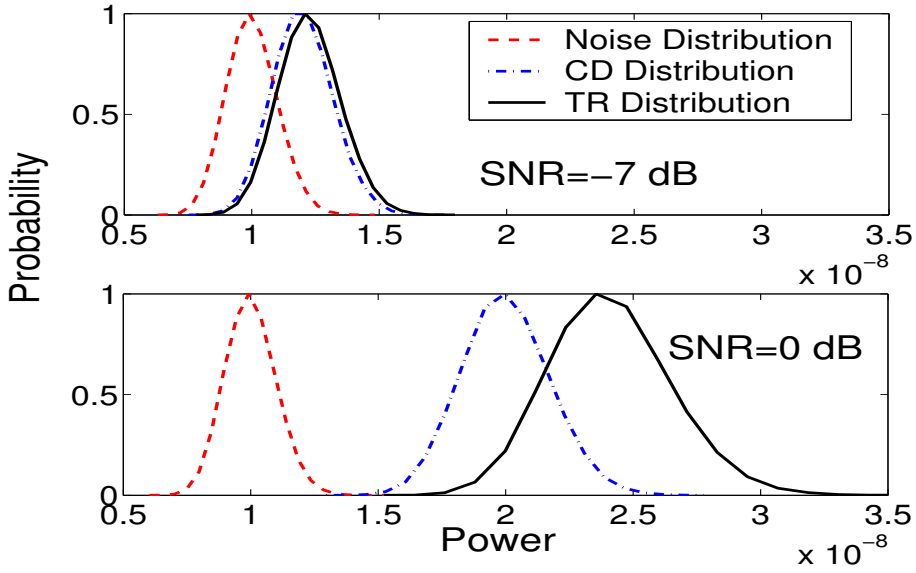


Figure 5.5: The normalized histogram of noise, change detection and time-reversal signal power with 0 dB and -7 dB SNRs.

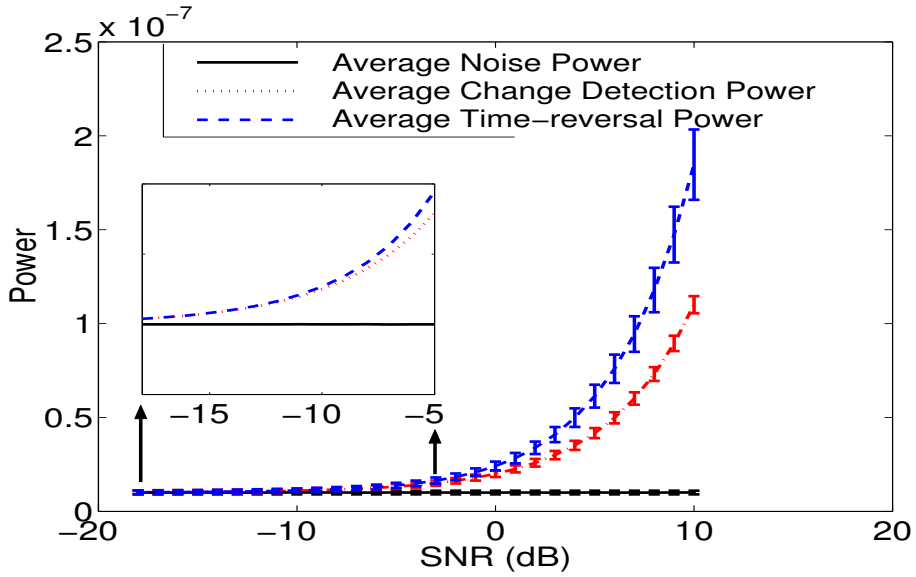


Figure 5.6: The mean value of noise, change detection and time-reversal signal power and their variation as a function of SNR.

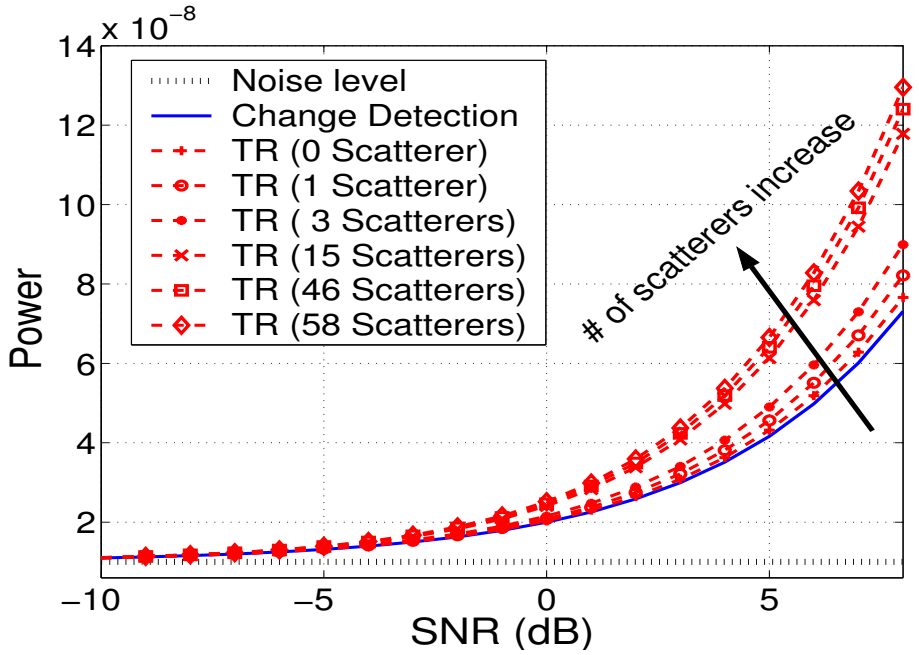


Figure 5.7: The mean value of noise, change detection and time-reversal signal powers using different numbers of scattering objects in the medium.

the time-reversal waveform. To explore this, we compared the performance of the energy detector in several cases where the only difference was due to the back-propagated noise. In the experiments, we have used different numbers of scattering objects to test the energy detector of time-reversal and change detection. In each case, the target was a 1.27 cm diameter copper pipe placed on the same location (as shown in Fig. 5.4). The scattering objects were 3.2 cm diameter solid dielectric rods. We have used 1,3,15,20, and 46 scattering objects at the points as indexed in Table 5.1. 201 frequency points have been used between 4-6 GHz. An SNR of -10 dB is used in all cases. Three cases were considered:

a) Noise present in the back-propagated waveform as given by Equation 5.31. The performance of the energy detector is shown in Fig. 5.8. The performance of time-reversal and change detection are very close to each other, time-reversal performing a little better.

b) A filter is designed in the time-domain to cancel the noise terms outside the expected duration of the scattering response. The time-domain pulse was between 0 and 100 ns. The minimum first arrival time is 15 ns, and we estimated that the significant echos in

Table 5.1: The positions of scattering objects on Fig. 2.23 and Fig. 2.24

| Number of Scatterers | The index of objects from Fig. 2.23 and Fig. 2.24 |
|---|---|
| 1 | 21 |
| 3 | 10,36,19 |
| 15 | 1,10,11,15,23:25,28,29,31,33,39,40,43,44 |
| 20 | 1,4,7,10,11,15,19,23:26,28,29,31,33,36,39,40,43,44 |
| 46 | 1:46 |

the medium are about 30 ns. So the filter passes everything between time intervals 15 ns and 45 ns and rejects outside this range. Since noise is randomly distributed across 100 ns time-duration but echos due to target are limited to a range of 30 ns between 15 ns and 45 ns, we have eliminated a big part of the noise from the time-reversal waveform. Fig. 5.9 shows the performance of the energy detector using the filter as described above. The filter clearly improved the detection performance of the time-reversal system compared to change detection.

c) The background noise is completely removed through averaging, or the back-propagation constant is matched only to the signal component (Fig. 5.10). The results show that as the number of scattering objects is increased, the performance of change detection stays the same, while time-reversal detection scheme gets better. In all three cases, time-reversal performs better than change detection, but the performance improves as the back-propagated noise is cancelled from the system. Another important point is that we have used 201 frequency points to implement the energy detector. This greatly removes the uncertainty in the noise, permitting detection using -10 dB of SNR. Designing the detector based on increasing numbers of frequency measurements lowers the SNR requirement. Each time the number of independent measurements is increased, the noise variation gets smaller. This is similar to doing averaging in the time-domain. The details of single antenna detection using various time-reversal algorithms and analytical expressions have been presented in [69].

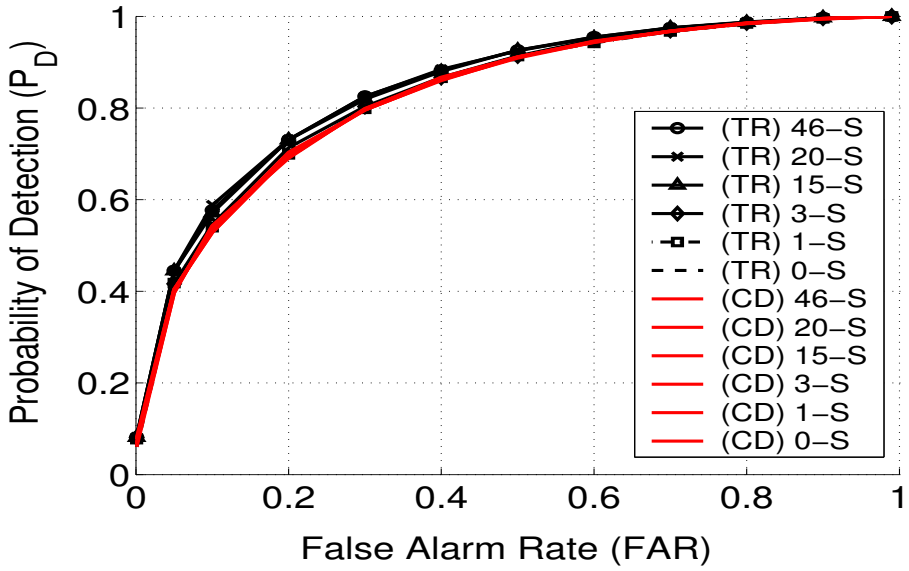


Figure 5.8: The performance of time-reversal based detection and change detection using different numbers of scattering objects in the medium.

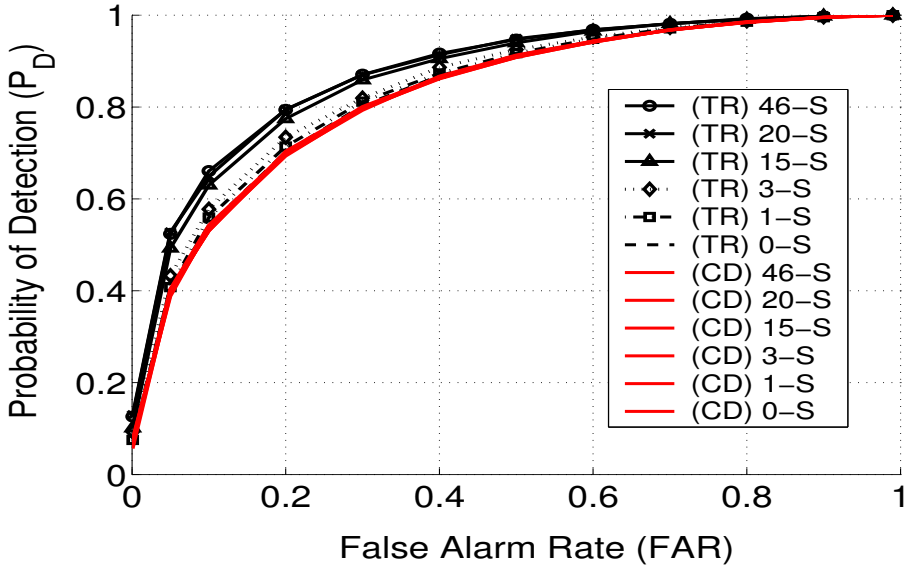


Figure 5.9: The performance of time-reversal based detection and change detection using different numbers of scattering objects in the medium. A filter is designed in the time-domain to remove the noise outside the expected duration of the scattering response, (15-45 ns).

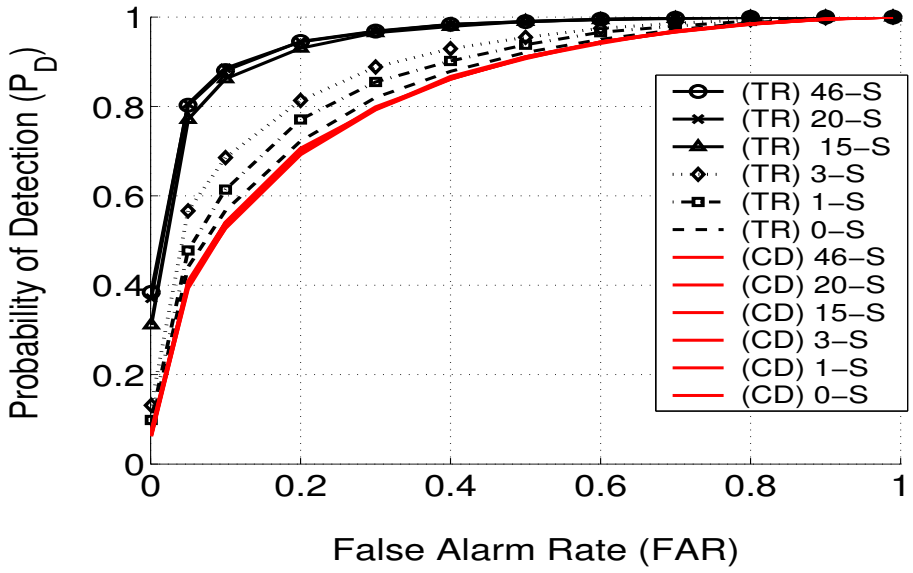


Figure 5.10: The performance of time-reversal based detection and change detection using different numbers of scattering objects in the medium. The back-propagated noise is ignored.

In the simplest case, where we have a wide-band power detector (like a diode detector), the total power in the passband is measured instead of individual frequencies. In the presence of a target in the medium, the total return power across the band is measured. In the absence of the target in the medium, the total noise power of the wide-band detector is measured, which increases in proportional to the total bandwidth. In this detection scheme, there is a single measurement, hence the noise is more random compared to the previous case. We have tested the performance of the single-carrier power detector in three scattering environments: no multipath, moderate multipath, and extreme multipath. In the first one, there is no scattering object in the medium. A copper pipe is the only target in front of the radar system (Fig. 5.11a). The second one has moderate multipath components in the presence of 58 dielectric rods as the scattering channel (Fig. 5.12a). The last one is the extreme multipath case, where we placed a 5 cm long metal stub target inside a duct cavity. The duct cavity produces extensive echos due to the target (Fig. 5.13a).

The detection performances of these three cases have been computed and compared with change detection results. There is no gain of time-reversal system over change de-

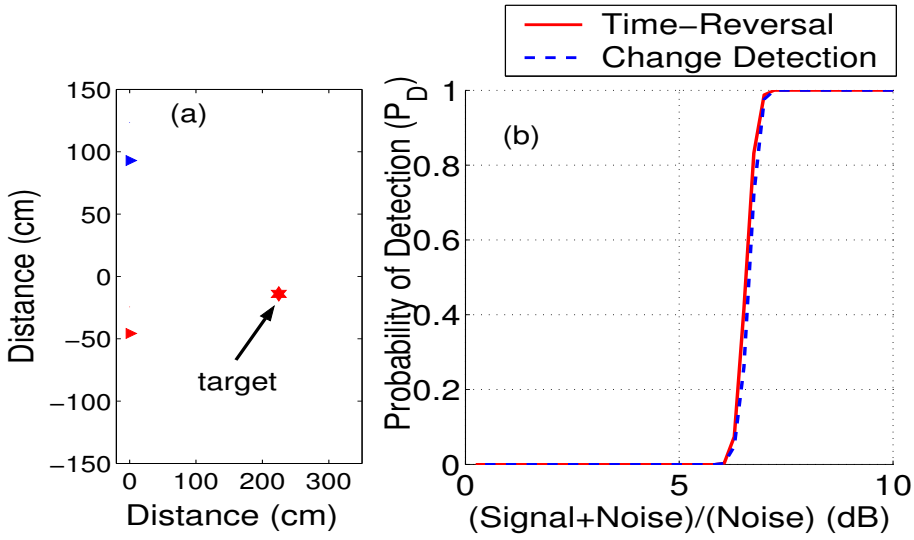


Figure 5.11: The performance of time-reversal based detection and change detection in the presence of single target in the medium. No scattering objects. False Alarm Rate is 1%.

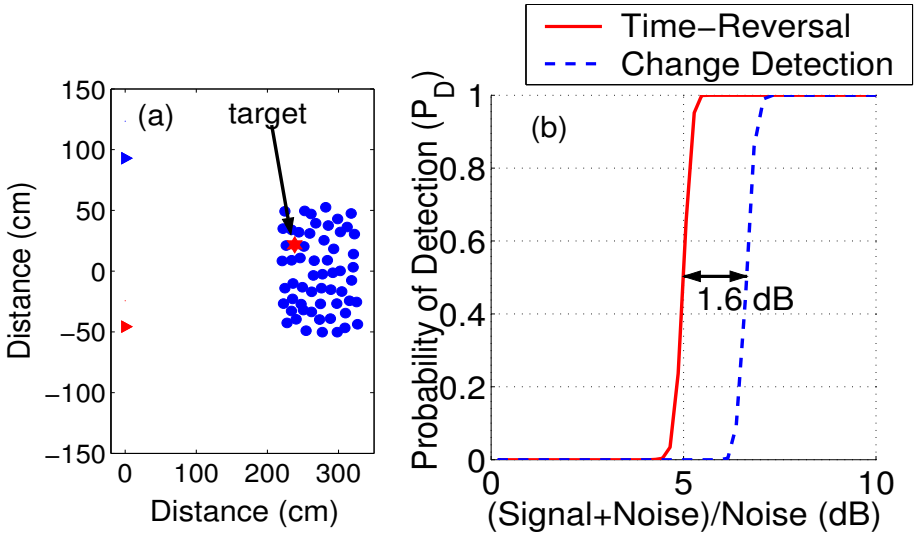


Figure 5.12: The performance of time-reversal based detection and change detection in the presence of 58 scattering objects in the medium. False Alarm Rate is 1%.

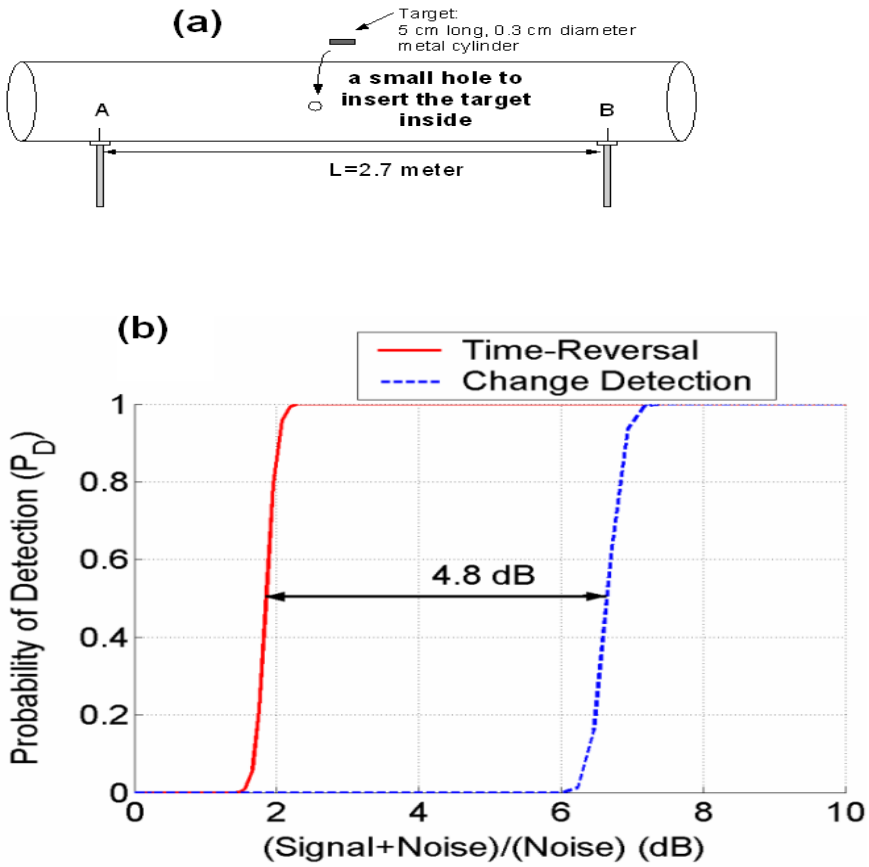


Figure 5.13: The performance of time-reversal based detection and change detection in a multipath rich duct channel. The target is a 5 cm long 0.3 cm diameter metal cylinder. False Alarm Rate is 1%.

tection in the first channel where there are no scattering objects in the medium. The time-reversal performance is exactly the same as that of change detection (Fig. 5.11b). Fig. 5.12b shows the performance of time-reversal detection to change detection in the moderate multipath channel. The SNR requirement of change detection stays the same, while time-reversal curve shifted to the left by 1.6 dB. Time-reversal thus provides a 1.6 dB improvement over change detection in this environment. In the extreme multipathing case, the time-reversal curve is shifted even further to the left (Fig. 5.13b). The resulting performance improvement is 4.8 dB over change detection.

### 5.2.3 Peak Detector

The detection scheme can also be designed in the time-domain as a peak detector. The time at which the waveform focuses is determined in advance. If the time-domain signal is sampled at the focusing time-instant, this can be compared with the noise to determine the presence or absence of a target. Similarly, the peak of the change detection scheme can be used to compare with the noise level to decide about whether a target exists in the medium. The time-domain change detection can be written as

$$y_{CD}(t) = h_t(t) + n(t) \tag{5.33}$$

The peak value is

$$y_{CD}(t)|_{peak} = max(|h_t(t) + n(t)|) \tag{5.34}$$

Similarly, the time-domain waveform of time-reversal signal is

$$z_{TR}(t) = k(h_t(T-t) + n(T-t)) * h_t(t) + n_2(t) \tag{5.35}$$

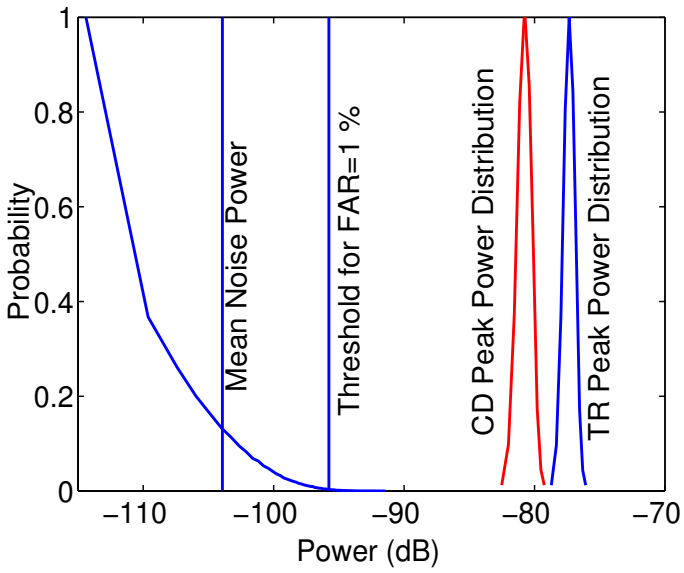


Figure 5.14: The distribution of noise, change detection peak and time-reversal peak power.

The peak of TR occurs at time $t = T$.

$$z_{TR}(t)|_{peak} = \int k(h_t(T-\tau)h_t(T-\tau) + n(T-\tau)h_t(T-\tau))d\tau + n_2(T) \tag{5.36}$$

The distribution of noise power, TR peak power and CD peak power is shown in Fig. 5.14. The threshold value is chosen for FAR of 1%. The performance of time-reversal and change detection peak detector is compared on Fig. 5.15. Using 46 dielectric rods in the medium, the time-reversal peak detectors provides a 4.7 dB improvement over change detection. The performance of time-reversal and change detection are very similar when there is only one scattering object in the medium. Compared to the energy detector results that were presented in the previous section, peak detector based time-reversal systems result in greater gain compared to change detection systems.

## 5.3 Multiple Antennas

The performance of time-reversal focusing can be improved using multiple antennas. By using multiple antennas, the focusing peak gets bigger compared to change detection and

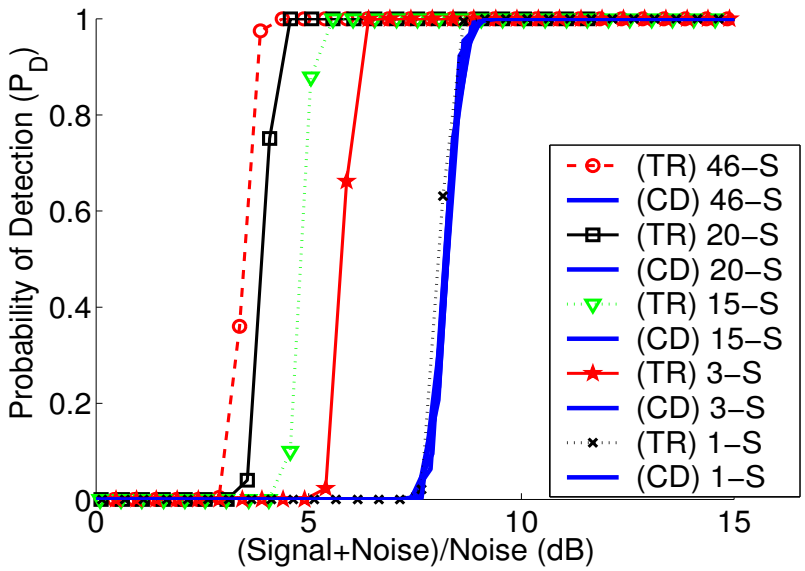


Figure 5.15: The probability of detection as a function of SNR for different numbers of scattering objects in the medium. False alarm rate is 1%.

the detection performance is improved. Fig. 5.16 shows the peak values of change detection and time-reversal using a single antenna and 10 antennas in an array. The results show that using 10 antennas, the TR-to-CD peak ratio is 8 in the case of just the target in the medium, and 20 when there are 46 additional scattering objects in the medium.

### 5.3.1 Time Reversal Adaptive Interference Canceller (TRAIC) for EM Wave Target Detection in Cluttered Environment

The TRAIC detection algorithm relies on the nulling of the medium. By using the time-reversal method with multiple antennas, we can minimize undesired echos due to scattering objects in the field. Co-phased pulses are first emitted from each one of the antennas in the transmit array. After scattering from the objects in the medium, the receive antennas capture the echo-signals. The received signals are time-reversed and sent back to the medium. They undergo similar reflections and coherently add up at the original source points. By inverting the polarity of alternating time-reversed signals before retransmission, we can null out the medium. That is, signals from even numbered antennas will add

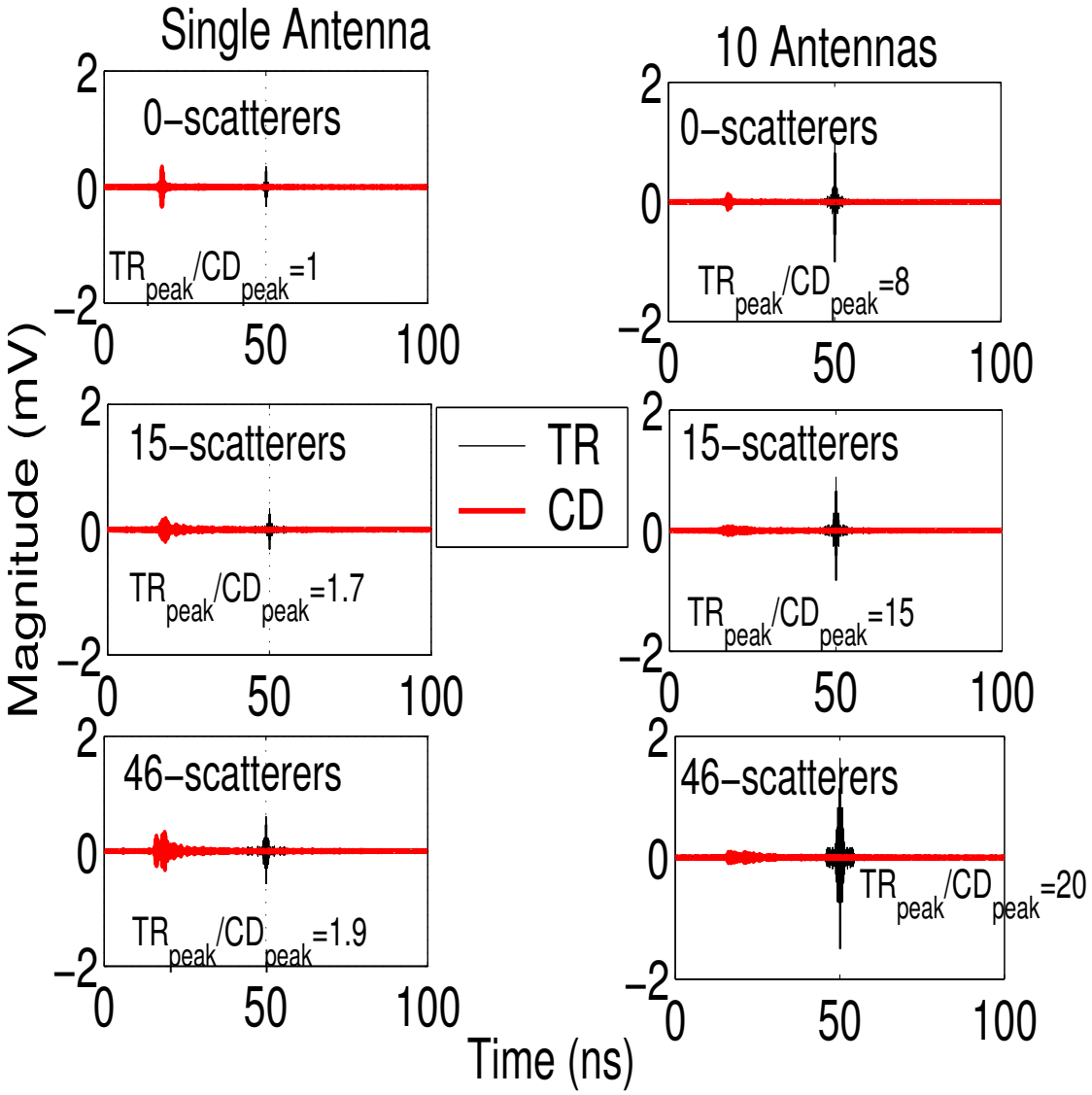


Figure 5.16: Multiple antennas improve the peaks of time-reversal waveforms compared to change detection waveforms.

coherently, signals from odd numbered antennas will add coherently but the combination of the odd and even signals will be 180 degrees out of phase, resulting in minimal signal strength at the original source points. Thus, the cluttered environment has been nulled. If any reflective object (target) appears in the field, the re-transmission of the modified time-reversal signal causes a reflection corresponding to the target. The experiments were conducted using 2 scattering objects and a target as shown in Fig. 5.17. In the set-up, we used 4 by 4 antenna arrays for the transmitter and receiver. In the TRAIC algorithm, there is a four-step process to decide whether there is a target in the field or not [65]. These steps along with the experimental considerations are explained below. Note that in this section, we have tested the performance of the TRAIC algorithm using the computational time-reversal method based on the measured forward channel response.

1. The first step is to record the channel Green's function through experimentation (Fig. 5.17). By putting all the scatterers in the field (without a target), we record the channel response. With the elements in the array fed with identical phase, a beacon signal is transmitted from each one of the transmit antennas simultaneously (A1 through A4). The amplitude and phase of the received signal at each array element on the receive side (B1 through B4) are recorded over the frequency range 4-6 GHz. This gives a frequency domain measurement of the Greens function of the channel to each array element.

2. The B-array antennas are then used to transmit the conjugate phase of the measured Greens function. On the receive side (A-array), the returned signals are recorded and summed. This process ensures that the signal is focused at the original source (Fig. 5.18). If we change the polarity of every other antenna on the B-array, and send the phase-changed time-reversed signals with B1(+), B2(-), B3(+), B4(-), then we will have a nulling effect instead of focusing. The time-reversed signals are sent to the field with different polarities from each one of the antennas. The electromagnetic fields try to avoid the scatterers and minimum energy reaches back to the receive

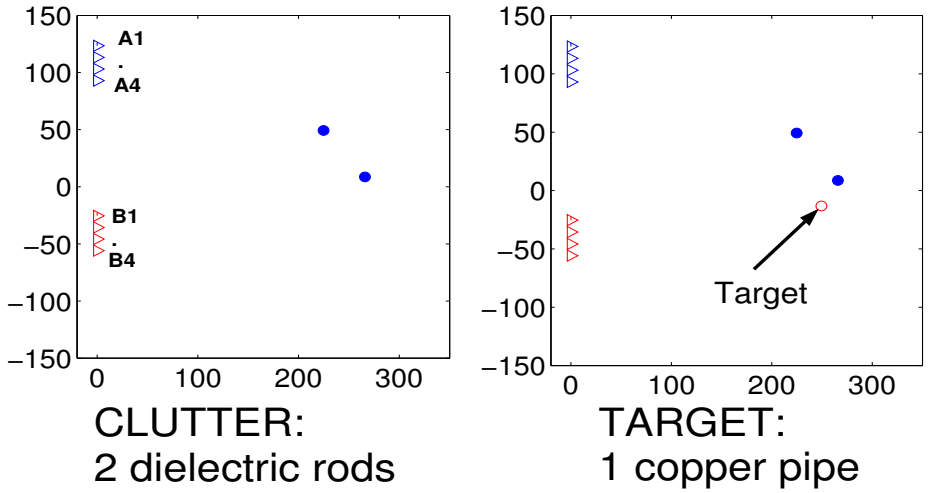


Figure 5.17: The experimental setup of clutter and target's position among the clutter.

antennas (A-array) (Fig. 5.18).

3. We repeat the previous step with the target in the field. The time-reversed signals avoid the scatterers and concentrate around the target, causing a stronger echo to appear at the receive antennas.

4. Next, we subtract the nulling signal obtained with target and without target, and take the time-reverse of the difference and send this signal from the transmitters (B-array). The time-reversed difference signal will avoid all scatterers and focus just around the target and result in a stronger echo on the A-array after summed through all 4 antennas (Fig. 5.19).

Fig. 5.19a is the impulse response and Fig. 5.19b is the frequency response waveforms of TRAIC and change detection. The TRAIC power across the 2 GHz band is 11 dB bigger than change detection power. The performance of TRAIC has been tested in a rich scattering channel where there were 46 dielectric rods and a copper pipe as the target. The experimental setup is shown in Fig. 5.20. Fig. 5.21 shows the focusing and nulling of clutter using all 4 antennas ($2^{nd}$ step in TRAIC algorithm), Fig. 5.22 is the final TRAIC waveform as compared to change detection. The TRAIC resulted in 8.5 dB improvement

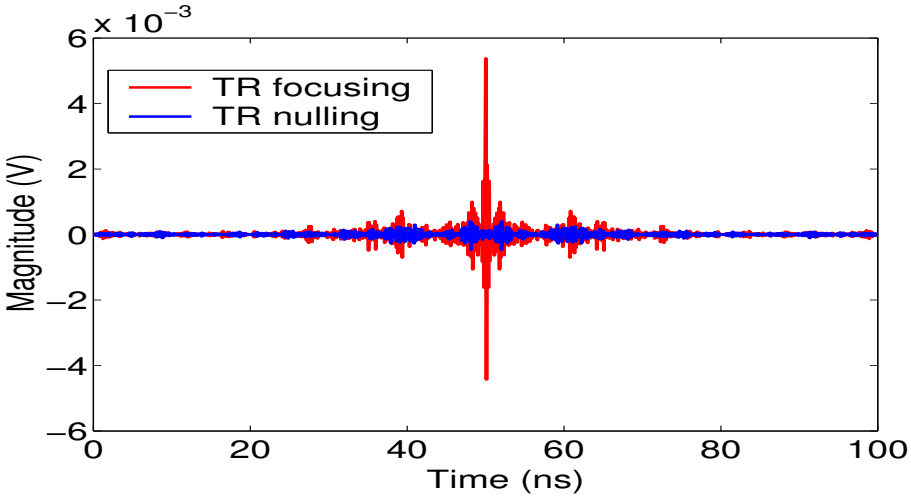


Figure 5.18: The focusing and nulling in the clutter channel.

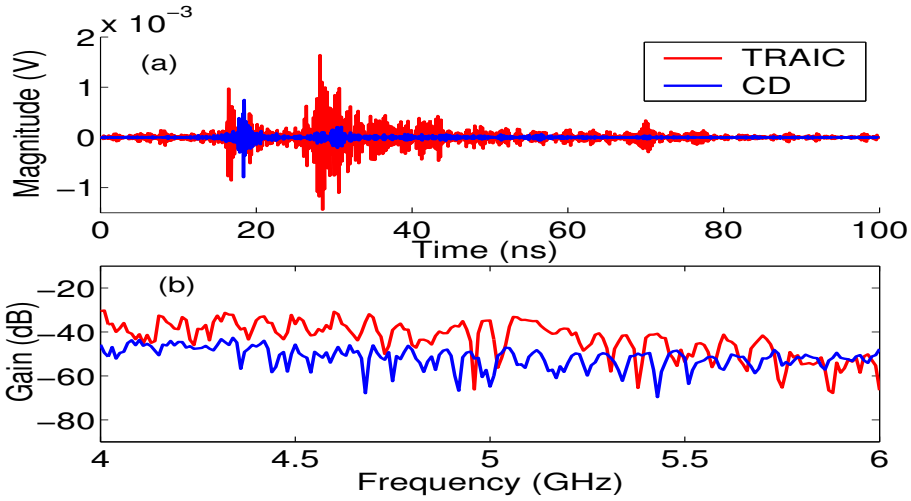


Figure 5.19: The final TRAIC and Change Detection waveforms obtained in (a) time-domain (b) frequency domain.

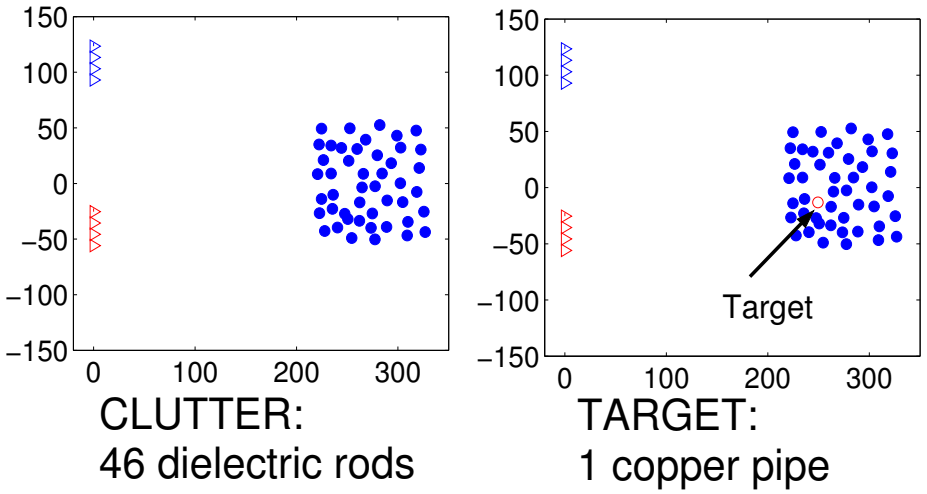


Figure 5.20: The experimental setup of clutter and target's position among the clutter.

in radar return power from target compared to change detection scheme. The performance of the TRAIC algorithm has also been tested in a channel where the target is hiding behind a metal duct (Fig. 5.23). There are dielectric rods, and copper pipes in addition to the 15.3 cm diameter duct in the channel. The target is a 1.27 cm diameter copper pipe that is placed just behind the duct. There is no line of sight from the antenna array to the target. In the absence of the target, the focusing and nulling waveforms are shown in Fig. 5.24. The return signal due to TRAIC is shown in Fig. 5.25 along with change detection return. It is clear from the time-domain and frequency domain waveforms that TRAIC results in a stronger return compared to change detection. The power gain of TRAIC over change detection is about 6 dB.

## 5.4 Conclusion

We have shown that time-reversal methods can be used to design detection schemes that can work better in a cluttered medium. Single antenna time-reversal experiments have shown that the gain of the time-reversal based detection scheme is related to channel clutter. The more scattering the channel provides the better is the time-reversal gain. The matched filter performance deteriorates as the medium becomes more cluttered, while

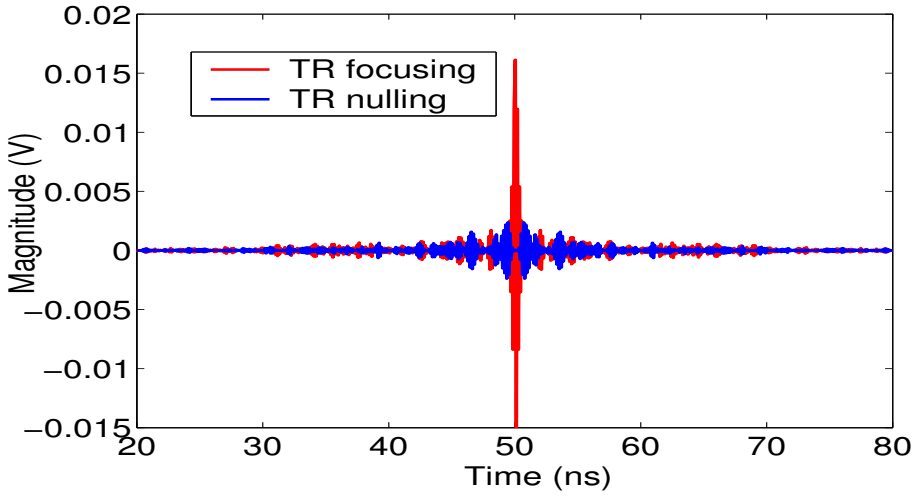


Figure 5.21: The focusing and nulling in the clutter channel.

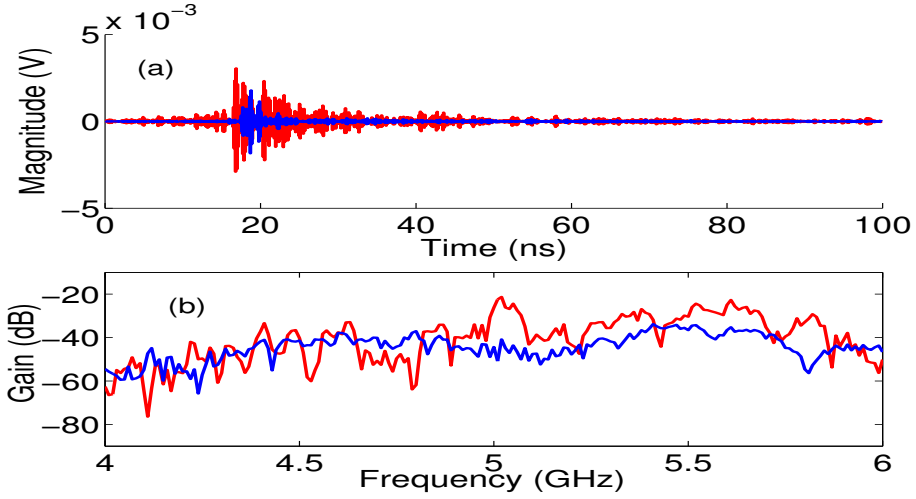


Figure 5.22: The final TRAIC and Change Detection waveforms obtained in (a) time-domain (b) frequency domain.

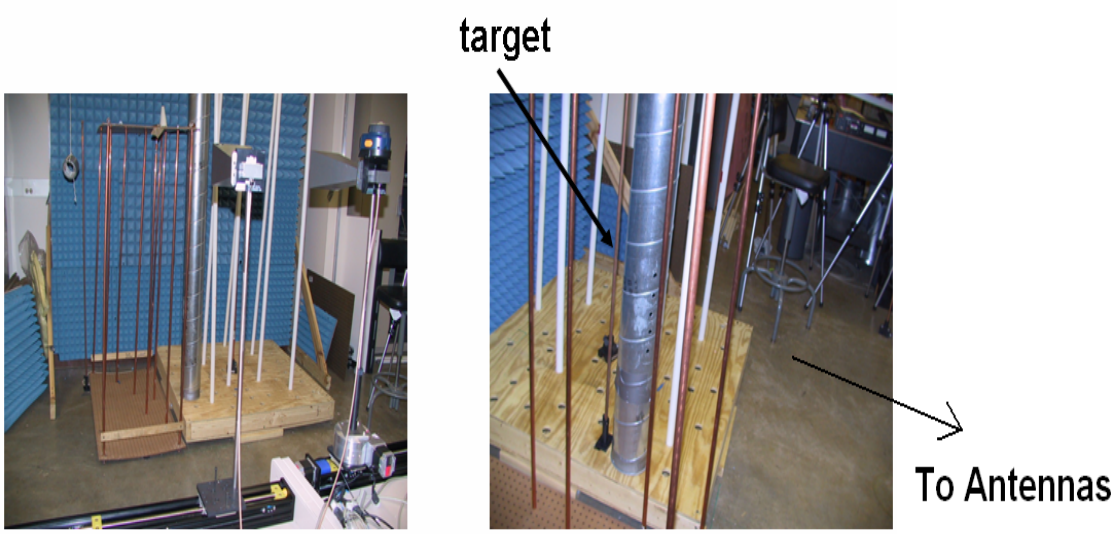


Figure 5.23: 15.3 cm diameter duct is placed in the range of the antennas and a 1.27 cm copper pipe is placed just behind the duct. There is no line of sight from the any elements of 4 by 4 antenna array.

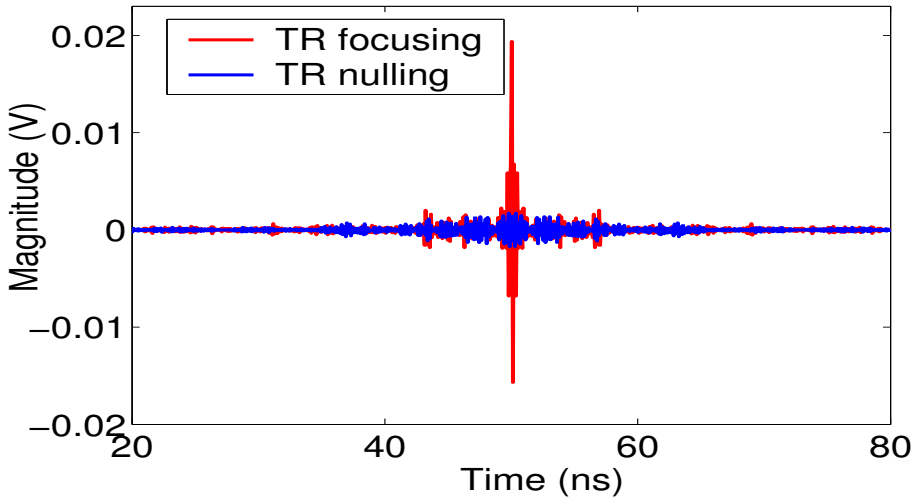


Figure 5.24: The focusing and nulling in the clutter channel where target is hiding behind the duct.

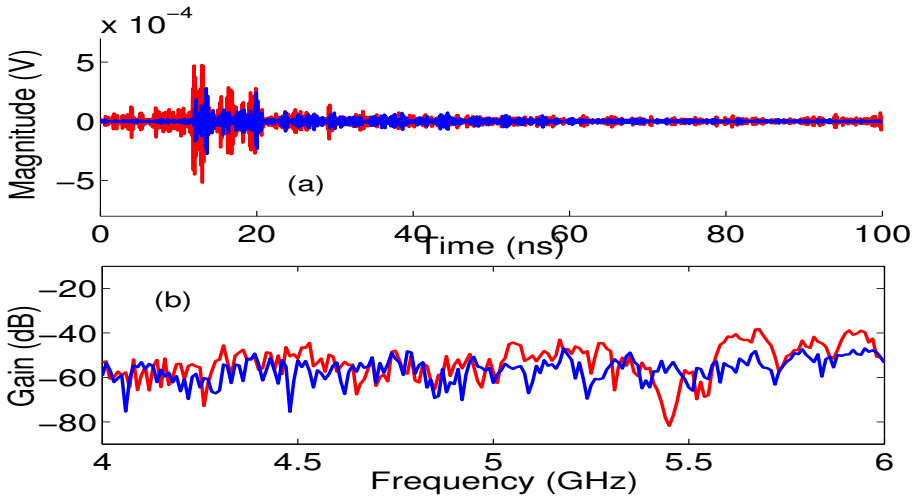


Figure 5.25: The final TRAIC and Change Detection waveforms obtained in (a) time-domain (b) frequency domain.

time-reversal works better as the channel becomes more cluttered. The detection scheme can be designed in the frequency domain as well as in the time-domain. The number of frequency measurements determines the minimum SNR requirement. As the number of samples increases, the required SNR becomes lower. So there is a trade-off between the complexity of the radar and the SNR required. The experimental results have shown that as the scattering environment gets more random, time-reversal detection gain improves compared to conventional change detection. We have observed a 1.6 dB improvement in SNR in a laboratory environment where we have used 58 dielectric rods as scatterers and a copper pipe as the target. In a multipath rich duct channel, the time-reversal based detection scheme resulted in 4.8 dB improvement over change detection. The time-domain peak detector along with the time-reversal method provided a greater gain compared to the time-reversal based energy detector. Using multiple antennas along with time-reversal methods results in a significant additional gain of time-reversal over conventional change detection. The peak of the time-reversal waveform improves as the number of antennas is increased. Experimental verification of a multiple antenna detection algorithm has been explained that uses time-reversal nulling methods. The clutter channel is first nulled and the RF energy is re-directed towards the target that enters into the medium. TRAIC algo-

rithm resulted in a significant improvement of SNR of the echo due to the target compared to conventional change detection schemes.

# Chapter 6

# Conclusions and Future Work

Time-reversal techniques show significant promise for improving the detection performance of a radar system. Time-reversal methods utilize the multipath components in the medium and focus electromagnetic waves within a region on the order of a wavelength in extent. Time-reversal system performance depends on three main parameters. These are multipath components in the medium, the bandwidth of the waveform and the number of antennas in the time-reversal array. As any one of them gets bigger, time-reversal produces a sharper focusing signal both in time and in space. In this thesis, we have experimentally demonstrated different aspects of time-reversal techniques using electromagnetic waves. As stated earlier, the main goal was to be able to use electromagnetic time-reversal methods for detection of targets in highly cluttered channels. We have demonstrated by experiments the gains achieved by electromagnetic time-reversal techniques over conventional radar methods to focus radar beams, to null the clutter environment and finally to detect targets in highly scattering environments. In this thesis, the main principles of time-reversal systems have been studied and the clutter channel has been analyzed to assess the feasibility of time-reversal methods in a laboratory environment.

## 6.1 Summary of Contributions

1. **Experimental characterization of a controlled scattering environment and extraction of the main parameters for a time-reversal system**

   **The 50% correlation bandwidth of the 1.44 $m^2$ scattering channel saturates around 140 MHz at 5 GHz.** The multipath components in the medium are characterized by coherence bandwidth. **Multiple experimental setups were prepared for measuring the scattered fields of a target/scatterers layout for subsequent post-processing to do target detection or imaging.** In the case of a single object in the channel, the coherence bandwidth started with an average value of 850 MHz and as the number of scattering objects was increased, the correlation bandwidth became smaller. In the presence of 20 scattering rods in the medium, the correlation bandwidth reached the minimum average value 120 MHz, and saturated around 140 MHz with additional scattering rods.

   We observed that **the correlation bandwidth of the "clutter+target" channel is very similar to that of the "target only" channel after clutter subtraction.** Consequently, once we characterize the clutter medium we can predict the correlation bandwidth of the target-only response. Since the correlation bandwidth directly affects the time-reversal focusing quality, we conclude that if we analyze only the clutter channel, we can estimate the performance of a time-reversal system. We also observed a relationship between the inter-scatterer spacing and the time-reversal gain over change detection. **When the inter-scatterer spacing becomes 4 wavelengths or less in our experiments, time-reversal system performance is observed to saturate.**

   **Time-reversal focusing saturates based on bandwidth to correlation bandwidth ratio. The number of frequency samples needed can be estimated by using the correlation bandwidth. In the presence of 30 scattering objects in the medium, 14 samples is enough in the 4-6 GHz frequency range to get the maximum time-**

**reversal gain.**

**We have developed a Green's function based propagation software to analyze wave propagation in complex media.** The software assumes point targets and includes first and secondary reflections from the objects in the channel. Higher order reflections are ignored. The advantage of this software tool is that the simulation time is independent of area of the scattering objects. The simulation time is dependent only on the number of scattering objects in the medium. Time-reversal focusing and the correlation bandwidth of various scattering environments have been studied using this software. We have concluded that **correlation bandwidth depends on the area over which the scattering objects are distributed. The larger the area, the lower the correlation bandwidth.**

**The correlation distance is about 10 cm at 5 GHz if there are more than 6 scattering objects in the 1.2 m x 1.2 m area.** Correlation distance determines the minimum spacing of antennas in a time-reversal array. In the case of a single object in the medium, the correlation distance was 35 cm and as the medium gets cluttered, the value dropped to 10 cm, approximately 2 wavelengths.

2. **Wide-band physical time-reversal experiment**

We have constructed a wideband physical time-reversal system using the phase-conjugation approach in the frequency domain. The system used a 4 by 4 antenna array. The experiments were conducted using 1.5 GHz bandwidth between 4 and 5.5 GHz. **We have demonstrated physical wideband time-reversal focusing and nulling in a laboratory environment.**

3. **Wide-band computational time-reversal experiment**

By using omni-directional antennas and a 2-D grid, we have studied wide-

band time-reversal focusing and nulling performance in a complex laboratory environment. **The effects of bandwidth and number of antennas** on temporal and spatial focusing have been researched through experimental measurements. **The impact of noise** has also been studied, showing that focusing can be achieved with SNR values as low as -4 dB.

4. **Focusing on 7 spots using 6 antennas and 2 GHz bandwidth**

   We have demonstrated focusing at 7 spots on the 2-D grid using 6 antennas and 2 GHz bandwidth.

5. **Time-reversal nulling using zero-forcing approach**

   Using experimental data, we have shown a zero-forcing time-reversal system, where we obtained a very deep nulling spot on the 2-D grid.

6. **Single antenna time-reversal nulling in a cavity environment**

   We have developed a novel algorithm that can be used to achieve nulling using a single antenna. The nulling algorithm utilizes the multipath components in the medium to cancel the signal at the source point.

7. **Electromagnetic time-reversal focusing and nulling simulations in a waveguide channel**

   We used a waveguide channel simulator and studied super-resolution focusing and nulling performance of time-reversal methods in a waveguide environment. The temporal and spatial focusing and nulling have been explored. The effects of bandwidth and the reflectivity of the end-caps have been analyzed.

8. **Demonstration of single antenna time-reversal focusing and nulling in longitudinal and circumferential directions in a cylindrical duct**

   Using a single antenna, the focusing and nulling waveforms were obtained in the longitudinal and circumferential directions in a circular waveguide.

9. **Detection performance of an experimental time-reversal radar system**

   We have analyzed the time-reversal and change detection performance at various $SNR's$. Using a wideband energy detector, the time-reversal system performance is the same as change detection in the absence of clutter. As the multipaths increase in the environment, time-reversal performance improves compared to change detection. The difference between time-reversal and change detection became more apparent for higher SNR values. **The time-reversal energy gain has been derived for two extreme channels that have (a) flat frequency response and (b) completely random frequency response. The gain in the former case was unity while in the latter case 4.77 dB.** We have also **developed a detection scheme based on time-domain peaks**. The time-reversal peak time is known in advance through system design. The waveform is sampled just at that focusing instant and compared with the change detection peak.

10. **Experimental verification of TRAIC algorithm**

    Measurements with different numbers of scatterers have been post-processed using the Time Reversal Adaptive Interference Cancellation method (TRAIC). The results show that the TRAIC algorithm also improves performance over change detection in a cluttered medium.

## 6.2 Future Work

There are many important topics that need to be explored regarding the target detection problem using electromagnetic time-reversal methods. Some of these topics are summarized below.

1. **Extend the experiments to outdoor environment**

   The experiments can be extended to outdoor channels where there are trees and other scattering objects with irregular shapes. Targets can be hidden under trees, or buried as in the case of mines. The detection performance of time-reversal schemes should be analyzed in those realistic channels.

2. **Determination of target location, imaging, and identification**

   Another important topic that we did not explore is target location using time-reversal methods. This can be through imaging of the complete medium, or imaging of the medium after clutter is subtracted. Another way that may potentially give the location of the target is to analyze time-reversal waveforms from multiple antennas. Can time-reversal techniques improve the ability to identify a target as well as detect it?

3. **Simultaneous focusing and nulling using time-reversal methods**

   In this thesis, we have shown that we can focus RF energy simultaneously at 7 spots using just 6 antennas. Can we focus RF energy at some spots and simultaneously null other spots using the time-reversal techniques?

4. **Target detection using time-reversal nulling in a cavity environment**

We experimentally demonstrated time-reversal focusing and nulling in a cavity channel. Signal nulling can be used to facilitate detection of the presence of any object that is brought into the cavity. Consequently, any slight change in the medium indicates the presence of the target. Zero-forcing time-reversal is particularly effective at generating deep nulls. Can time-reversal nulling improve target localization as well as detection in a cavity?

5. **Improved Nulling Schemes**

Do other nulling schemes exist that yield deeper nulls and/or increase the time-span of the null?

6. **The performance of time-reversal based radar systems when a large target is embedded among small scatterers**

So far we have studied the time-reversal performance using objects that have relatively similar radar cross sections. In contrast, consider a large tank surrounded by trees, leaves etc., so that there is a big difference between the radar cross section of the target and clutter objects. How will time-reversal methods perform in this case? The weak scattering between a large target and the clutter can possibly be emphasized using some type of custom filter.

7. **The imaging of extended targets**

Can time-reversal methods enable imaging the back side of a target embedded in clutter?

8. **Polarization effects in the E-M experiments**

The polarization of antennas can be used to improve the multipath components of an antenna system and may positively affect time-reversal system performance.

9. **The impact of coupling between antennas in an antenna array**

The time-reversal methods work better if the antenna elements are omnidirectional so that the waves arrive to the source antenna from all directions producing super-resolution. However, with omnidirectional elements, mutual coupling between the elements can be significant. Just as with conventional phased array antennas, this mutual coupling must be taken into account when determining the required element excitations.

# Appendix A

# Experimental Setup

The frequency domain experiments have been conducted using an Agilent E8358A Vector Network Analyzer. A vector network analyzer (VNA) is an instrument which measures the complex transmission and reflection characteristics of two-port devices in the frequency domain. It does this by sampling the incident signal, separating the transmitted and reflected waves, and then performing ratios that are directly related to the reflection and transmission coefficients of the two-port. Frequency is swept to rapidly obtain amplitude and phase information over a band of frequencies of interest. The s-parameter representation is the most common format used to represent VNA measurements. The s-parameters S11 and S21 can be interpreted as the input reflection coefficient and forward transfer coefficient (gain or loss) under the conditions that the source and load impedances represent perfect Zo (e.g. 50 Ohm) matches. Likewise S22 and S12 can be interpreted as the output reflection coefficient and reverse transfer coefficient (gain or loss) under the conditions that the source and load impedances represent perfect (e.g. 50 Ohm) matches. User calibration is necessary to correct for cable losses, to correct for non-matched conditions, and to establish phase reference planes. In our experiments, we have recorded S21 transmission coefficients across 4 GHz to 6 GHz using 201 frequency points. The phase reference planes were at the antenna terminals. At each frequency, 0 dBm of power was transmitted from the source and the signal power and phase were recorded at the other

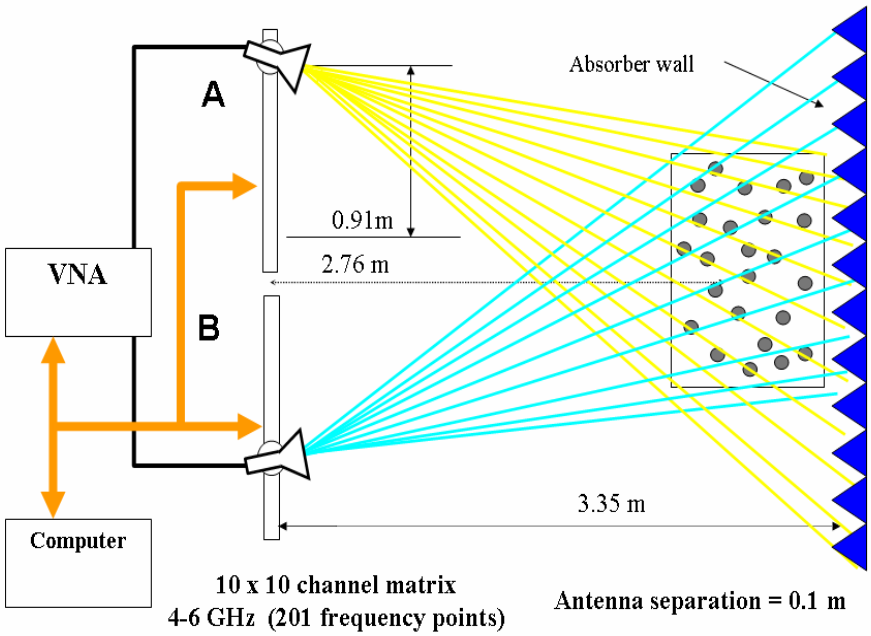


Figure A.1: The schematics of multistatic radar experimental setup.

terminal. The IF bandwidth was 5 kHz. The lower the IF bandwidth, the lower is the noise floor. The sweeping time was 42 msec.

The experimental setup is shown in Fig. A.1. The height of the scattering rods were 2.4 m. We have used 2 pairs of linear stages (Velmex MB25 Unislide) and rotary stages (Velmex B5990TS). We used horn antennas on the rotary stages that are rotated towards the scattering objects. Antennas were moved by 10.16 cm between measurements. We marked 10 points on rail A and 10 points on rail B. The first point is when both antennas are on the upper side of the rails (Fig. A.1). The antenna on rail A stays on the same point while the antenna on rail B moves all 10 points marked on rail B and after that returns back to the starting point and antenna on rail A moves by 10.16 cm to the next point. At the end, we have 100 channel measurements of the scattering objects in the medium. Each channel measurement has 201 frequency points. So for each set of experiment, we recorded a 100 x 201 complex channel matrix for post-processing.

# Bibliography


[1] J.D. Parsons, *"The Mobile Radio Propagation Channel,"* Second Edition, John Wiley & sons, 1992.

[2] G. J. Foschini and M. J. Gans, *"On limits of wireless communication in a fading environment when using multiple antennas,"* Wireless Personal Commun., vol. 6, no. 3, pp. 311-335, Mar. 1998.

[3] D.S. Shiu, G. J. Foschini and M. J. Gans, and J.M. Kahn, *"Fading correlation and its effect on the capacity of multielement antenna systems,"* IEEE Trans. Com., vol. 48, pp.502-512, March 2000.

[4] A.J. Paulraj, D.A. Gore, R.U. Nabar, H. Bolcskei, *"An overview of MIMO communications - a key to gigabit wireless,"* Proceedings of the IEEE, Volume 92, Issue 2, pp. 198-218, Feb 2004.

[5] A.J. Paulraj, C.N. Boon, *"Space-time modems for wireless personal communications,"* Personal Communications, IEEE, Volume 5, Issue 1, pp. 36-48, Feb. 1998.

[6] A.S.Y. Poon, R.W. Brodersen, D.N.C Tse, *"Degrees of freedom in multiple-antenna channels: a signal space approach,"* Information Theory, IEEE Transactions on Volume 51, Issue 2, pp. 523-536, Feb. 2005.

[7] J.W. Wallace, M.A. Jensen, A.L. Swindlehurst, B.D. Jeffs, *"Experimental characterization of the MIMO wireless channel: data acquisition and analysis,"* Wireless Communications, IEEE Transactions on Volume 2, Issue 2, pp. 335-343, March 2003.

[8] M. Skolnik, *"Introduction to Radar Systems,"* McGraw-Hill Book Company, 1980.

[9] Mathias Fink, *"Time-Reversed Acoustics,"* Scientific American, pp. 91-97, November 1999.

[10] M. Born, and E. Wolf, *"Principles of Optics,"* Academic Press, New York, 1970.

[11] M. Fink, *"Time-reversal of ultrasonic fields - Part I: Basic Principles,"* IEEE Trans. Ultrasonics, Ferroelectrics, and Frequency control, vol.39, no. 5, pp. 555-566, 1992.

[12] F. Wu, J. L. Thomas, and M. Fink, *"Time-reversal of ultrasonic fields - Part II: Experimental results,"* IEEE Trans. Ultrasonics, Ferroelectrics, and Frequency control, vol.39, no. 5, pp. 567-578, 1992.

[13] A. Ishimaru, *"Wave propagation and scattering in random media,"* New York, Academic Press, 1978.

[14] P. Sheng, *"Scattering and localization of classical waves in random media,"* Singapore, World Scientific Publishing Co., 1990.

[15] D. M. Pepper, *"Nonlinear Optical Phase Conjugation,"* Optical Engineering, vol. 21, no. 2, p. 156, Mar/Apr. 1982.

[16] M. Fink, C. Prada, F. Wu, and D. Cassereau, *"Self focusing in inhomogeneous media with time reversal acoustic mirrors,"* in IEEE Ultrasonics Symposium, Montreal, Canada, vol. 1, pp. 681Ű686, 1989.

[17] C. Prada, F. Wu, and M. Fink, *"The iterative time reversal mirror: A solution to self- focusing in the pulse echo mode,"* J. Acoust. Soc. Am., pp. 1119-1129, 1991.

[18] M. Fink, *"Time reversal mirrors,"* J. Phys. D, pp. 1330-1350, 1993.

[19] C. Prada, J.L. Thomas, and M. Fink, *"The iterative time reversal process: Analysis of the convergence,"* J. Acoust. Soc. Am., Vol. 97, pp. 62-71, 1995.

[20] A. Derode, P. Roux, M. Fink, *"Robust acoustic time-reversal with higher order multiple scattering,"* Phys. Rev. Letter, 75, pp. 4209-9, 1995.

[21] C. Prada, S. Manneville, D. Spolianski, and M. Fink, *"Decomposition of the time reversal operator: Detection and selective focusing on two scatterers,"* J. Acoust. Soc. Am., pp. 2067-2076, 1996.

[22] E. Kerbrat, C. Prada and D. Cassereau, *"Ultrasonic nondestructive testing of scattering media using the decomposition of the time-reversal operator,"* IEEE Trans. Ultrasonics, Ferroelectrics, and Frequency control, vol.49, no. 8, pp. 1103-1112, 2002.

[23] W.A. Kuperman and J.F. Lynch, *"Shallow-Water Acoustics,"* Physics Today, October 2004.

[24] S. Kim, W.A. Kuperman, W.S. Hodgkiss, H.C. Song, G. Edelmann, and T. Akal, *"Robust time reversal focusing in the ocean,"* J. Acoust. Soc. Am. 114, pp. 145-157, 2003.

[25] G. Edelmann, T. Akal, W.S. Hodgkiss, S. Kim, W.A. Kuperman, H.C. Song, *"An initial demonstration underwater acoustic communication using time reversal,"* IEEE J. of Oceanic Eng. 27, pp. 602-609, 2002.

[26] W.A. Kuperman, W.S. Hodgkiss, H.C. Song, T. Akal, C. Ferla, and D.R. Jackson, *"Phase conjugation in the ocean: Experimental demonstration of a time reversal mirror,"* J. Acoust. Soc. Am. 103, pp. 25-40, 1998.

[27] W. S. Hodgkiss, H. C. Song, W. A. Kuperman, T. Akal, C. Ferla, and D. R. Jackson. *"A Long-Range and Variable Focus Phase-Conjugation Experiment in Shallow Water,"* Journal of the Acoustical Society of America, 105(3), pp.1597-1604, March 1999.

[28] David R. Dowling and Darrell R. Jackson, *"Phase Conjugation in Underwater Acoustics,"* Journal of the Acoustical Society of America, 89, pp.171-181, January 1990.

[29] G. F. Edelmann, T. Akal, and W.S. Hodgkiss, S. Kim, W.A. Kuperman, and H.C. Song, *"An initial demonstration of underwater acoustic communication using time reversal,"* IEEE J. Oceanic Engineering, 27, pp. 602-609, 2002.

[30] M. Fink, D. Cassereau, A. Derode, C. Prada, P. Roux, and M. Tanter, *"Time reversed acoustics,"* Rep. Prog. Phys., pp. 1933-1994, 2000.

[31] P. Blomgren, G. Papanicolaou, H. Zhao, *"Super-resolution in time-reversal acoustics,"* J. Acoust. Soc. Am., 111, pp. 238-248, 2002.

[32] C.Tsogka and G. Papanicolaou, *"Time reversal through a solid-liquid interface and super- resolution,"* Inverse Problems 18, pp. 1639-1657, 2002.

[33] G. Papanicolaou, L. Ryzhik and K. Solna, *"Statistical stability in time reversal,"* SIAM J. on Appl. Math., 64, pp. 1133-1155, 2004.

[34] P. Blomgren, G. Papanicolaou and H. Zhao, *"Super-Resolution in Time-Reversal Acoustics,"* Journal of the Acoustical Society of America, Vol 111, pp. 230-248, 2002.

[35] L. Borcea, C. Tsogka, G. Papanicolaou and J. Berryman, *"Imaging and time reversal in random media,"* Inverse Problems, 18, pp. 1247-1279, 2002.

[36] J. F. Clouet, J.P. Fouque, *"A time reversal method for an acoustical pulse propagating in randomly layered media,"* Wave Motion, 25, pp. 361-368, 1997.

[37] D.R. Dowling, D.R. Jackson, *"Narrow band performance of phase conjugate arrays in dynamic random media,"* J. Acoust. Soc. Am., 91, pp. 3257-3277, 1992.

[38] M. Asch, W. Kohler, G. Papanicolaou M. Postel and B. White, *"Frequency content of randomly scattered signals,"* Siam Review, 33, pp. 519-62, 1991.

[39] W. Kohler, G. Papanicolaou and B. White, *"Localization and Mode Conversion for Elastic Waves in Randomly Layered Media,"* Wave Motion, 23, pp.1-22 and 181-201, 1996.

[40] C. Prada, J.L. Thomas and M. Fink, *"The iterative time reversal process: Analysis of the convergence,"* Journal of the Acoustical Society of America, 97, pp. 62-71, 1995.

[41] C. Prada, S. Manneville, D. Spoliansky and M. Fink, *"Decomposition of the time reversal operator: Detection and selective focusing on two scatterers,"* Journal of the Acoustical Society of America, 99, pp. 2067-2076, 1996.

[42] R.K. Snieder and J.A.Scales, *"Time-reversed imgaing as a diagnostic of wave and particle chaos,"* Physical Review E, 58, pp. 5668-5675, 1998.

[43] N. Mordant,C. Prada, and M. Fink, *"Highly resolved detection and selective focusing in a waveguide,"* Journal of the Acoustical Society of America, 105, pp. 2634-2642, 1999.

[44] H. Lev-Ari and A.J. Devaney, *"The time-reversal technique re-interpreted: subspacebased signal processing for multi-static target location,"* IEEE Sensor Array and Multichannel Signal Processing Workshop, pp. 509-513, Cambridge, MA, 2000.

[45] S. K. Lehman and A. J. Devaney, *"Transmission mode time-reversal super-resolution imaging,"* J. Acoust. Soc. Am. 113, pp. 2742-2753, 2003.

[46] S. Hou, K. Solna, H. Zhao, *"Imaging of Location and Geometry for Extended Targets Using the Response Matrix,"* J. Comp. Phys. Vol. 199(1), pp. 317-338, 2004.

[47] P. Blomgren, G. Papanicolaou, H. Zhao, *"Super-resolution in time-reversal acoustics,"* J. Acoust. Soc. Am., 111, pp. 238-248, 2002.

[48] C. Prada and J.L. Thomas, *"Experimental subwavelength localization of scatterers by decomposition of the time reversal operator interpreted as a covariance matrix,"* J. Acoust. Soc. Am. 114, pp. 235-243, 2003.

[49] E. Kerbrat, C. Prada, D. Cassereau, and M. Fink, *"Ultrasonic nondestructive testing of scattering media using the decomposition of the time reversal operator,"* IEEE Trans. Ultrason., Ferroelec., Freq. Contr., 49(8), 2002.

[50] J.G. Minonzio, C. Prada, D. Chambers, D. Clorennec, and M. Fink, *"Characterization of sub-wavelength elastic cylinders with the decomposition of the time-reversal operator: Theory and experiment,"* J. Acoust. Soc. Am., 117, pp. 789-798, 2005.

[51] G. Montaldo, M. Tanter, and M. Fink, *"Real time inverse filter focusing by iterative time reversal,"* J. Acoust. Soc. Am., 115, pp. 768-775, 2004.

[52] G. Montaldo, M. Tanter, and M. Fink, *"Revisiting iterative time reversal processing: Application to detection of multiple targets,"* J. Acoust. Soc. Am., 115, pp. 776-784, 2004.

[53] Claire Prada, Sebastian Manneville, Dimitri Spoliansky, and Mathias Fink, *"Decomposition of the time reversal operator: Detection and selective focusing on two scatterers,"* Journal of the Acoustical Society of America, 99, pp. 2067-2076, 1996.

[54] C. Prada and M. Fink, *"Eigenmodes of the time-reversal operator: A solution to selective focusing in multiple target media,"* Wave Motion 20, pp. 151-163, 1994.

[55] C. Prada, S. Manneville, D. Spoliansky and M. Fink, *"Decomposition of the time-reversal operator: Application to detection and selective focusing on two scatterers,"* J. Acoust. Soc. Am. 99, pp. 2067-2076, 1996.

[56] M. Mordant, C. Prada and M. Fink, *"Highly resolved detection and selective focusing in a waveguide using the D.O.R.T. method,"* J. Acoust. Soc. Am. 105, pp. 2634-2642, 1999.

[57] H. Lev-Ari and A.J. Devaney, *"The time-reversal technique re-interpreted: Subspace-based signal processing for multi-static target location,"* IEEE Sensor Array and Multichannel Signal Processing Workshop, Cambridge, MA, pp. 509-513, 2000.

[58] S. Lehman and A.J. Devaney, *"Transmission mode time-reversal super-resolution imaging,"* J. Acoust. Soc. Am. 113, pp. 2742-2753, 2003.

[59] M. Dennison and A. J. Devaney, *"Inverse scattering in inhomogeneous background media Part II: Multiple frequency case and SVD analysis,"* Inverse Problems, vol. 20, pp. 1307-1324, 2004.

[60] A.J. Devaney, E. A. Marengo and F. K. Gruber *"Time-reversal-based imaging and inverse scattering of multiply scattering point targets,"* J. Acoust. Soc. Am., 2005.

[61] B. Henty, D. Stancil, *"Bandwidth limitations of phase-conjugate arrays used for multipath focusing,"* Antennas and Propagation Society Symposium, IEEE, vol.3, pp. 2792-2795, 2004.

[62] B. Henty, D. Stancil, *"Multipath enabled super-resolution for rf and microwave communication using phase conjugate arrays,"* Phys. Rev. Letts. 93, 243904, 2004.

[63] G. Lerosey, J. de Rosny, A. Tourin, A. Derode, G. Montaldo, and M. Fink, *"Time Reversal of Electromagnetic Waves,"* Physical Review Letters, vol. 92, pp. 194301, 2004.

[64] A.G. Cepni, D.D. Stancil, *"Single Antenna Microwave Nulling using Time-Reversal Techniques,"* Microwave Symposium Digest, IEEE MTT-S International, pp. 1723-1726, June 2005.

[65] J.Zhu, Y. Jiang, D.D. Stancil, and J. Moura, *"A Novel Time Reversal Method for Target Detection in Cluttered Media,"* in the proceedings of Antennas and Propagation (APS-05) conference, Washington DC, July 2005.

[66] J. Moura, Y.W. Jin, D. Stancil, J.G. Zhu, A.G.Cepni, Y. Jiang, B. Henty, *"Single Antenna Time Reversal Adaptive Interference Cancellation,"* IEEE International Conference on Acoustics, Speech, and Signal Processing, (ICASSP), Volume 4, pp. 1121-1124, March 2005.

[67] J. M. F. Moura, Y. Jin, D. Stancil, J. G. Zhu, A. Cepni, Y. Jiang, and B. Henty, *"Time reversal adaptive interference cancellation and detection,"* in the proceedings of the 13th Annual Workshop on Adaptive Sensor Array Processing, Lexington, MA, June 2005.

[68] A.G. Cepni, D.D. Stancil, J.Zhu, Y. Jiang, *"Experimental Results on Target Detection in Cluttered Medium using Electromagnetic Time-Reversal Techniques,"* in the proceedings of Antennas and Propagation (APS-05) conference, Washington DC, July 2005.

[69] J. Moura, Y.W. Jin, *"Detection by Time Reversal: Single Antenna,"* submitted to Journal of Acoustics, 2005.

[70] A.G. Cepni, D.D. Stancil, J. Zhu, Y. Jiang, *"Microwave Signal Nulling using Multiple Antennas and Time-Reversal Method,"* in the Proceedings of Vehicular Technology Conference (VTC Fall05), Dallas, TX, Sep. 2005.

[71] D.F. Gingras, P.Gerstoft and N.L. Gerr, *"Electromagnetic matched field processing for source localization,"* IEEE Int. Conf. Acoustics, Speech, and Signal Processing, 1997.

[72] M.E. Yavuz, F.L. Teixeira, *"A numerical study of time-reversed UWB electromagnetic waves in continuous random media,"* Antennas and Wireless Propagation Letters, Volume 4, pp. 43-46, 2005.

[73] L. Dehong, K. Gang, L. Ling, C. Ye, S. Vasudevan, W. Joines, L.H. Qing, J. Krolik, L. Carin, *"Electromagnetic time-reversal imaging of a target in a cluttered environment,"* IEEE Transactions on Antennas and Propagation, Volume 53, Issue 9, pp. 3058-3066, Sept. 2005.

[74] K. Sarabandi, I. Koh, and M. D. Casciato, *"Demonstration of time reversal methods in a multipath enviroment,"* Antennas and Propagation Society International Symposium, IEEE Volume 4, pp.4436-4439, June 2004.

[75] M. Emami, J. Hansen, A. Kim, A. J. Paulraj, G. Papanicolaou, D. Cheung, and C. Prettie, *"Predicted Time Reversal Performance in Wireless Communications Using Channel Measurements,"* Communications Letters, 2004.

[76] C.Oestges, J. Hansen, M. Emami, A. J. Paulraj, and G. Papanicolaou, *"Time Reversal Techniques for Broadband Wireless Communications,"* Proceedings of the European Microwave Week, Amsterdam, Oct. 2004.

[77] P. Kyritsi, G. Papanicolaou, P. Eggers and A. Opera, *"MISO time reversal and delay spread compression for FWA channels at 5GHz,"* Antennas and Wireless Propagation Letters, 3, pp.96-99, 2004.

[78] S. Guoqing, K.J. Ranson, *"A three-dimensional radar backscatter model of forest canopies,"* IEEE Transactions on Geoscience and Remote Sensing, Volume 33, Issue 2, pp. 372-382, Mar 1995.

[79] J.M. Bourgeois, G.S. Smith, *"A fully three-dimensional simulation of a ground-penetrating radar: FDTD theory compared with experiment,"*, IEEE Transactions on Geoscience and Remote Sensing, Volume 34, Issue 1, pp. 36-44, Jan 1996.

[80] J.B. Billingsley, A. Farina, F. Gini, M.V. Greco, L. Verrazzani, *"Statistical analyses of measured radar ground clutter data,"* IEEE Transactions on Aerospace and Electronic Systems, Volume 35, Issue 2, pp. 579-593, 1999.

[81] T. S. Rappaport, *"Wireless Communications: Principles and Practice,"* Prentice Hall, 1996.

[82] K.F. Riley, M.P. Hobson, S.J. Bence, *"Mathematical methods for physics and engineering: A comprehensive guide,"* Cambridge University Press, 1998.

[83] A.J. Devaney, *"Time reversal imaging of obscured targets from multistatic data,"* Antennas and Propagation, IEEE Transactions on Volume 53, Issue 5, pp. 1600-1610, May 2005.

[84] A.Derode, A.Tourin, J.de Rosny, M.Tanter, S.Yon, M.Fink, *"Taking advantage of multiple scattering to communicate with time-reversal antennas,"* Physical Review Letters, vol. 90, Issue 1, 2003.

[85] http://www.atmmicrowave.com/wave-horn.html

[86] M. Fink, C. Prada, *"Acoustic time-reversal mirrors,"* Inverse Problems, vol. 17(1), pp. R1 - R38, Feb. 2001.

[87] G.T. Ruck, D.E. Barrick, W.D. Stuart, and K.C. Krichbaum, *"Radar Cross Section Handbook,"* 2 volumes, Plenum Press, New York, 1970.

[88] J.W. Crispin, K.M. Siegel, *"Methods of Radar Cross Section Analysis,"* Academic Press, New York, 1968.

[89] P. Blacksmith, R.E. Hiatt, and R.B. Mack, *"Introduction to Radar Cross Section Measurements,"* Proc. IEEE, vol.53, pp. 901-920, 1965.

[90] M.R. Andrews, P.P. Mitra, R. Decarvalho, *"Tripling the capacity Of wireless communications using electromagnetic polarization,"* Nature, 409, pp. 316-318, January 2001.

[91] J.P. Van't Hof and D.D. Stancil, *"Ultra-wideband high data rate short range wireless links,"* Proceedings of the 55th Vehicular Technologies Conference 2002, Vol. 1, pp. 85-89, May 2002.

[92] M. Fink, *"Time-reversed acoustics,"* Physics Today, vol. 50, no. 3, pp. 34-40, 1997.

[93] P. V. Nikitin, D. D. Stancil, A. G. Cepni, O. K. Tonguz, A. E. Xhafa, and D. Brodtkorb, *"Propagation model for the HVAC duct as a communication channel,"* IEEE Transactions on Antennas and Propagation, vol. 51, no 5, pp. 945-951, May 2003.

[94] A.G. Cepni, D.D. Stancil, and D. Brodtkorb, *"Experimental mode content analysis technique for complex overmoded waveguide systems,"* IEEE Antennas and Propagation Society Symposium (APS-04), vol. 3, pp. 2991-2994, California, 2004.

[95] P. V. Nikitin, D. D. Stancil, O. K. Tonguz, A. E. Xhafa, A. G. Cepni, and D. Brodtkorb, *"RF propagation in an HVAC duct system: impulse response characteristics of the channel,"* IEEE Antennas and Propagation Symposium (APS-02), vol. 2, pp. 726-729, 2002.

[96] A.G. Cepni, D.D. Stancil, A.E. Xhafa, B. Henty, P.V. Nikitin, O.K. Tonguz, and D. Brodtkorb, *"Capacity of multi-antenna array systems for HVAC ducts,"* IEEE International Conference on Communications (ICC-04), vol. 5, pp. 2934-2938, Paris, 2004.

[97] Simon Haykin, *"Communication Systems,"* 4th Edition, John Wiley Sons, Inc.

[98] A. Papoulis, *"Probability, Random variables and Stochastic processes,"* McGraw-Hill Companies.